AD NUMBER

AD804590

LIMITATION CHANGES

TO:

Approved for public release; distribution is unlimited.

FROM:

**Distribution authorized to U.S. Gov't. agencies and their contractors;
Administrative/Operational Use; NOV 1966. Other requests shall be referred to Rome Air Development Center, Griffiss AFB, NY.**

AUTHORITY

RADC ltr 17 Sep 1971

RADC-TR-66-663
Final Report

SURFACE WAVE BEHAVIOR IN PHASED ARRAYS

Dr. L.W. Lechtreck
Sylvania Electronic Systems-East
A Division of Sylvania Electric Products Inc.
100 First Avenue, Waltham, Mass. 02154

TECHNICAL REPORT NO. RADC-TR-66-663
November 1966

Rome Air Development Center
Research and Technology Division
Air Force Systems Command
Griffiss Air Force Base, New York

SURFACE WAVE BEHAVIOR IN PHASED ARRAYS

Dr. L. W. Lechtreck
Sylvania Electronic Systems-East
A Division of Sylvania Electric Products Inc.
100 First Avenue, Waltham, Mass. 02154

ABSTRACT

Mutual coupling in a phased array can cause its radiation performance to vary with electrical phasing used to steer the array. Large performance degradations can accrue when many coupling contributions add in-phase. This happens when the steering phase advance equals the mutual coupling phase delay between consecutive elements. For these critical scan directions reflections can be very large, and the antenna array will transmit or receive very little power, as evidence by deep holes in the element radiation pattern.

A large, flat, uniformly spaced array of identical antenna elements is analyzed. A relationship is found between critical scan angle and mutual coupling coefficients. Element radiation pattern, active array mismatch, and radiation efficiency are shown to be equivalent representations of phased array scan performance.

Extensive radiation pattern and mutual coupling measurements were made in a planar, equi-angular array of coaxial horn antennas. These measured mutual coupling coefficients were summed over columns of the test array. The phases of these column sums were found to vary linearly with distance. At the critical scan angle, all columns on one side of the array couple in-phase and re-radiate destructively, causing deep holes in array coverage and in element radiation pattern. Empirical coupling velocities were less than the free space velocity of light. Radiation holes appeared at scan angles which were smaller than those for which the grating lobe maximum enters real space.

Many physical perturbations of the array geometry were investigated experimentally to determine their influence on array scan performance. Several diverse array types are reported to have radiation minima attributable to in-phase coupling accumulation.

TABLE OF CONTENTS

TABLE OF CONTENTS (Continued)

LIST OF ILLUSTRATIONS

LIST OF ILLUSTRATIONS (Continued)

INTRODUCTION

A phased array consists of an assembly of fixed antenna elements, coherently excited through a beam forming and steering network. The phased array is steered by controlling the phase (or time) delays connected to each antenna element.

Mutual coupling between antenna elements can cause large variations in array performance as a function of scan angle. Coupling contributions accumulate in-phase with maximum effect on performance in those critical scan directions for which the consecutive steering phase advances match the mutual coupling phase delays. This report describes the nature of this coupling accumulation and its effect on array scan performance.

The analysis is general, not unique, to any particular antenna type. The array is assumed to be large and planar with identical antenna elements at uniform spacing. Each antenna element is excited with the same intensity and with a uniform progressive phase delay which matches the radiation retardation of each element in the desired direction of scan.

Phased arrays are used in many different electronic systems. A specific application of this study is in large, multifunction, phased array radar.

SECTION I

THEORY OF COUPLING ACCUMULATION

Mutual coupling in phased arrays causes the antenna active impedance to vary with beam scan angle. The impedance variation and consequent radiation pattern degradations can be computed from the array mutual coupling coefficients and antenna drives. Both are knowable. The transmission line voltages driving the antennas are determined by the array illumination taper and radar scan direction. The mutual coupling coefficients are knowable either from measurement or analysis. From this knowledge, one can construct the active impedance, scanning reflection, element power pattern, and target illumination intensity vs. scan angle. The analysis here will be general, not unique to any particular antenna type. We will assume that the array is large, flat, and has uniform interelement spacing.

Figure 1-1 shows a uniformly spaced, planar phased array and its coordinates. The array face is in the XY plane. The Z axis is the array normal and the pole of a spherical coordinate system. θ is the polar angle measured from the outward array normal; ϕ is the longitude about this normal. The small circles in Figure 1-1 represent potential antennas. In a uniform rectangular array, identical antenna elements occupy every circle; separations d_x and d_y are independent design constants. In an equiangular hexagonal array identical antennas occupy alternate circles (in checkerboard fashion) with $d_x = \sqrt{3}\, d_y$. Any plane containing the hexagonal array normal and passing through any one of the 6 closest elements is called a cardinal plan (e.g. $\phi = 90°$). The bisecting planes are called intercardinal planes (e.g. $\phi = 0°$).

1.1 ACTIVE REFLECTION COEFFICIENT

An array of M × N antenna elements constitutes an MN port network, which usually is reciprocal, lossy (radiating), and obeys linear superposition. The active mismatch of the central (0, 0) antenna element (with all neighbors suitably excited) is given by the following exact relation:

$$\Gamma = \sum_m \sum_n S_{mn} \left(\frac{V_{mn}}{V_{oo}}\right) \qquad (1\text{-}1)$$

where

S_{mn} = mutual coupling coefficient between the central (0, 0) antenna and the (m, n^{th}) antenna

V_{mn} = drive applied to the (m, n^{th}) antenna

V_{oo} = drive applied to the $(0, 0^{th})$ antenna element.

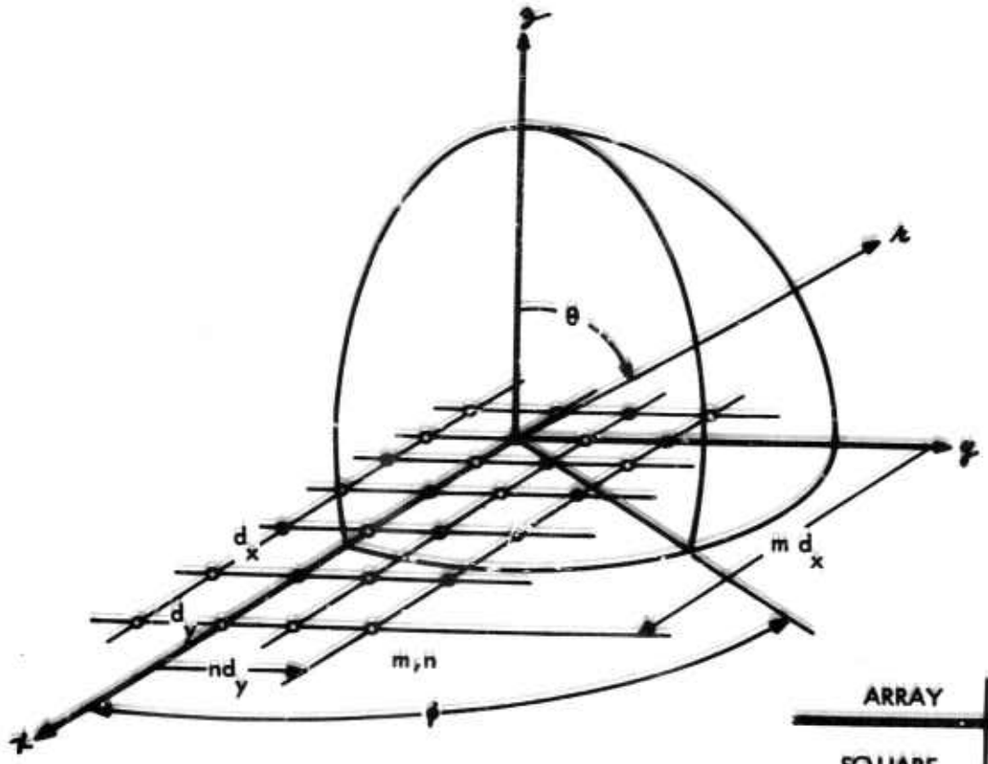

2456-66W

ARRAY	SPACING	ANTENNA LOCATIONS
SQUARE	$\frac{d_x}{d_y} = 1$	ALL "m" ALL "n" (BLACK DOTS & OPEN CIRCLES)
HEXAGONAL	$\frac{d_x}{d_y} = \sqrt{3}$	m + n EVEN (BLACK DOTS OR OPEN CIRCLES)

Figure 1-1. Spherical Coordinates

Each antenna drive V_{mn} is characterized by an amplitude and a phase angle. The amplitude is determined by the chosen array illumination (assumed uniform in the neighborhood of the reference element 0, 0). The phase is determined by the beam pointing direction and controlled by the array steering network. The steering phase advance is assumed to be the exact complement of the radiation retardation in the selected direction of the array scan. Thus all array radiation contributions add in phase when the far field observer at r, θ, ϕ is at a maximum of the steered beam $\theta = \theta_s$, $\phi = \phi_s$. The drive applied to the $(m, n)^{th}$ antenna is

$$\frac{V_{mn}}{V_{oo}} = e^{-jK_o[md_x \sin\theta_s \cos\phi_s + nd_y \sin\theta_s \sin\phi_s]} \tag{1-2}$$

Subscripts "s" refer to the array steering commands. The phase increments between consecutive columns and rows are respectively

$$\Psi_x = K_o d_x \sin\theta_s \cos\phi_s = 2\pi\left(\frac{d_x}{\lambda_o}\right)\cos(x, r)$$

$$\Psi_y = K_o d_y \sin\theta_s \sin\phi_s = 2\pi\left(\frac{d_y}{\lambda_o}\right)\cos(y, r) \tag{1-3}$$

where cos(x, r) and cos(y, r) are direction cosines between the scan beam and the X or Y axis respectively. Inserting equations (1-2) and (1-3) into (1-1) yields the array active reflection coefficient $\Gamma(\Psi_x, \Psi_y)$ and its Fourier complement S_{mn}.

$$\Gamma(\Psi_x, \Psi_y) = \sum_m \sum_n S_{mn} e^{-j(m\Psi_x + n\Psi_y)} \tag{1-4}$$

$$S_{mn} = \left(\frac{1}{2\pi}\right)^2 \int_{\Psi_x=-\pi}^{\pi} \int_{\Psi_y=-\pi}^{\pi} \Gamma(\Psi_x, \Psi_y) e^{j(m\Psi_x + n\Psi_y)} d\Psi_x d\Psi_y \tag{1-5}$$

1.2 PERIODICITY AND SYMMETRY OF SCAN MISMATCH

Equation (1-4) shows that the active reflection coefficient is a periodic function of Ψ_x and Ψ_y.

In a rectangular array, the period is

1. $\Delta\Psi_x = 2\pi m''$ or $\Delta\cos(x, r) = \left(\frac{\lambda_o}{d_x}\right) m''$ and

2. $\Delta\Psi_y = 2\pi n''$ or $\Delta\cos(y, r) = \left(\frac{\lambda_o}{d_y}\right) n''$

m'' and n'' are arbitrary independent integers, generating the familar grating lobe series. At each grating lobe the steering command Ψ_x and Ψ_y repeats, consequently, the active reflection is also repetitive.

A hexagonal array can be regarded as the sum of two interlaced rectangular arrays. Its active reflection coefficient has a period

1. $\Delta\Psi_x = \pi m''$ or $\Delta\cos(x, r) = \left(\frac{\lambda_o}{2d_x}\right) m''$ and

2. $\Delta\Psi_y = \pi n''$ or $\Delta\cos(y, r) = \left(\frac{\lambda_o}{2d_y}\right) n''$.

Here m'' and n'' are arbitrary integers having an even sum. They form the grating lobe series for the hexagonal array.

If the coupling coefficients are symmetric, $S_{m,n} = S_{-m,-n}$, then the reflection coefficient is also symmetric, $\Gamma(\Psi_x, \Psi_y) = \Gamma(-\Psi_x, \Psi_y)$. These symmetry conditions are usually met in rectangular and hexagonal arrays of linearly or circularly polarized antenna elements.

1.3 IN-PHASE COUPLING ACCUMULATION

Equation (1-4) shows that the active reflection coefficient $\Gamma(\Psi_x, \Psi_y)$ is a summation of complex coupled contributions from neighboring antennas. Each contribution is generally very small but many coupling contributions can add in-phase to produce a large mismatch resulting in minimal radiation in certain critical scan directions. These critical scan angles will now be evaluated in terms of the array mutual coupling coefficients.

Consider array steering in the principal plane ($\phi_s = 0$) containing rows of a rectangular array, or in the intercardinal plane of a hexagonal array. All antenna elements in any column are driven in the same phase (see Figure 1-2). The steering phase increments (equation (1-3)) become

$$\Psi_x = \frac{2\pi d_x}{\lambda_o} \sin\theta_s \quad \text{and} \quad \Psi_y = 0. \tag{1-6}$$

The array scan mismatch (equation (1-4)) becomes

$$\Gamma(\Psi_x) = \sum_m \left(\sum_n S_{mn}\right) e^{-jm\Psi_x}. \tag{1-7}$$

The inner summation is over all the elements in any one column "m"; the outer summation is over columns of the array. The net coupling contribution from any one column[1] can be written in terms of its amplitude and phase

$$\sum_n S_{mn} = A_m e^{j\Psi_m}. \tag{1-8}$$

The phases of the column coupling coefficients Ψ_m are important in determining the scan capabilities of phased array. Each Ψ_m is a function of the column index $|m|$. Experimental evidence (Figures 1-3 and 1-4) indicates that Ψ_m is almost exactly proportional to the column index $|m|$ and hence proportional to the physical separation $|m|d_x$ between the m^{th} column and the reference element (0, 0).

This linear phase delay with distance can be understood from the physical mechanism causing column coupling. All elements in the m^{th} array column are excited with the same amplitude and phase; all elements outside this column are terminated in a resistance Z_o. The individual antenna elements in the m^{th} column are Huygens sources. Their fields add to produce a linear phase front parallel to the array column, when observed at distances which are great: in comparison to a wavelength, and in comparison to the interelement spacing. The wave travels across the array face at a uniform velocity, since the phase delay

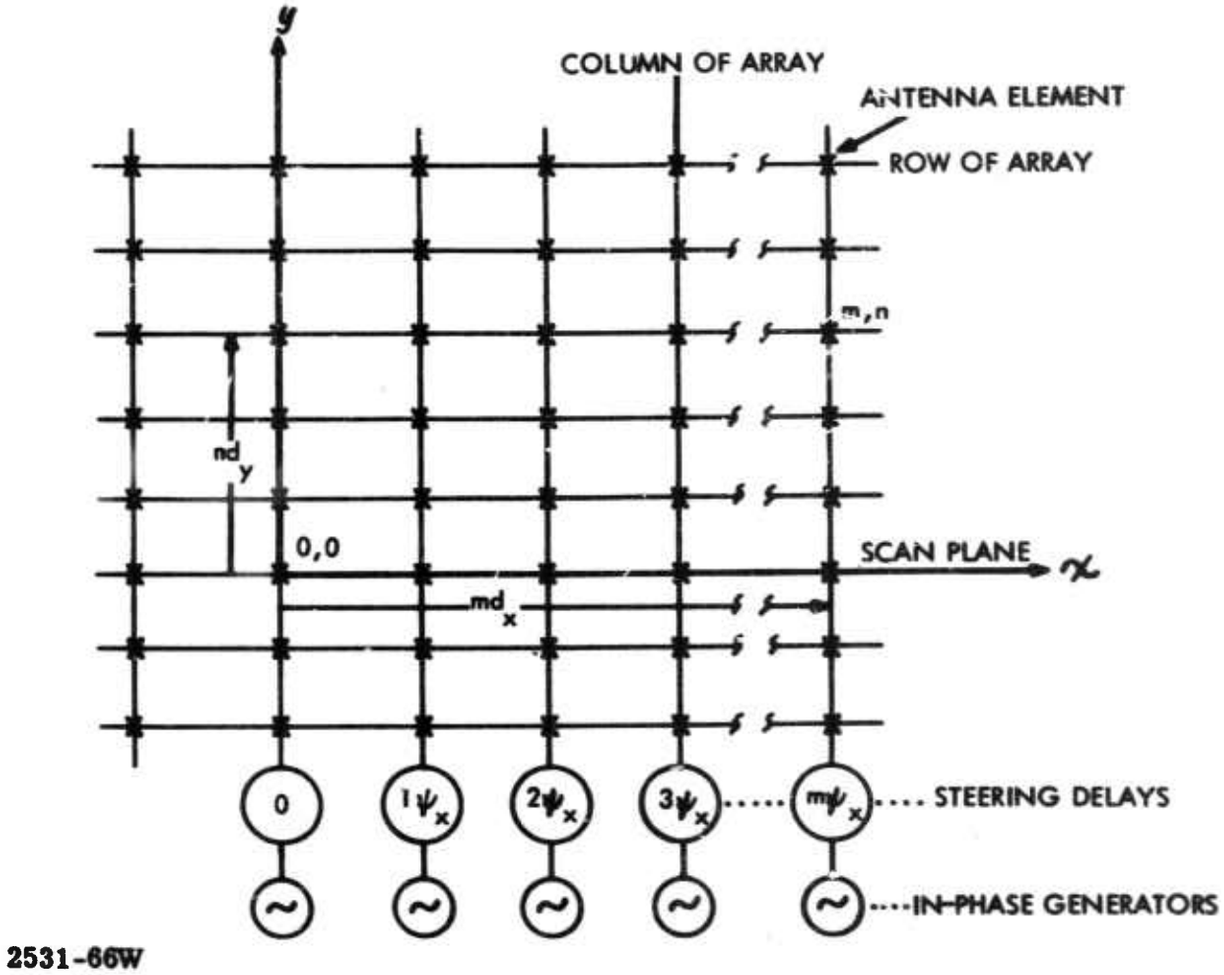

Figure 1-2. Array Column Steering

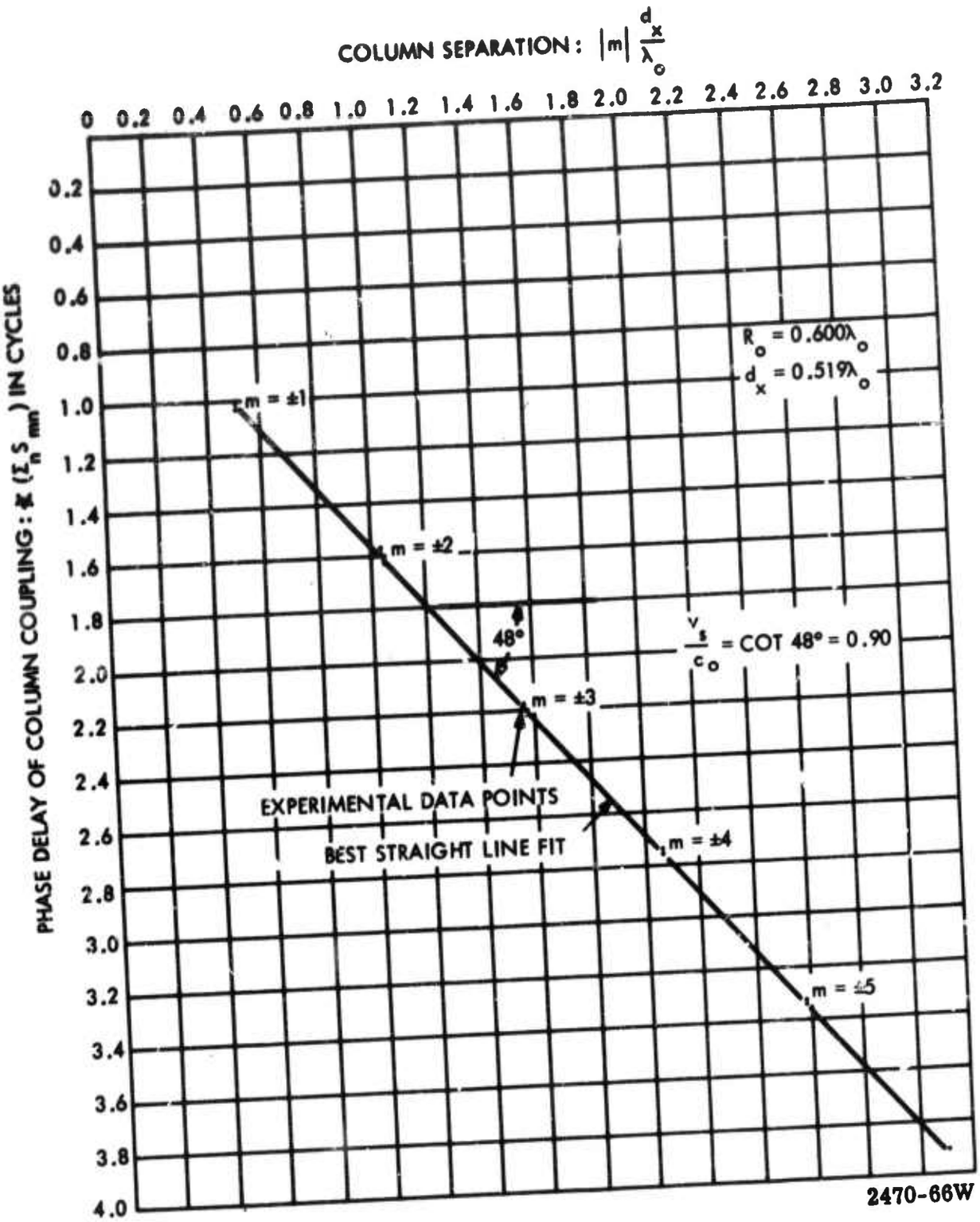

Figure 1-3. Phase of Column Coupling for Linearly Polarized Coaxial Horns

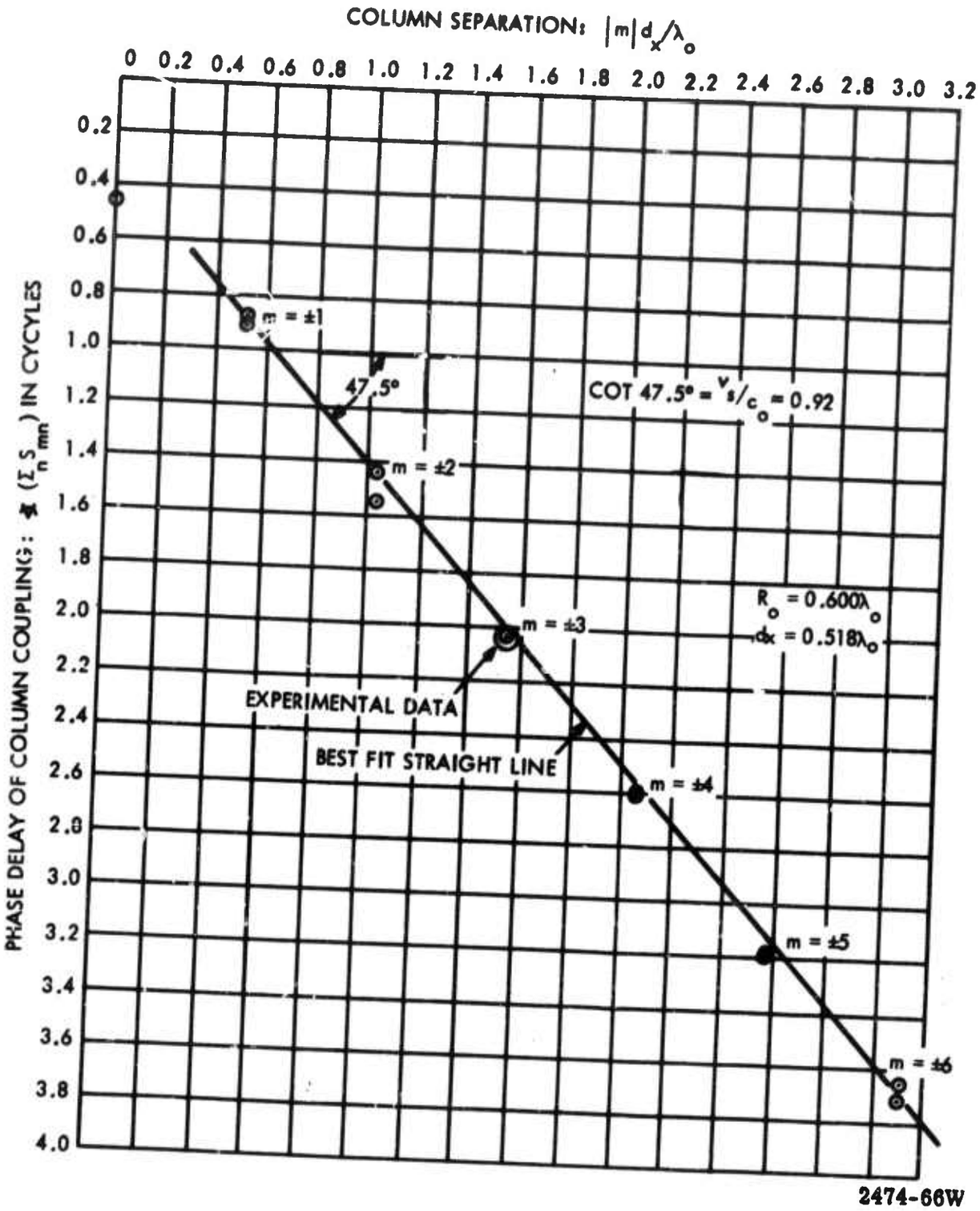

Figure 1-4. Phase of Column Coupling for Circularly Polarized Coaxial Horns

Ψ_m is proportional to distance $|m|d_x$. This wave is intercepted by consecutive passive antenna elements which absorb and scatter part of the traveling wave. The reference element (0, 0) can be thought of as a "probe" which loosely couples and samples the surface fields generated when the m^{th} column of the array is driven. Changing $|m|$ effectively moves the "probe" across the array face in discrete increments equal to the intercolumn spacing d_x. This is the physical explanation of the column coupling coefficients defined in equation (1-8).

The phase of the column coupling coefficient Ψ_m is a symmetric function of the column index $|m|$. This functional dependence could be expressed in a power series

$$\Psi_m = a + b|m| + c|m|^2 + \cdots \tag{1-9}$$

The coefficients a, b, c, $\cdots$ are constants in any given array. From Figures 1-3 and 1-4 and from the heuristic argument above, we see that a and b are the dominant terms in the series. The remaining terms are negligible for coupling via a wave traveling across the array face at a uniform velocity.

Define "$\bar{\Psi}$" as the mean slope of the coupling phase Ψ_m vs. $|m|$. An effective wave number "K_s", wavelength "λ_s" and phase velocity "v_s" can be defined in terms of this mean phase delay per column $\bar{\Psi}$ computed or measured at the discrete antenna terminals.

$$\bar{\Psi} = K_s d_x = \frac{2\pi d_x}{\lambda_s} = \frac{\omega d_x}{v_s} \tag{1-10}$$

Inserting equations (1-8), (1-9), and (1-10) into (1-7) yields the following expression for the scanning mismatch:

$$\Gamma = \sum_n S_{on} + e^{ja}\left[\sum_{m>0} A_m e^{-jm(\Psi_x - \bar{\Psi})} + \sum_{m>0} A'_m e^{+jm(\Psi_x + \bar{\Psi})}\right]. \tag{1-11}$$

Equation (1-11) has the following physical meaning: the active reflection coefficient at the reference element (0, 0) is the sum of its own mismatch plus coupling from elements in its own column [1st term in (1-11)] plus coupling from all columns to its left and right [last two series in (1-11)]. Each coupling amplitude (A_o, A_m, and A'_m) is very small

(weaker than -20 db in most cases). Large mismatches occur when many coupling contributions add in-phase. This happens when

$$\Psi_x = \pm \bar{\Psi} + 2\pi q \tag{1-12}$$

where q is any integer, Ψ_x is the array steering phase increment per column given in equation (1-6), and $\bar{\Psi}$ is the mean coupling phase delay per column (equation (1-10)). Equation (1-12) gives an infinite set of critical scan directions. Typically, only $q = \pm 1$ correspond to critical scan angles in real space ($|\sin \theta_{sc}| < 1$). These critical scan directions are determined by:

$$\left|\sin \theta_{sc}\right| = \left(\frac{\lambda_o}{d_x}\right) - \left(\frac{c_o}{v_s}\right) \tag{1-13}$$

For scan angles at or near θ_{sc}, the consecutive steering phase advances just match the mutual coupling delays, and many coupling contributions add in-phase to produce a large mismatch. For a given array (d_x/λ_o) is known and (v_s/c_o) can be obtained either analytically or via measurements. Equation (1-13) shows that, for any given radio frequency and array design, the critical scan angle is the arc sine of the difference between the inverse electrical spacing and the inverse coupling velocity.

The critical scan angle (producing large mismatch) will now be compared to the scan angle θ_{sgL} causing an end-fire grating lobe

$$\left|\sin \theta_{sgL}\right| = \frac{\lambda_o}{d_x} - 1 \tag{1-14}$$

Comparing equations (1-13) and (1-14), we find that the critical scan angle θ_{sc} is smaller than the scan angle θ_{sgL} causing an end-fire grating lobe, when $v_s < C_o$, as is the case when mutual coupling is via a slow wave.

Measurements in arrays of linearly polarized coaxial horns, circularly polarized coaxial horns, and linearly polarized rectangular horns all show coupling at velocities substantially less than the velocity of light.

This fact is very important in phased array design. Typical array design procedure selects the interelement spacing so as to place the grating lobe at the edge of real space for maximum radar scan angles. This can result in serious radar degradations (large

impedance mismatch, large radiation loss, and polarization distortion) at lesser scan angles within the design coverage objectives of the array. These degradations are a consequence of the in-phase accumulation of many small coupling contributions, and hence could go undetected in the analysis or measurement of antenna element performance in small array samples.

1.4 ZENNECK SURFACE WAVE

Array antenna elements of several types appear to couple via surface wave propagation across the array face. The resultant column coupling coefficients (equation (1-8)) have heuristic and measured properties similar to the classic Zenneck surface wave.[2,18] Surface wave theory has been effective in interpreting the coupling measurements and in analyzing the effect of dielectric sheets and hemispheric radomes on scan performance of these arrays. Antenna elements known to support slow wave propagation include the TE_{11} mode coaxial horn of the shape shown in Figure 1-5, and the TE_{10} mode rectangular waveguide radiating end-on.[11]

This section contains a brief description of the classic Zenneck surface wave followed by its application to several important problems in phased array radar.

The lowest order surface wave mode propagating over a metal ground plane is TM_0. Array antenna elements can be thought of as perturbations in such a ground plane. These perturbations influence the surface wave velocity and extract power from the surface wave through mutual coupling and scattering. (Interelement spacing is such as to provide coherent back radiation at an angle equal to the critical scan direction and with a scattering phase which would reduce the direct element radiation in this direction.) Thus, the planar array can be thought of as a periodically loaded slow wave structure whose surface wave velocity determines the radar scan coverage (equation 1-13).

The macroscopic properties of surface waves can be analyzed independently of the detail surface structure producing the wave retardation (i.e., a dielectric sheet and a trough surface can be designed to have the same surface wave properties, at large distances from the surface irregularities). Consequently, it is desirable to know these surface wave properties independently of the launching and propagating structures. Barrow and Cullen[2] have derived relationships between the tangential propagation constant "γ", the orthogonal propagation constant "u", and the surface impedance "Z_s". Knowledge of any one of

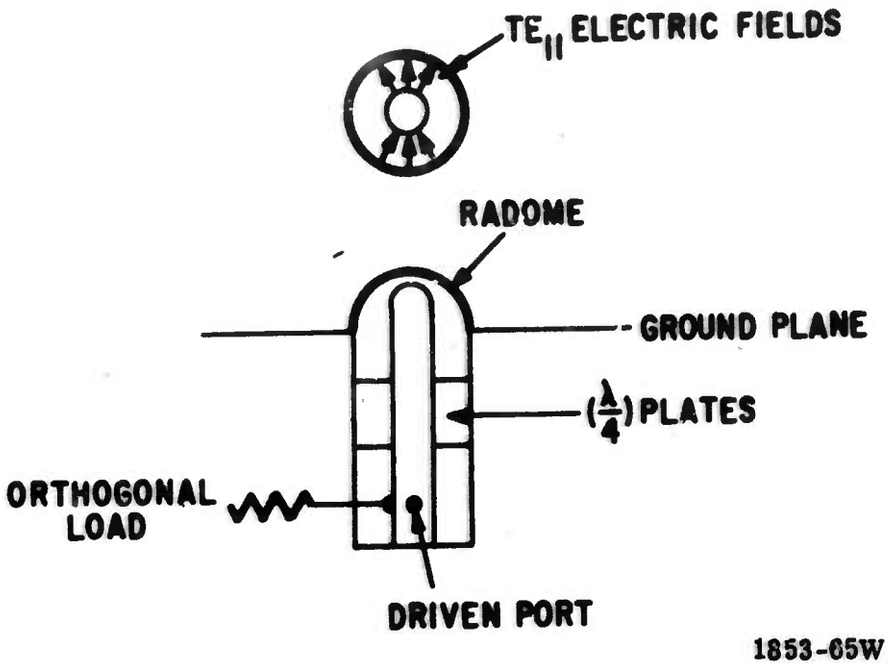

Figure 1-5. Antenna Element Cross Section

these complex numbers completely determines the other two and defines the surface wave; the relationships are

$$Z_s = \frac{j}{\omega e}\, u \quad \text{and} \quad u^2 + \gamma^2 + K_o^2 = 0 \tag{1-15}$$

where

Z_s = tangential surface impedance

γ = tangential propagation constant

u = orthogonal propagation constant

$K_o = \frac{(\omega)}{(c_o)} = \omega \sqrt{\mu_o e_o}$ = free space wave number

The surface wave, remote from the irregularities, has the form of a complex plane wave

$$Ae^{j\omega t - uz - \gamma x}. \tag{1-16}$$

The Z-axis is chosen normal to the interface (array outward normal). The X-axis is chosen along the direction of surface wave propagation. Phase and amplitude of the surface wave are independent of Y as they would be if the discrete elements in any column of Figure 1-2 were approximated by a continuous line source.

In general, Z_s, u, and γ are complex numbers. For surfaces having very low coupling and scattering losses, the surface impedance Z_s is mainly reactive. u is mainly real and γ is mainly imaginary. Thus, a slow wave propagates in the X direction; constant phase fronts are coincident with constant values of X. Antenna coupling and re-radiation losses cause attenuation in the X direction of propagation, and γ becomes complex.

1.5 COLUMN COUPLING COEFFICIENTS

Next the measured properties of the column coupling coefficients will be compared to the characteristics of the Zenneck surface wave.

Experimentally determined column coupling coefficients in two different arrays are shown in four Figures: 1-3, 1-4, 1-6, and 1-7. The phase plots (Figures 1-3 and 1-4) are linear, suggesting uniform velocity slow waves as per equation (1-16). Equation (1-16) also suggests an exponential amplitude decay with distance, $|x| = |m| d_x$. Measured

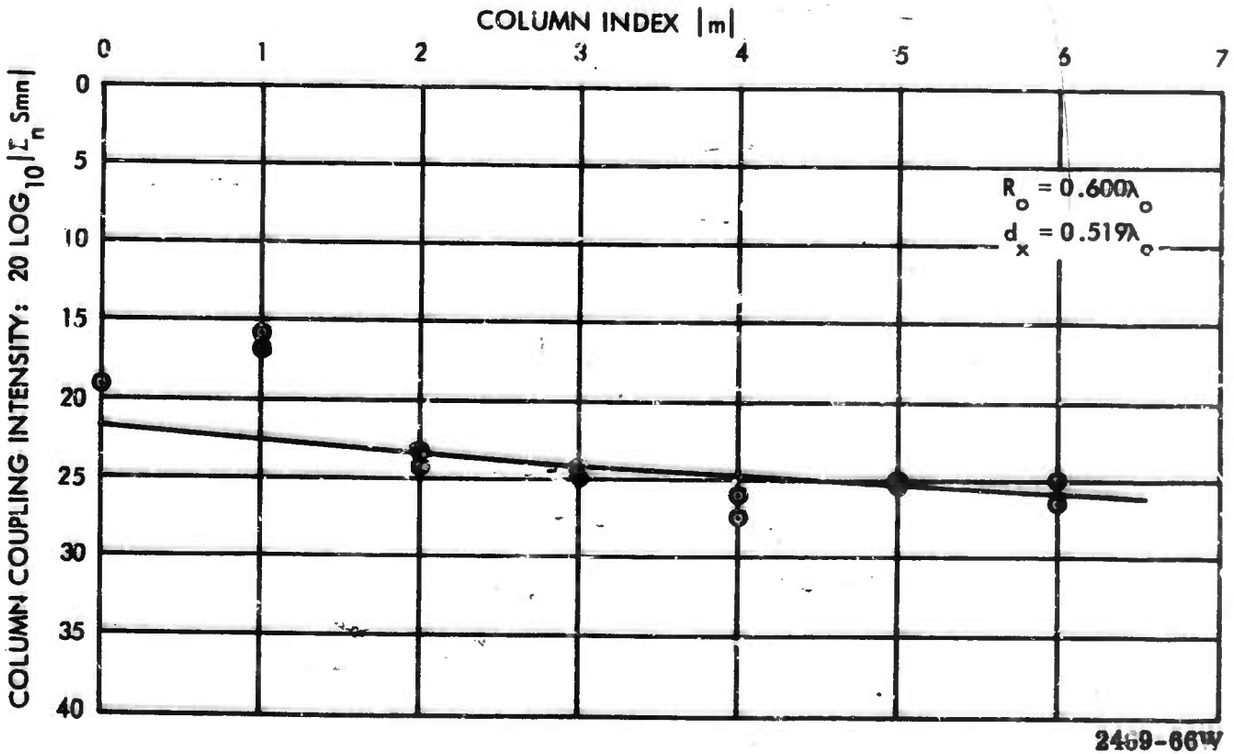

Figure 1-6. Amplitude of Column Coupling, Linearly Polarized Coaxial Horns

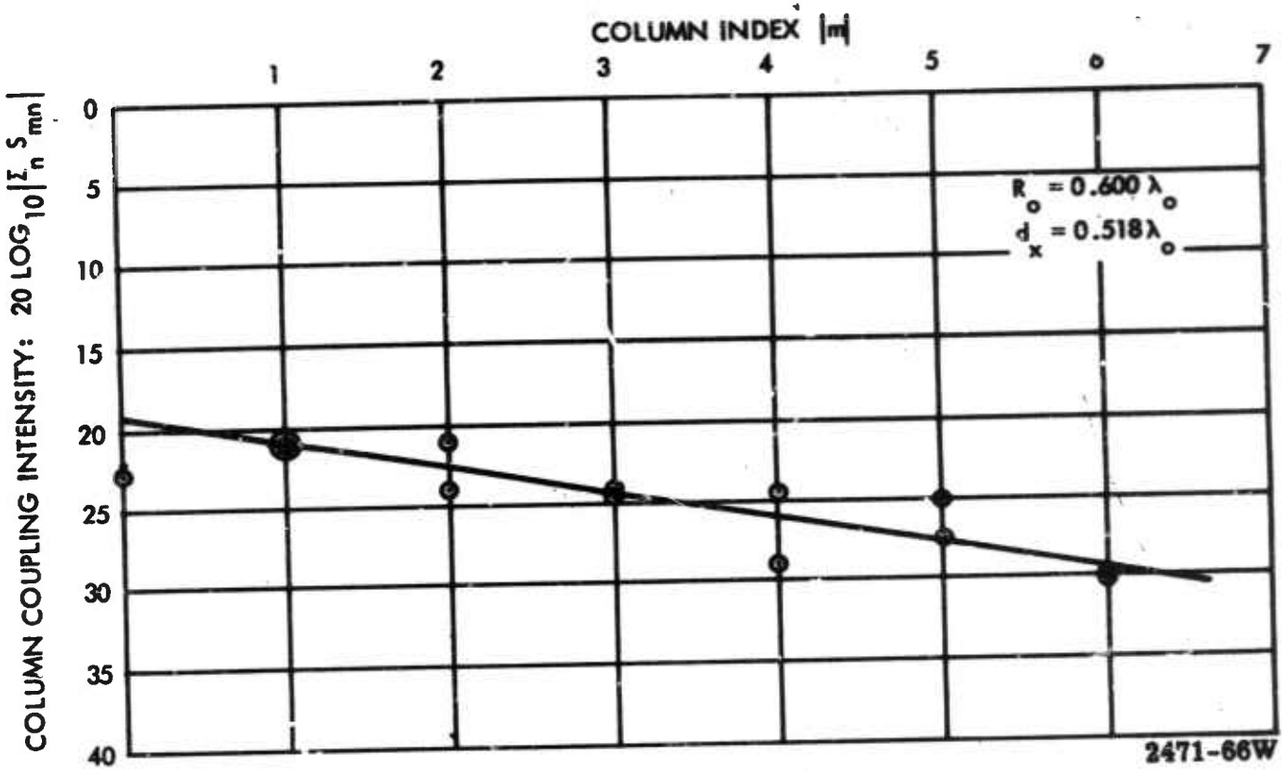

Figure 1-7. Amplitude of Column Coupling, Circularly Polarized Coaxial Horns

amplitude of the column coupling (Figures 1-6 and 1-7) also seems to fit surface wave theory for $|m| > 1$. (When $m = 0$ or ± 1, the driven column and reference element are separated by less than λ_o. Near field effects and array discreteness would be expected to cause departures from the Zenneck surface wave theory for $|m| \leq 1$.)

Array column couplings have the same X dependence as the Zenneck surface wave. In the Y direction, the array and its excitations repeat at increments d_y equal to the array spacing. Consequently, the distant column coupling coefficients will have no Y dependence, also matching equation (1-16). Thus, the measured coupling data fits well the Zenneck surface wave theory at the discrete antenna terminals.

The performance of an element in a large phased array resembles that of surface wave antennas[3] containing a driven element, a slow wave structure, and a collection of radiators. A surface wave on an array excites passive neighbors which radiate in-phase in the direction $\theta = \theta_{sc}$ as given in equation (1-13). The phase of the parasitic radiation can be opposite to that radiated directly by the element, resulting in deep holes in the element radiation pattern at the critical angle θ_{sc} (e.g., see Figure 5-1).

1.6 ACTIVE MISMATCH ESTIMATE

The scan mismatch of a phased array can be obtained in closed form for certain types of coupling. In particular, column coupling coefficients $A_m = A_o e^{-\alpha |m|}$ fit the surface wave (equation 1-16), having a line source at $\begin{Bmatrix} x = 0 \\ z = 0 \end{Bmatrix}$ and sampled at the discrete array columns. The resultant active mismatch* is

$$\Gamma(\theta_s) = A_o e^{j\alpha} \left[C_1 + \sum_{m>0}^{m} e^{-m\left\{\alpha + j(\psi_x - \bar{\psi})\right\}} + \sum_{m'>0}^{M'} e^{-m'\left\{\alpha - j(\psi_x + \bar{\psi})\right\}} \right] \qquad (1\text{-}17)$$

m and m′ are summation indices representing elements to the left and right of the reference element (0, 0), whose active mismatch is $\Gamma(\theta_s)$. M and M′ are the number of columns in

*We have assumed that array columns are driven in phase and that the surface wave phase fronts are parallel to array columns. Thus equations (1-17) and (1-18) apply to beam scanning in a principal plane of a rectangular array grid or in an intercardinal plane of a hexagonal array. These scan planes are the worst cases (least scan coverage to θ_{sc}). The mismatch Γ is a gradual function of the plane of scan ϕ_s so that equation (1-18) is valid in and near the worst scan planes, $\phi_s = 0, \pm 60°, \pm 120°$, and $180°$ for the hexagonal array and $\phi_s = 0, \pm 90°$, and $180°$ for the rectangular array.

the array on either side of the selected reference. Equation (1-17) can be simplified using the following definitions and series identity:

$$C_1 = (\sum_n S_{on}) A_o^{-1} e^{-ja}$$

$$Q = \alpha + j(\psi_x - \bar{\psi}) = \alpha + jK_o d_x (\sin\theta_s - \sin\theta_{sc})$$

$$Q' = \alpha - j(\psi_x + \bar{\psi}) = \alpha - jK_o d_x (\sin\theta_s + \sin\theta_{sc})$$

$$\sum_{m=1}^{M} e^{-mQ} = \frac{1 - e^{-MQ}}{e^{Q} - 1}$$

Equation (1-17) reduces to

$$\Gamma(\theta_s) = A_o e^{ja} \left[C_1 + \frac{1 - e^{-MQ}}{e^{Q} - 1} + \frac{1 - e^{-MQ'}}{e^{Q'} - 1} \right]. \qquad (1\text{-}18)$$

Equation (1-18) is an explicit expression for the active reflection coefficient Γ as a function of the scan angle θ_s and the coupling properties A_o, C_1, a, θ_{sc} and α. These quantities are all knowable from coupling measurements and from array scan instructions. The mismatch generally has two distinct maxima near $\theta_s = \pm\theta_{sc}$ defined by equation (1-13). For arrays having a slow decay of column coupling ($\alpha << 1$), the magnitude of maximum mismatch is

$$\left| \Gamma(\pm\theta_{sc}) \right| \cong \left| A_o (C_1 + \frac{1}{\alpha}) \right|$$

Experiments show (Figures 4-8 and 5-1) that this critical mismatch can approach unity (resulting in full reflection and no radiation) when the array is steered toward these critical scan directions $\pm\theta_{sc}$. Minima are located at $|\psi_x| = \bar{\psi}$. The width of a minima is obtained by equating real and imaginary parts of Q or Q': $|\psi_x - \bar{\psi}| = \alpha$. The width across a radiation minimum (or mismatch spike) is

$$2\left| \sin\theta_{sh} - \sin\theta_{sc} \right| = \left(\frac{\alpha}{\pi}\right)\left(\frac{\lambda_o}{d_x}\right)$$

In Section II it will be seen that the array scanning mismatch determines the element power pattern, the antenna gain, and (in the case of a radar array) the target illumination and echo intensity vs. scan. Equations (1-18) and (1-13) give the array scan

mismatch and critical scan direction θ_{sc}. This latter direction corresponds to a hole in the element power pattern and poor transmission and reception in the phased array radar. A sample antenna element pattern is shown in Figure 5-1.

1.7 THEORY OF SURFACE WAVES ON A DIELECTRIC SLAB AND ITS ARRAY APPLICATION

Next consider a specific slow wave structure consisting of a dielectric slab of thickness "t" over a perfectly conducting ground plane. (Exact analysis of this simple surface wave geometry will prove effective in explaining the effects of complex radomes on the scan performance of a real phased array.)

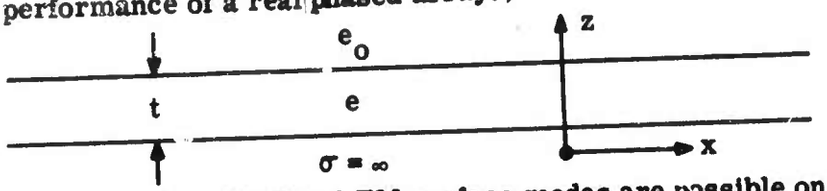

An infinite number of TE and TM surface modes are possible on the simple, flat, dielectric clad, metal sheet sketched above. Each mode is an exact solution to Maxwell's equations, fitting the dielectric boundary conditions. Each has the form of a non-uniform plane wave (equation 1-16) in the space outside the dielectric ($z > t$). Only the lowest TM_o mode is above cutoff for all frequencies, all dielectric constants "e", and any dielectric thickness "t" above a metal slab. C. Walter[4] gives the complete field expressions. Insertion of these into the wave equations yields a set of three simultaneous transcendental equations, which can be reduced to the following implicit expression for the tangential propagation constant: γ

$$\tan^2\left\{ t\sqrt{k_o^2 e + \gamma^2} - \frac{n\pi}{2} \right\} = \frac{-e^2(\gamma^2 + k_o^2)}{ek_o^2 + \gamma^2} \qquad (1\text{-}19)$$

where

n = modal index in TM_n surface mode

$\gamma = \alpha + j\beta$ = tangential propagation constant of the surface wave

$v_s = j\omega/\mathrm{im}\gamma = \omega/\beta$ = surface wave velocity

$R_v = (C_o/v_s)^2$ = inverse square of the surface wave velocity.

Determination of the tangential surface wave propagation constant γ is important for two reasons:

1) The surface wave is completely defined (equations 1-15 and 1-16) once γ is determined.

2) The propagation constant γ and the related surface wave velocity v_s can affect the performance of systems containing surface wave propagation (e.g , the scan coverage of a phased array).

γ will be evaluated for the flat, lossless, dielectric sheet in the lowest (TM_o) mode. Inserting into equation 1-19 the following two expressions:

$$n = 0 \text{ and } \gamma^2 = -\beta^2 = -\left(\frac{\omega}{v_s}\right)^2 = -k_o^2 \left(\frac{c_o}{v_s}\right)^2 = -k_o^2 R_v$$

yields

$$\tan\left\{tk_o\sqrt{e - R_v}\right\} = e\sqrt{\frac{R_v - 1}{e - R_v}}. \qquad (1\text{-}20)$$

Equation (1-20) is an implicit statement of the surface wave velocity (contained in R_v) in terms of slab dielectric constant e, and electrical thickness t/λ_o.

Figure 1-8 is a plot of the surface wave velocity (v_s/c_o) as a function of dielectric constant e, and slab thickness (t/λ_o). The abscissa is the dielectric thickness t divided by the free space wavelength λ_o. The ordinate is the normalized surface wave velocity v_s divided by c_o. Each curve represents a specified dielectric constant; e = 10 is typical of dense ceramics, e = 4 is typical of plastics, e = 2 for teflon, and e = 1.2 for some dielectric foams. It can be seen that the surface wave velocity decreases monotonically with increases in either dielectric constant and/or electrical thickness. Each curve has two asymptotes. These are

for thin, light dielectrics $\frac{v_s}{c_o} \cong 1 - 2\pi^2\left(\frac{t}{\lambda_o}\right)^2\left(\frac{e-1}{e}\right)^2$

for thick, dense slabs $\frac{v_s}{c_o} \cong \frac{1}{\sqrt{e}}\left[1 + \frac{1}{32e\left(\frac{t}{\lambda_o}\right)^2}\right]$.

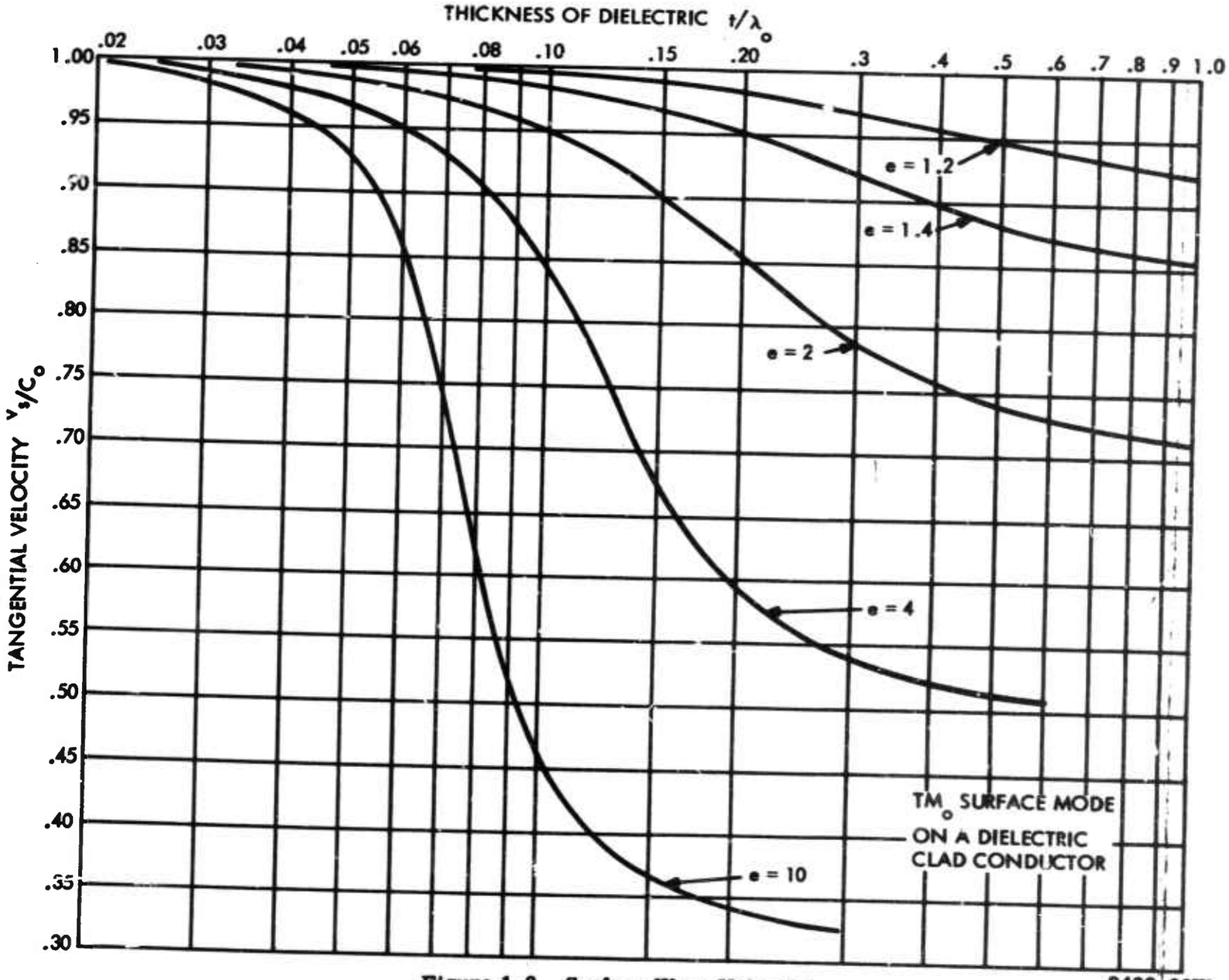

Figure 1-8. Surface Wave Velocity

Physical considerations require that equation (1-20) be real for all $t \geq 0$, for all $k_o \geq 0$, and for all $e \geq 1$. This leads to the following bounds on the surface wave velocity:

$$\frac{1}{\sqrt{e}} \leq \sqrt{\frac{1}{R_v}} = \frac{v_s}{c_o} \leq 1 \qquad (1\text{-}21)$$

The lower bound indicates that the surface wave velocity is always greater than the velocity of a plane wave in the infinite dielectric. It is approached for very thick dielectric slabs. The upper bound requires that the surface wave always travel slower than light in free space; this is approached for a very thin sheet of low dielectric constant.

An important application of surface wave theory is the determining of scan limitations of phased arrays. Two phased arrays were analyzed. In both cases array theory was corroborated by the continuous surface wave analysis. The second application included experimental verification.

The first application was an infinite, planar array of slot antennas covered by a dielectric sheet. The active array admittance determined (Appendix A) by Fourier transform techniques had poles ($Y_{act} \to \infty$) at certain critical scan angles. The corresponding surface wave velocity on the array was computed. This value of velocity was compared with the surface wave velocity on a smooth, dielectric clad metal sheet using equation (1-20). The equations for the two surface wave velocities (for the array and for the smooth dielectric sheet on a continuous conductor) agreed perfectly, indicating that the surface wave retardation caused by a dielectric cover over a slot array can be computed from the theory of surface waves over a continuous surface.

A second application of surface wave theory is the estimating of the surface wave retardation caused by hemispheric radomes over an array of coaxial horns. The coaxial horn array (MAR I type) is described in Section III. The radomes are thin dielectric hemispheres of dielectric constant $e = 6$, electrical thickness $T/\lambda_o = 0.018$, and radome height $h/\lambda_o = 0.345$.

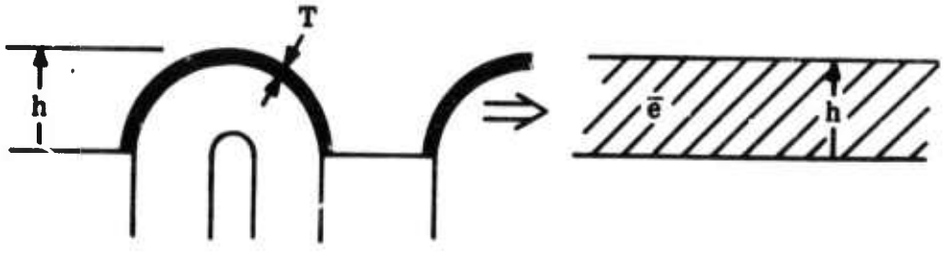

This real array geometry (sketched at left) is too complex for exact surface wave solution. An electrostatic analog (suggested by R. Gordon, Sylvania Electric) of the hemispheric radome consists of a uniform flat dielectric slab having the true radome height and an effective dielectric constant given by the formula

$$\bar{e} = \frac{eV_d + e_o V_o}{V_d + V_o} \rightarrow 1.36$$

where

V_d = volume of the hemispheric dielectric radome/unit area of array

V_o = volume of air/unit area and to a height "h" above the ground.

This analog has an electrostatic capacitance per unit area approximating that of the real hemispheric radomes for electric fields perpendicular to the ground plane in the analog and parallel to the radome shell for the TM_o mode on the array. (Electric fields perpendicular to a thin radome $T = 0.018\lambda_o$ have negligible influence on surface wave velocity).

In this example, the flat sheet analog has $\bar{e} = 1.36$ and $h/\lambda_o = 0.345$. It supports only one propagating mode (TM_o) with a velocity 7.5 per cent less than the velocity of light.

The radiation nulls of the real array were measured before and after removal of the hemispheric radomes. The null shift corresponds to a 7 per cent increase in surface wave velocity, which agrees well with the 7.5 per cent velocity change calculated from the crude surface wave analog. (Array scan coverage increased 10° or more in all directions after removing the radomes and rematching the array.)

SECTION II

SCAN RELATIONSHIPS IN PLANAR PHASED ARRAYS

2.1 INTRODUCTION

Radiation performance of a planar array is a function of scan angle and usually deteriorates sharply as the scan angle θ_s approaches 90°. The exact character of this scan degradation depends on the design of the antenna element and on array geometry. However, for any given array design there exist certain fixed relationships between the scan variables, specifically:

1) radiation power density in a selected direction,

2) element radiation pattern in the array,

3) array efficiency,

4) active impedance mismatch, and

5) solid angle spanned by the radiation beam.

This section will derive equations relating these phased array scan variables.

The derivation is based on equating the power delivered by the feed lines to the power radiated by the array. It is complicated by the fact that different elements in the array can have differing radiation and impedance characteristics because of antenna, element nonuniformity, space taper, or edge effects. Effects of these array inhomogeneities are included in the subsequent analysis.

A large, planar phased array together with its coordinate system was shown in Figure 1-1. Electrical phase delays (for beam steering) were given in equations (1-2) and (1-3). The following additional symbols will now be defined:

θ, ϕ = spherical radiation angles

(θ_s, ϕ_s) = array steering direction

V_m = incident transmission line voltage driving the m^{th} antenna element

$E_m(\theta\phi)$ = electric field radiated by the m^{th} element per unit incident line voltage; with the rest of the array elements terminated in Z_o

E_Σ = field radiated by the fully excited array.

P_a = total power available from the full active array

$P(\theta_s\phi_s)$ = power radiated by the fully excited array

$\eta_a(\theta_s\phi_s)$ = array efficiency = $\dfrac{\text{power radiated by the array}}{\text{power consumed by the array}}$

$\Gamma_m(\theta_s\phi_s)$ = active reflection coefficient at m^{th} element, with array fully excited

Z_o = characteristic impedance of the transmission lines

N_o = characteristic impedance of free space = 377 ohms

2.2 POWER CONSERVATION

The total power available from a phased array is independent of scan

$$P_a = \sum_m \frac{|V_m|^2}{2Z_o} \quad .$$

The total power delivered depends on array scan direction, efficiency, and active mismatch

$$P(\theta_s\phi_s) = \eta_a(\theta_s\phi_s) \sum_m \frac{|V_m|^2}{2Z_o} \left\{1 - |\Gamma_m(\theta_s\phi_s)|^2\right\} \tag{2-1}$$

$$P(\theta_s\phi_s) = \eta_a(\theta_s\phi_s)\left\{1 - |\bar{\Gamma}(\theta_s\phi_s)|^2\right\}\left(\frac{1}{2Z_o}\right)\sum_m |V_m|^2 \tag{2-2}$$

where a mean array reflection coefficient is here defined as

$$|\bar{\Gamma}(\theta_s\phi_s)|^2 \equiv \frac{\sum_m \left[|V_m|^2 \times |\Gamma_m(\theta_s\phi_s)|^2\right]}{\sum_m |V_m|^2} \tag{2-3}$$

If the active reflection coefficient is the same throughout the array then that is also the value of the mean reflection coefficient. Otherwise, it is the weighted average given in equation (2-3).

The net radiated field intensity is the linear superposition of contributions from each antenna element in the array. The resulting summation is a function of the angular location of the observer $(\theta\phi)$ and of the direction of array electrical scan $(\theta_s\phi_s)$. The electric field radiated in the direction of scan ($\theta = \theta_s$ and $\phi = \phi_s$) is:

$$E_{\Sigma}\left(\begin{matrix}\theta=\theta_s\\ \phi=\phi_s\end{matrix}\right) = \sum_m V_m E_m(\theta_s\phi_s) = \bar{E}(\theta_s\phi_s)\sum_m |V_m| \qquad (2\text{-}4)$$

where the mean element pattern has been defined as

$$\bar{E}(\theta_s\phi_s) = \frac{\sum_m V_m E_m(\theta_s\phi_s)}{\sum |V_m|} \quad . \qquad (2\text{-}5)$$

If the element pattern is homogeneous throughout the array [5] then the mean and homogeneous element patterns are the same. Otherwise the mean pattern is a weighted average given in equation (2-5). For radiation in the direction of scan ($\theta = \theta_s$, $\phi = \phi_s$), the radiation retardation and the steering phase advance ψ_m are exact compliments for every element in the array. These canceling phases are hence deleted from the drives V_m and the element responses $E_m(\theta_s\phi_s)$ and $\bar{E}(\theta_s\phi_s)$ in equations (2-4) and (2-5).

Equation (2-4) shows that, in any scan direction, a phased array radiates a field intensity proportional to the mean element pattern. (The factor $\left\{\sum_m |V_m|\right\}$ is a constant for all scan directions.)

Total far field power radiated by a phased array is the integral of the power density over any sphere in the far field. The observer coordinates (θ, ϕ) are now treated as integration variables, and steering angles $(\theta_s\phi_s)$ are held constant during integration.

$$P(\theta_s\phi_s) = \int\int \frac{|E_{\Sigma}(\theta, \theta_s, \phi, \phi_s)|^2}{2N_o}\, da = \frac{R^2}{2N_o} \iint |E_{\Sigma}(\theta\theta_s\phi\phi_s)|^2 d\Omega \qquad (2\text{-}6)$$

Next an effective solid angle Ω_i surrounding each major radiation lobe in real space is defined

$$\bar{\Omega}_i \equiv \frac{\iint |E_{\Sigma i}(\theta\theta_s\phi\phi_s)|^2 d\Omega}{\left|E_{\Sigma i}\left(\begin{matrix}\theta=\theta_s\\ \phi=\theta_s\end{matrix}\right)\right|^2} = \frac{\iint |E_{\Sigma i}(\theta_s\theta\phi_s\phi)|^2 d\Omega}{|\bar{E}_i(\theta\phi)|^2 \left\{\sum_m |V_m|\right\}^2} \quad . \qquad (2\text{-}7)$$

Combining equations (2-6) and (2-7) yields an expression for net power radiated by the array in terms of the effective solid angle surrounding each major beam

$$P(\theta_s\phi_s) = -\frac{R^2\left\{\sum_m |V_m|\right\}^2}{2N_o} \sum_{\substack{ML\\GL}} |\bar{E}(\theta_i\phi_i)|^2 \bar{\Omega}_i \qquad (2\text{-}8)$$

where $\sum_{\substack{ML\\GL}}$ implies summation over the main lobe and the grating lobes.

Equating the net radiated power (2-8) with the net power delivered by the array (2-2) yields

$$\sum_{\substack{ML\\GL}} |\bar{E}_i(\theta_i\phi_i)|^2 \bar{\Omega}_i = \left[\frac{N_o}{Z_o R^2} \times \frac{\sum_m |V_m|^2}{\left\{\sum_m |V_m|\right\}^2}\right] \times \eta_a(\theta_s\phi_s) \left\{1 - |\bar{\Gamma}(\theta_s\phi_s)|^2\right\}.$$

The factor in square brackets is a constant C_2 for any target range and antenna illumination taper. The scan dependence is

$$\sum_{\substack{ML\\GL}} |\bar{E}_i(\theta_i\phi_i)|^2 \bar{\Omega}_i = C_2 \eta_a(\theta_s\phi_s) \left\{1 - |\bar{\Gamma}(\theta_s\phi_s)|^2\right\}. \qquad (2\text{-}9)$$

If the phased array radiates only one major lobe in real space then the left hand summation reduces to a single term describing that steered lobe

$$|\bar{E}(\theta_s\phi_s)|^2 \bar{\Omega}(\theta_s\phi_s) = C_2 \eta_a(\theta_s\phi_s) \left\{1 - |\bar{\Gamma}(\theta_s\phi_s)|^2\right\}. \qquad (2\text{-}10)$$

2.3 ARRAY SCANNING VARIATIONS

We can compare the radiation intensity in any two array steering directions $\theta_1\phi_1$ and $\theta_2\phi_2$

$$\frac{\bar{P}(\theta_1\phi_1)}{\bar{P}(\theta_2\phi_2)} = \frac{|\bar{E}(\theta_1\phi_1)|^2}{|\bar{E}(\theta_2\phi_2)|^2} = \frac{\eta_a(\theta_1\phi_1)}{\eta_a(\theta_2\phi_2)} \times \frac{1 - |\bar{\Gamma}(\theta_1\phi_1)|^2}{1 - |\bar{\Gamma}(\theta_2\phi_2)|^2} \times \frac{\bar{\Omega}(\theta_2\phi_2)}{\bar{\Omega}(\theta_1\phi_1)}. \qquad (2\text{-}11)$$

Equation (2-11) shows that the target illumination and mean element radiation power pattern are each proportional to the array efficiency (dissipative and reflective) and inversely proportional to the effective radiation solid angle $\bar{\Omega}$.

The effective radiation solid $\bar{\Omega}$ can be computed from the integral of the array radiation pattern via definition (2-7). This spherical integral contains contributions from the area of the main lobe plus contributions from the surrounding sidelobes. R.S. Elliott[21] provided equations for estimating the main lobe beamwidth and its solid angle. However, thinned arrays or arrays of Tchebyscheff design can radiate substantial power into sidelobes and this contribution must be considered in (2-7). Sidelobes of the Tchebyscheff form add an effective radiation solid angle which is approximately 1/4 of their normalized peak power times the spherical angle occupied by these sidelobes.

If the wide angle sidelobe power is negligible, and if the array is not steered close to end fire, then equation (2-11) yields the following radar scan equation:

$$\frac{\vec{P}(\theta_1\phi_1)}{\vec{P}(\theta_2\phi_2)} = \frac{|\vec{E}(\theta_1\phi_1)|^2}{|\vec{E}(\theta_2\phi_2)|^2} = \frac{\eta_a(\theta_1\phi_1)}{\eta_a(\theta_2\phi_2)} \times \frac{1 - |\bar{\Gamma}(\theta_1\phi_1)|^2}{1 - |\bar{\Gamma}(\theta_2\phi_2)|^2} \times \frac{\cos\theta_1}{\cos\theta_2} \qquad (2\text{-}12)$$

Beam field intensity and element power pattern are each proportional to the dissipative and reflective efficiency of the array times the cosine of the scan angle. Constant array efficiency and match imply a cosine element power pattern, as was pointed out in Reference 6.

The intensity of radiation from a phased array decreases with increasing scan angle according to equation (2-12). The cosine θ factor is weakest for scanning near "end-fire". A planar array having a 1° circular beam at broadside will have a 1° × 11° oval beam near "end-fire", which in a radar will contribute a two-way echo degradation exceeding 20 db. Further substantial losses can accrue from impedance mismatch,[7, 8, 15, 16, 17] usually worst when a major lobe approaches "end-fire".

In summary, equations have been derived relating several critical phased array performance figures: target illumination, antenna element pattern, array efficiency, impedance mismatch, and effective radiation solid angle. Each depends on the electrical scanning of the array $(\theta_s\phi_s)$. Element radiation pattern in a passive array and active mismatch in a phase steered array are seen to be equivalent representations of array scanning performance. Results apply to any large, planar, phased array. Included is an upper bound on wide angle performance of planar, phased array systems when perfectly matched and lossless.

SECTION III

ARRAY MEASUREMENT PROCEDURE

3.1 ANTENNA-ARRAY GEOMETRY

To check the theory discussed in the preceeding sections several arrays were assembled and subjected to extensive electrical measurements. These antenna elements, their modification, and the tests carried out will be described in the following sections.

Figure 1-5 shows the basic antenna element. This antenna and various modifications of it was used in all the tests. It is a coaxial horn consisting of a pair of concentric cylinders propagating the TE_{11} mode, as sketched in the top view of the antenna. This mode is launched by a radial probe a quarter wavelength from the bottom of the coaxial cavity. It travels up through a dielectric quarter-wave-plate, radiating circular polarization. The reverse sense circular polarization couples to an orthogonal probe and resistive load inside each antenna element. Linear polarization is obtained by removing the quarter-wave-plates.

These coaxial horn antennas were assembled in several different planar arrays, each having a uniform, hexagonal, interelement geometry and a rectangular periphery. Figure 3-1 is a photograph of an array containing 48 complete antenna elements plus 17 "dummies". The dummies were internally matched (both ports); they lacked external connections but were otherwise complete antennas. The dummies (from another application) were located around the edge of the arrays to increase its effective size.

Each antenna element was inspected physically and electrically prior to use in the array. Electrical inspection included measurement of the passive impedance match $S_{\bullet\bullet}$ and the radiation pattern (amplitude and phase) of each antenna element.

A conducting ground plane extended several inches beyond the array on all four sides. The ends of the ground plane were rolled back to reduce the effects of edge current discontinuities on radiation pattern and active impedance. The entire array was supported on a turntable for measurement of radiation patterns.

A variety of antenna and array shapes were constructed and measured to determine the effects of various array design variables on array scan performance. These variables included

1) polarization (circular and linear)

2) radomes (on and off)

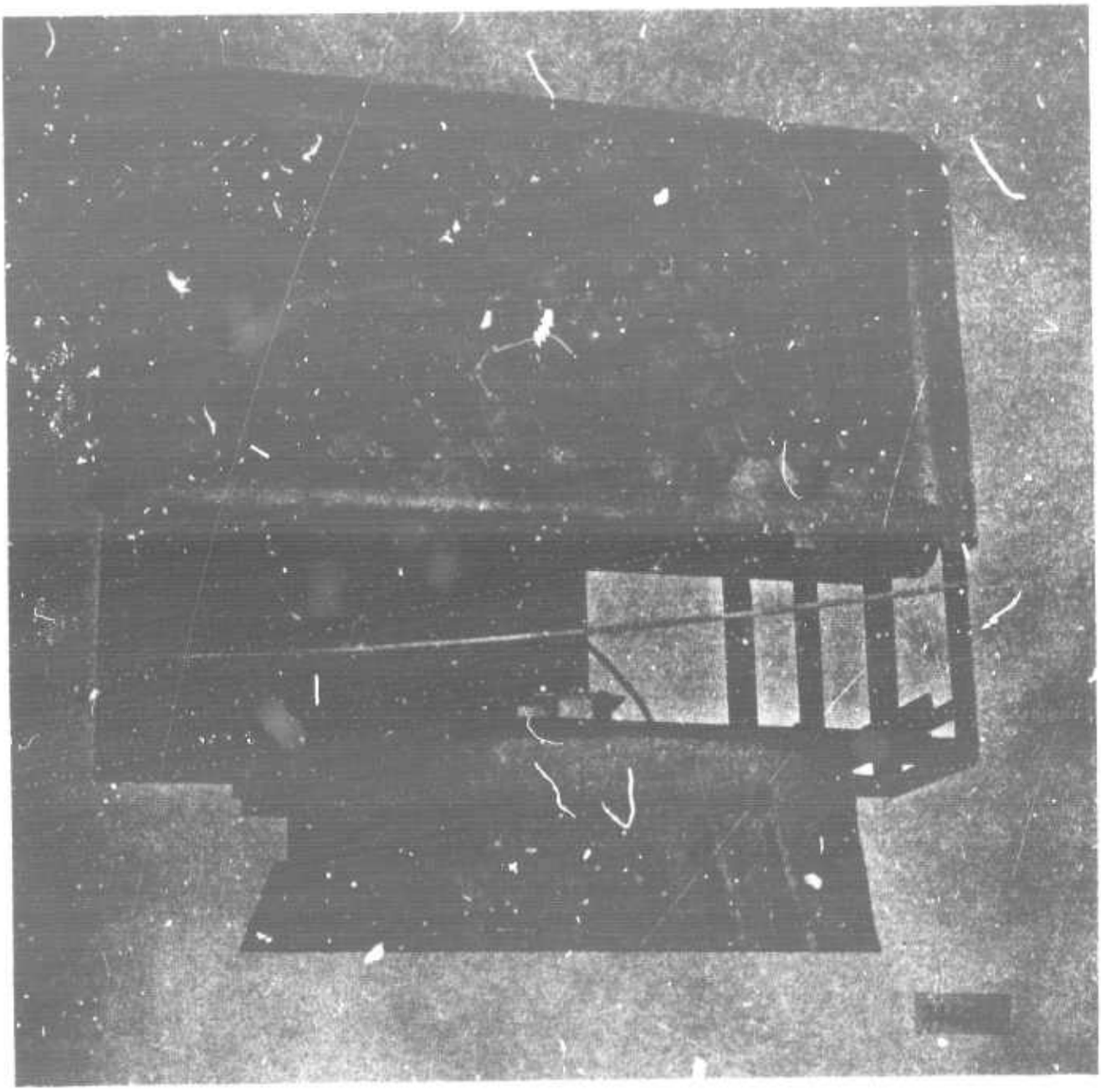

Figure 3-1. 65 Element Array

3) grooves in ground plane between elements (present or absent)

4) scan plane (two, in the x-z and the y-z planes)

5) driving impedance (five)

When any change was made all elements were changed identically to preserve array uniformity. After each array modification, radiation patterns of the central element were measured at several different microwave frequencies spaced uniformly over a 15% band. All electrical tests were in the microwave "L" band, where the free space wavelength is several inches.

3.2 RADIATION PATTERN MEASUREMENT PROCEDURE

All element radiation patterns were measured on a forty-foot outdoor antenna range (Figure 3-2). A signal source and dipole feed illuminated a four foot paraboloidal transmitter antenna. The electrical center of this transmitter beam was pointed at the central element $\begin{Bmatrix} m = 0 \\ n = 0 \end{Bmatrix}$ in the receiver array under test. Illumination was nearly uniform in amplitude and phase across the array. The array was mounted on an azimuth turntable (Figure 3-1) with the aperture of the central element directly over the turntable axis of rotation.

The feed dipole at the transmitter dish could be rotated to provide a rapid measure of the polarization ellipse of the array under test. Stepping the dipole orientation provided any linear polarization at the transmitter facility without tilting the transmitted beam. When the transmitter dipole feed is horizontal, its radiated electric field is also horizontal linear and in the plane of scan of the array. When the transmitter dipole is vertical the radiated electric field is vertical, and orthogonal to the plane of scan.

A hexagonal array (e.g., Figure 4-1) is a periodic structure. Its periodicity can be used to reduce or to check electrical measurements. Physical congruence occurs for every rotation about the normal, $\Delta\phi = 60°$. Radiation pattern cuts were taken in the intercardinal ($\phi = 0$ and $180°$) and cardinal ($\phi = 90°$ and $270°$) planes. Radiation cuts are in the intercardinal plane when the array is mounted as shown in Figure 3-1. Standing the array on end (Figure 3-3) permits radiation measurements in the cardinal plane. Most radiation patterns were measured in an intercardinal plane, where the large effective spacing between elements limits array scan coverage.

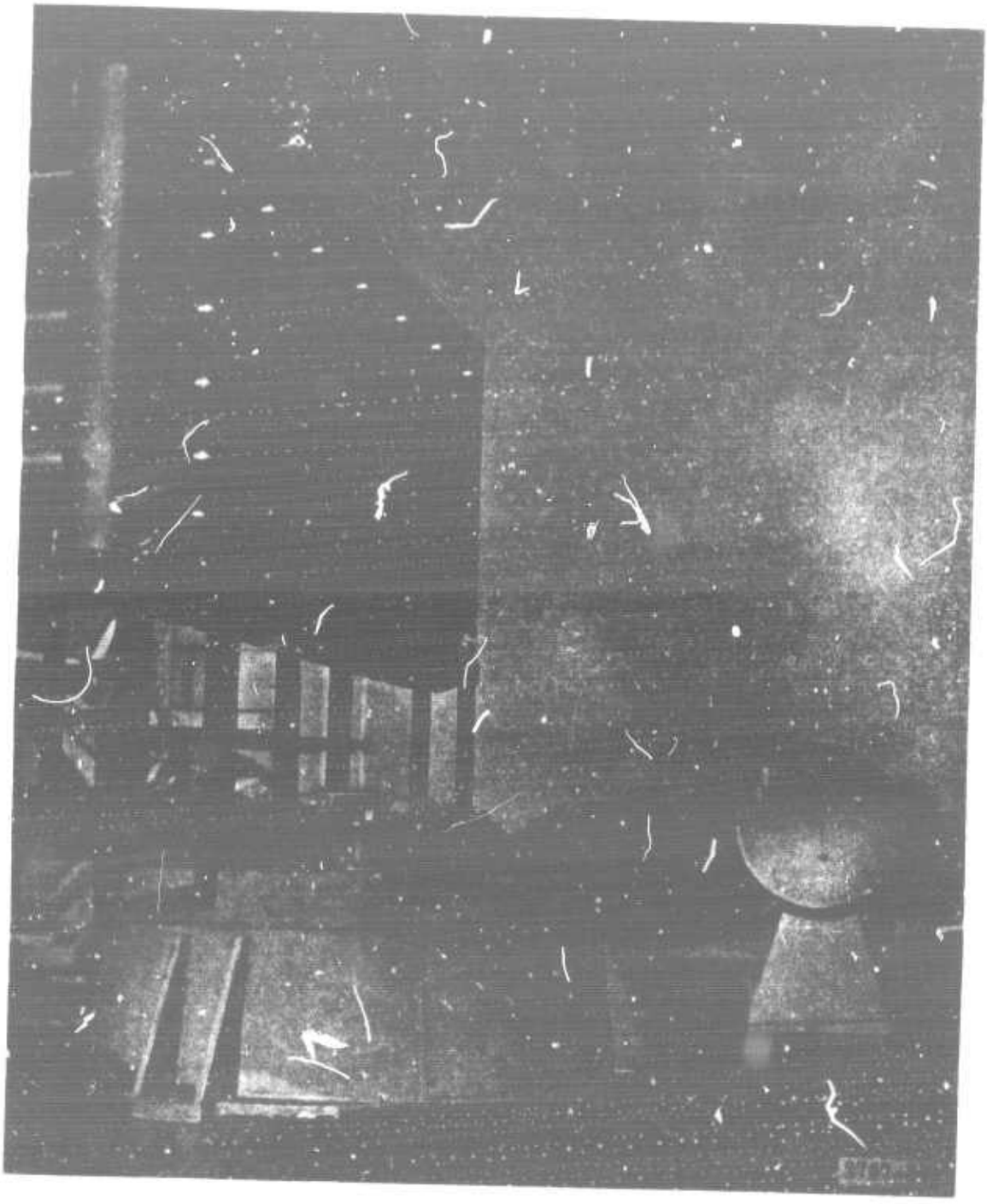

Figure 3-2. Antenna Test Range

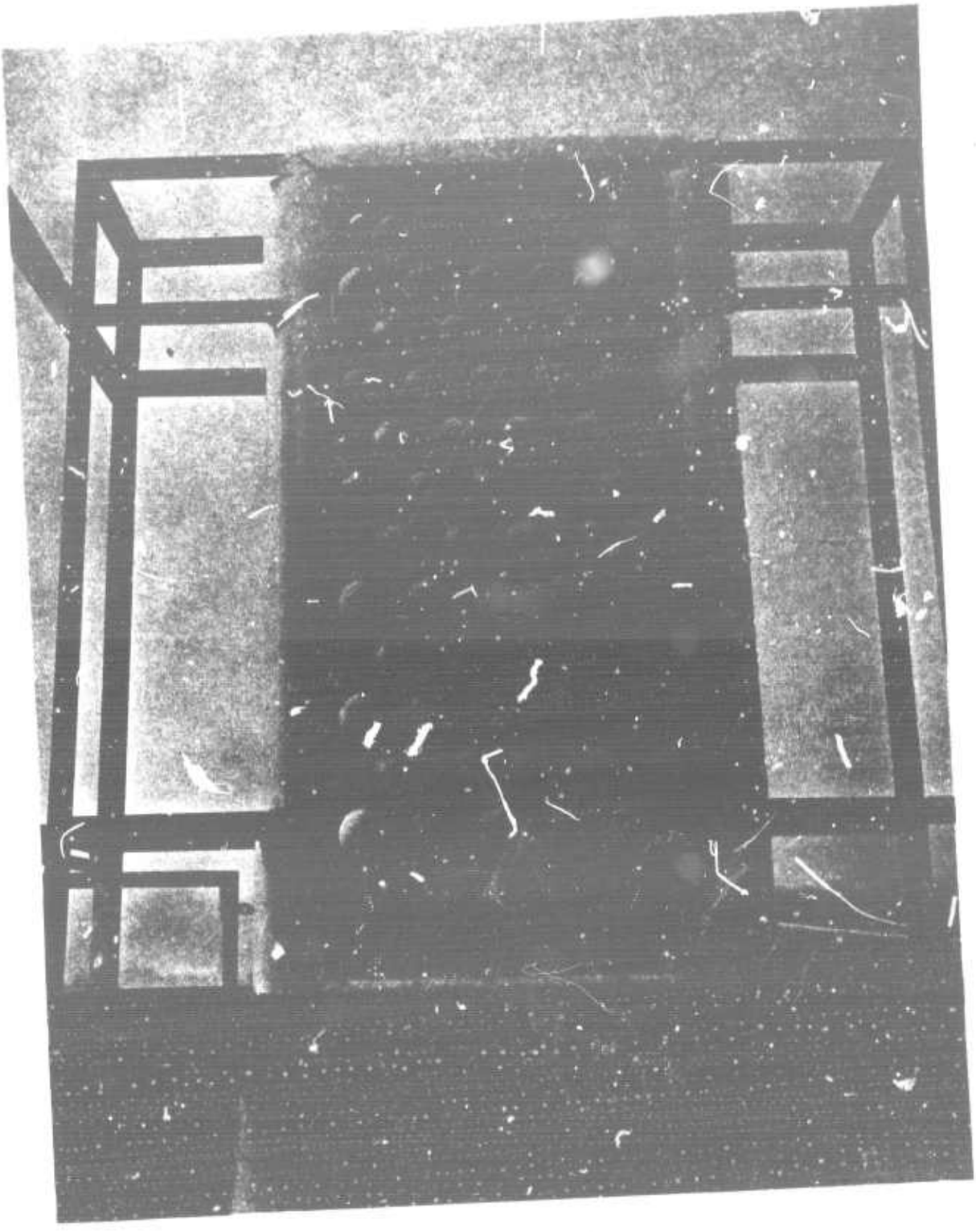

Figure 3-3. Array Rotating in Cardinal Plane

The element radiation pattern is obtained by uniformly illuminating the array (by an incident plane wave) and measuring the microwave signal received by the central (0, 0) antenna as a function of turntable rotation. The turntable rotates at a very slow uniform rate and the received power is recorded (logarithmically) as a function of turntable position (in degrees). Subsequent radiation plots will show these two variables in cartesian coordinates for various array geometries.

By reciprocity, the receive pattern of the central element is identical to its transmit pattern in the same array environment. Thus, the four foot paraboloid and its rotatable dipole feed can be thought of as measuring the linear electric field components radiated by a single driven transmitter element at the array center.

Only the radiation patterns of the individually connected central array element were measured. Section II showed that the mean element pattern contains complete information regarding the array scan capabilities, including the transmitter array gain, target illumination intensity, receiver array receptivity (or effective height), and array mismatch loss vs. scan. Measurement of the normalized element radiation pattern at an angle θ from broadside yields the normalized active array radiation (gain) when steered to this same scan angle ($\theta_s = \theta_1$).

Scan performance of a phased array depends on the character of the beam forming network interconnecting the antenna elements. Frequently, each antenna element connects individually to an amplifier or other isolating device, having uniform impedances Zg. This phased array radiation performance is reproduced in the radiation pattern of the central element when all the neighbors are terminated in the same Zg. In this study, Zg = 50 Ω, except where stated otherwise.

3.3 MUTUAL COUPLING MEASUREMENT PROCEDURE

In a phased array every antenna element couples to every other element. Each coupling coefficient is a complex quantity whose amplitude and phase depend on the inter-element separation and direction, and on other antenna design factors. These coupling coefficients and known antenna element excitations together completely determine the antenna active impedance (equation 1-1) and the array scan capability.

The procedure used to measure the coupling coefficients is based on the scattering matrix representation. The coupling coefficient S_{mn} is defined as the complex ratio of

signal received at the $(m, n)^{th}$ element, to that delivered to the central $(0, 0)^{th}$ element. A transmitter was connected to the central element $\begin{Bmatrix} m = 0 \\ n = 0 \end{Bmatrix}$ and all neighbors were terminated in 50 Ω coaxial resistors. A matched receiver was then connected sequentially to each of the neighboring antenna ports; the amplitude and phase of the signal received at each port was recorded. These measurements give one row (or column) of coupling coefficients in the square, symmetric, non-unitary, scattering matrix. They are sufficient to define the active impedance (vs. scan) of the central element in a large phased array.

In a smaller array, additional coupling measurements are useful to simulate big array performance. The simulation is based on the invariance of the coupling coefficie .t under simultaneous equal translation of both transmitter and receiver. This invariance is a consequence of the periodic character of the large, uniformly spaced planar array. This invariance was verified experimentally (within 1 db in amplitude and 0.05 cycles in phase) in our test array, even for the condition in which one antenna is only one row or column away from the a ray edge. Additional coupling measurements were made with the generator connected to other than the central (0, 0) antenna, and the receiver moved sequentially to selected neighboring antennas. These measurements were used to construct an array coupling model containing up to 78 effective antenna elements.

Separate measurements were made of the amplitude and phase of each coupling coefficient. Coupling amplitude was measured with a calibrated attenuator, bolometer, and a HP-415b amplifier-meter.

The phases of the coupling coefficients were measured using the double probe phase meter shown in the block diagram (Figure 3-4). A stable sine wave oscillator feeds two microwave paths thru a power divider. The microwave path at the top and right of Figure 3-4 contains the coupled elements in the antenna array to be measured. The microwave path on the left side of the figure is the reference arm containing the precision attenuator and phase shifter. The two microwave paths recombine in a slotted line. Balance is indicated by the switched double probe method.[9]

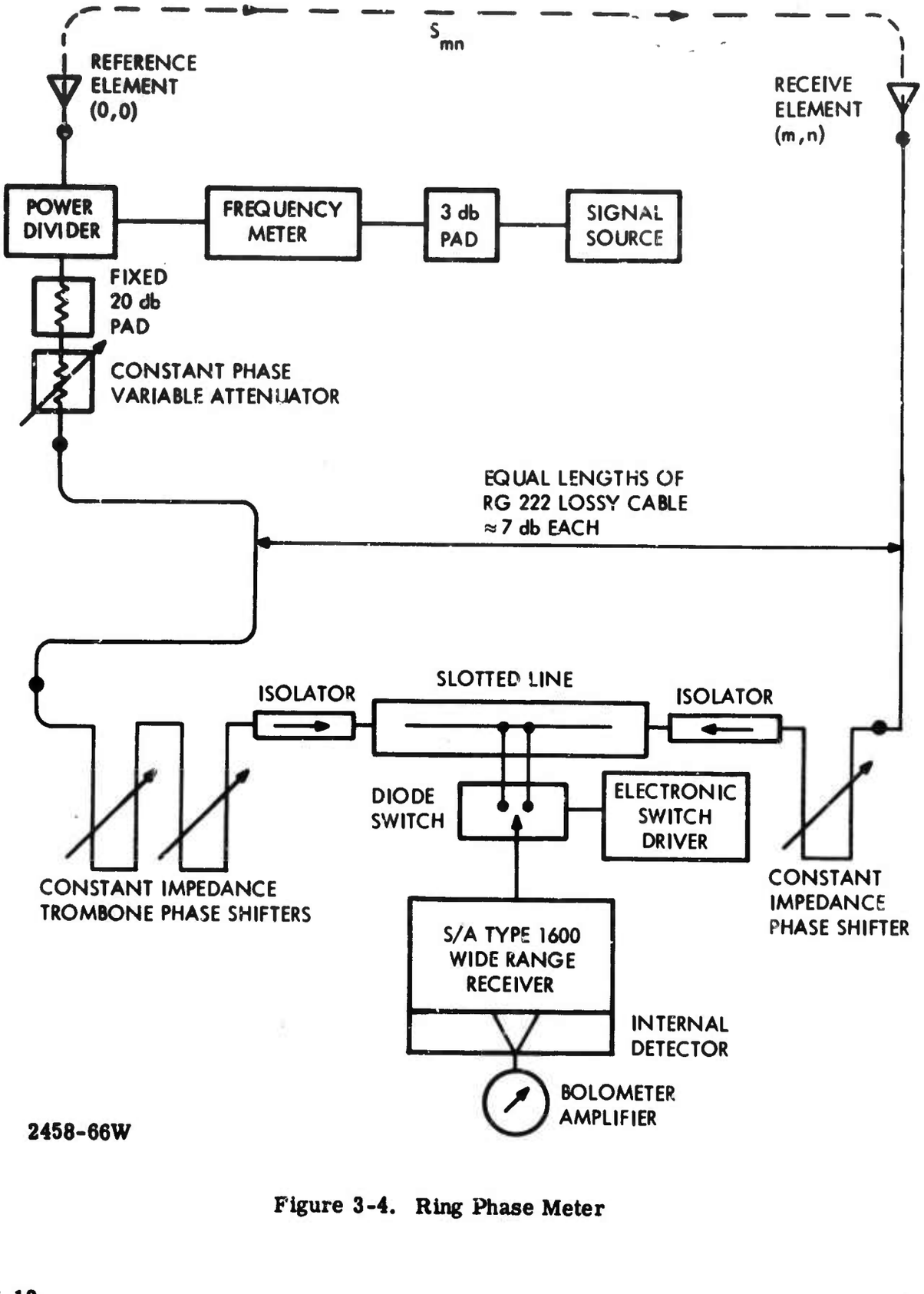

Figure 3-4. Ring Phase Meter

SECTION IV

MUTUAL COUPLING DATA

The previous section described the antenna-array geometry and the electrical procedures used to evaluate its performance. Numerous physical changes were made in the array and extensive radiation patterns were measured following each change. These tests were aimed at determining those antenna-array design factors affecting array scan performance. In addition, two sets of complex coupling coefficients were measured, one set for the linearly polarized array and one set for the circularly polarized array. The object of these coupling tests was to construct a mathematical model of the array coupling mechanism and so to better understand the radar scan limitations growing out of mutual coupling accumulation.

4.1 MEASURED COUPLING BETWEEN ELEMENTS

Figures 4-1 and 4-2 are maps showing the mutual coupling coefficients measured in arrays of linearly and circularly polarized antenna elements respectively. The central antenna element ($\begin{smallmatrix} m=0 \\ n=0 \end{smallmatrix}$) was driven and the coupled signal was measured at the terminals of each remaining antenna. Circles in Figures 4-1 and 4-2 locate the antenna elements. Two entries appear in each circle; the upper entry represents the measured coupling intensity in db, the lower entry the coupling phase delay in cycles. The coupled intensity is normalized to the wave incident on the central element. Coupling phase delays are all relative to the phase of coupling between antenna pair ($\begin{smallmatrix} m=0 \\ n=0 \end{smallmatrix}$) and ($\begin{smallmatrix} m=1 \\ n=1 \end{smallmatrix}$). The decimal part of the phase was measured unambiguously. The integer part was estimated based on a radial propagation slightly slower than light. Circularly polarized elements have an additional phase delay[10] equal to twice the angular coordinate ϕ between the coupled elements. These two phase delays were added and the nearest integer was recorded on the coupling coefficient maps.

Coupling between antenna pairs has a phase and amplitude each dependent on their separation distance R and direction ϕ. Figures 4-3 and 4-4 are plots of coupling intensity vs. distance for linearly and circularly polarized arrays respectively. Chart entries appear at the discrete positions of the antenna center lines in the array. Lines connect measured coupling between the central element and others along the principal diagonals

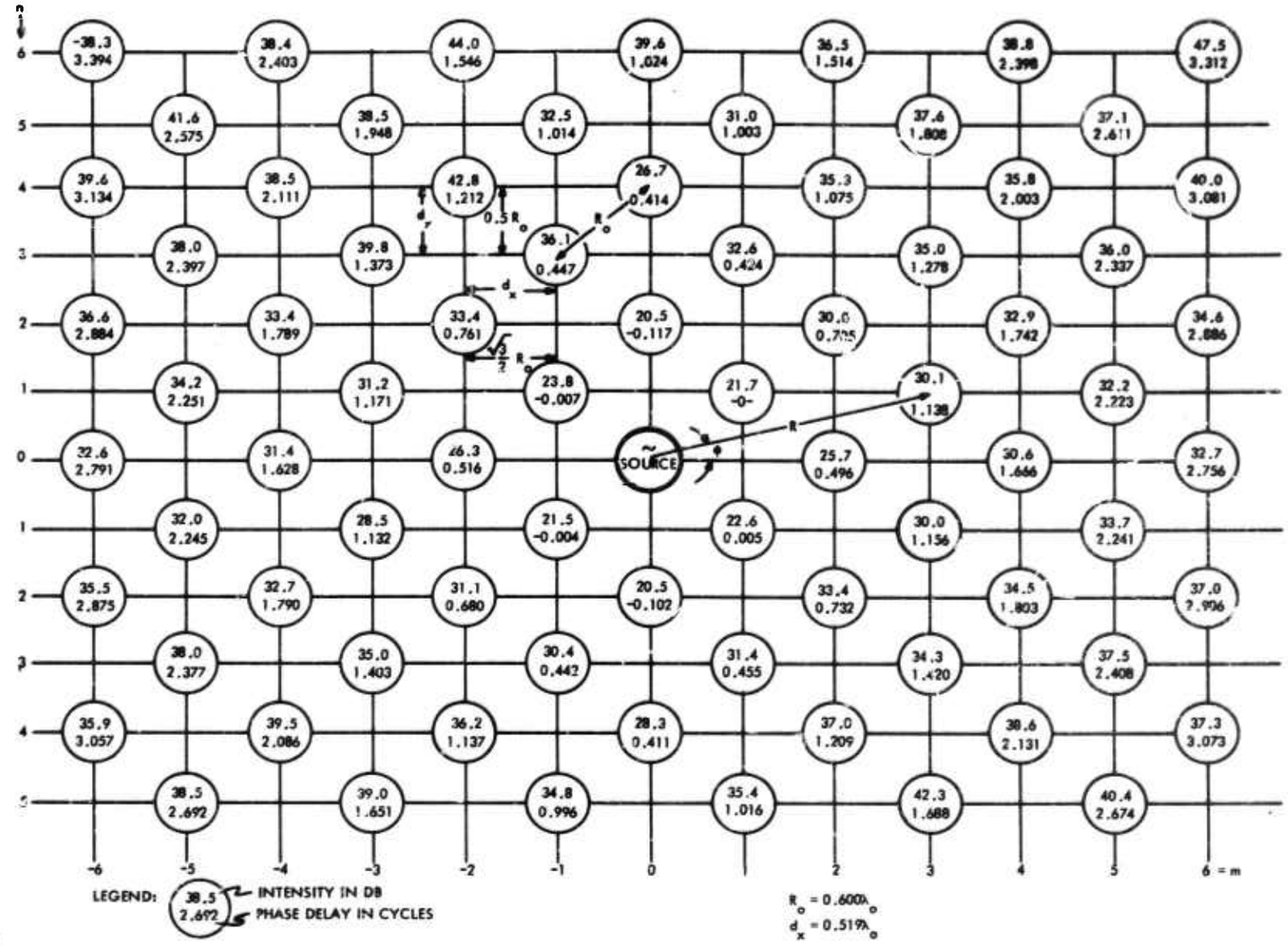

2463-66W

Figure 4-1. Array Coupling Coefficients Between Linearly Polarized Elements (E Horizonal)

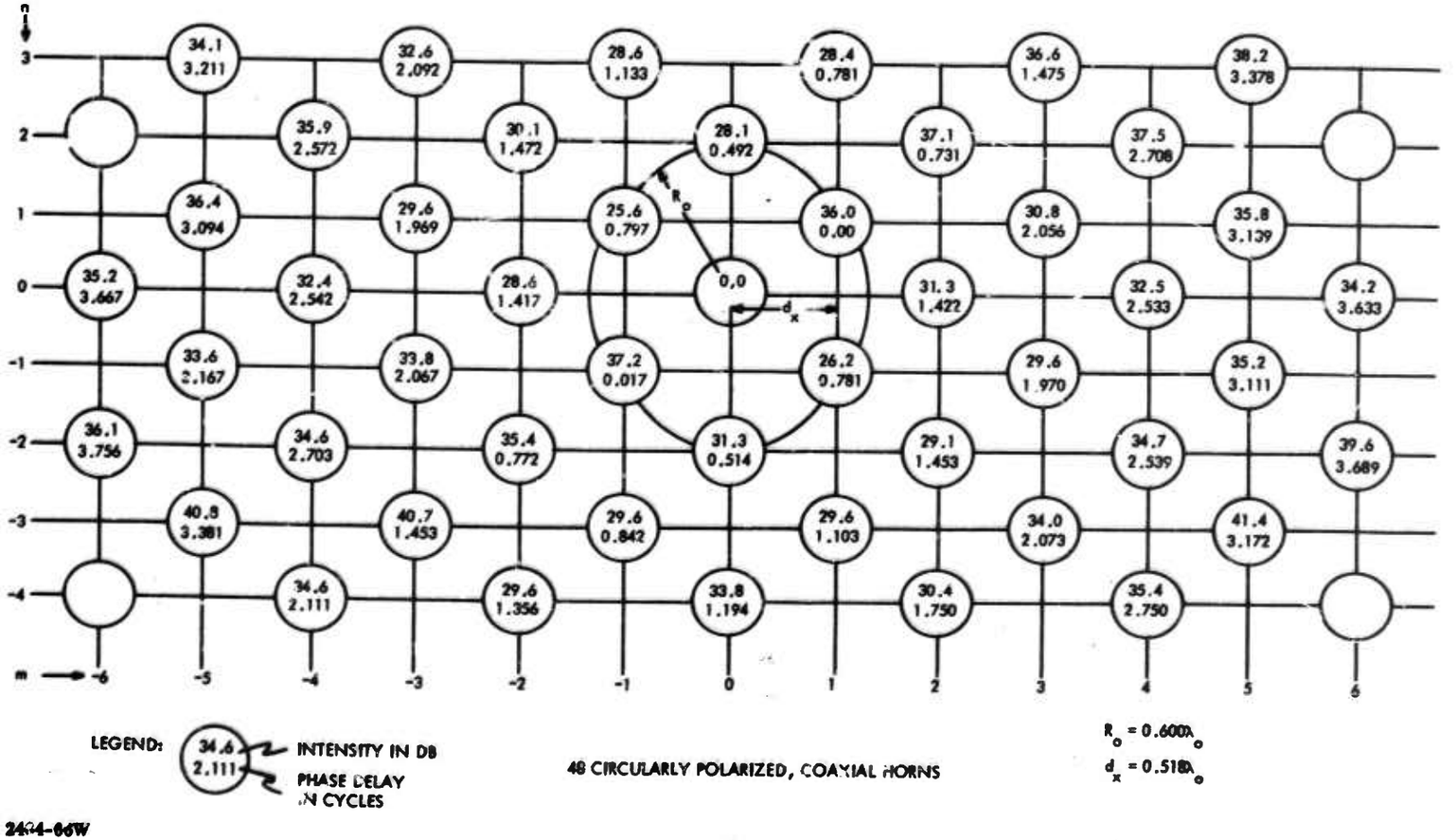

Figure 4-2. Array Coupling Coefficients Between Circularly Polarized Elements

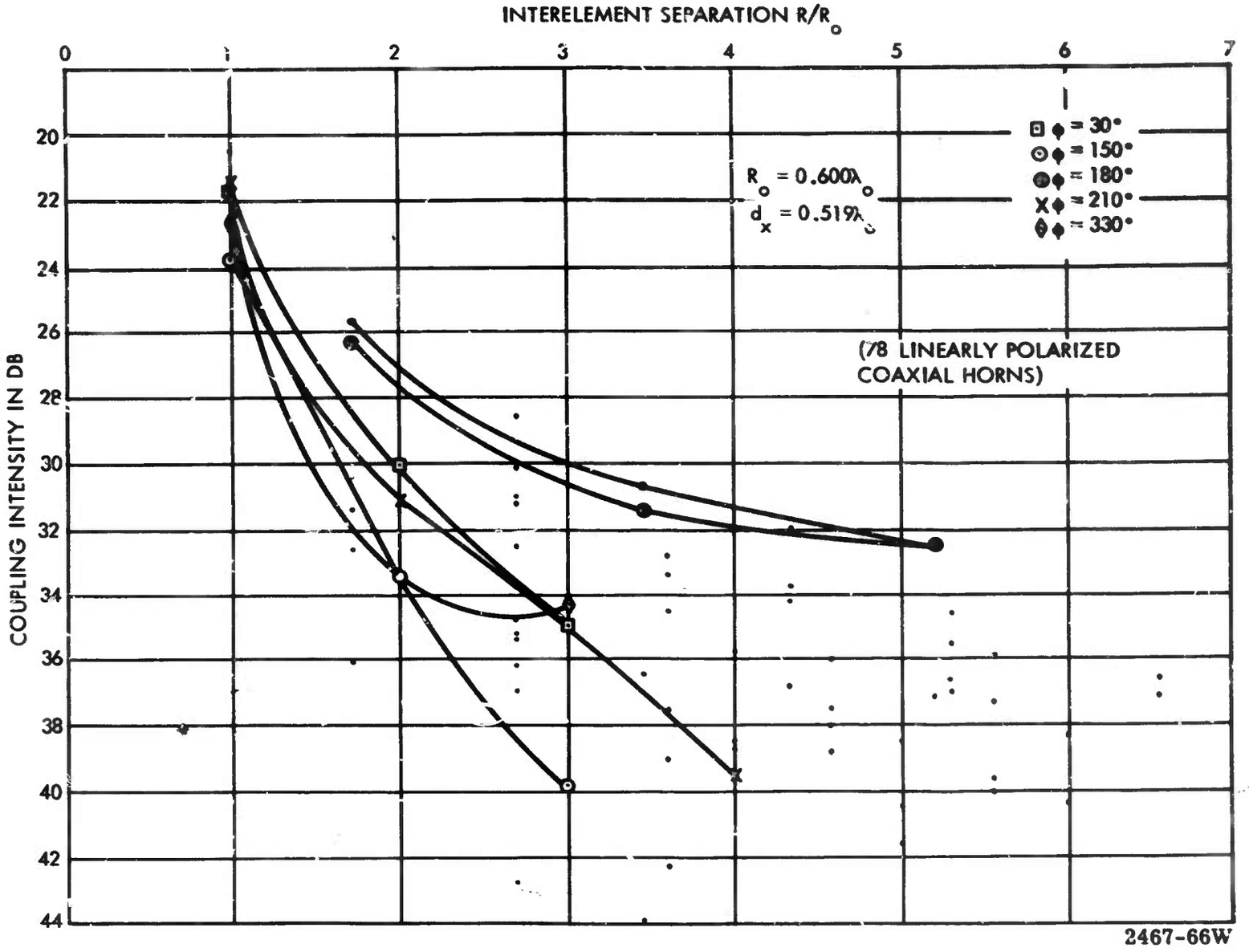

Figure 4-3. Intensity of Coupling Between Linearly Polarized Antenna Elements

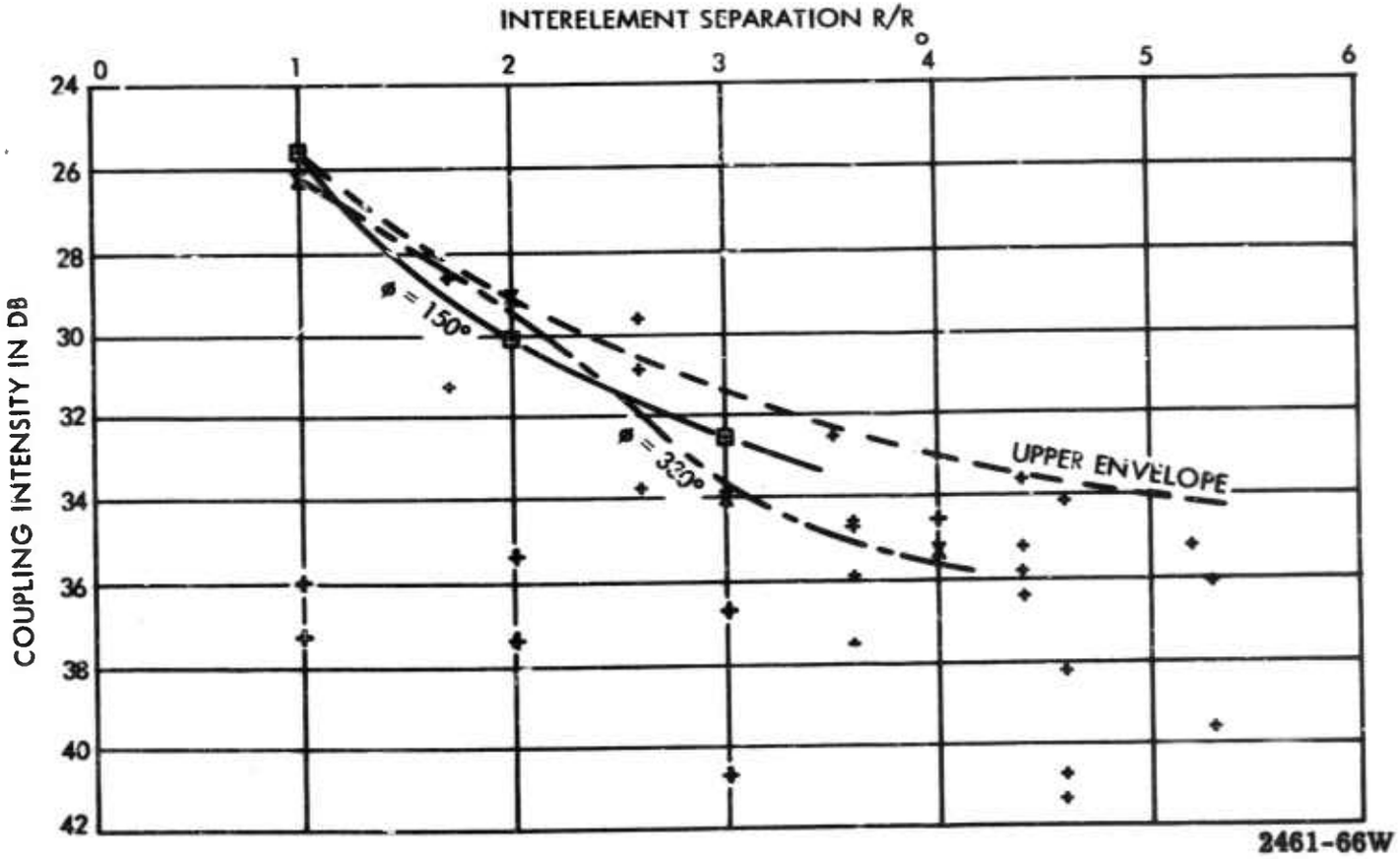

Figure 4-4. Intensity of Coupling Between Circularly Polarized Antenna Elements

of the array ($\phi = \pm 30°$ and $\pm 150°$). Isolated points represent coupling to elements off the principal diagonals. Coupling intensities in Figures 4-3 and 4-4 differ both in initial value and in decay rate. Linearly polarized coupling is generally more intense than circularly polarized coupling. Very little power is delivered to the orthogonal ports in a linearly polarized array, whereas in the circularly polarized array appreciable power is coupled into the reverse screw sense port. This orthogonal component of the mutual coupling is dissipated within the antenna elements. It does not appear at the antenna terminals and is not included in the coupling data presented here.

Figures 4-5 and 4-6 show the phase delay of the coupling vs. distance R and direction ϕ. In the linearly polarized array (Figure 4-5), coupling phase delay is linearly proportional to distance R and nearly independent of angles ϕ. In the circularly polarized array (Figure 4-6), coupling delay is linearly proportional to distance R and has an additional delay 2ϕ. This latter dependence accounts for the vertical displacement of about 0.333 cycles (120 electrical degrees) between the 3 diagonal lines connecting coupling phase data in the 3 cardinal planes of the circularly polarized array (Figure 4-6).

The coupling phase delays (Figures 4-5 and 4-6) are linearly proportional to distance. This is very important. It suggests a coupling emanating from the central element and propagating radially outward at a velocity slightly less than the velocity of light in free space. The slopes of these curves suggest that the velocity of propagation is 0.90 c_o for both arrays.

4.2 COLUMN COUPLING COEFFICIENTS

Interelement coupling coefficients (obtained from array measurements) were summed along each column to obtain empirical column couplings as defined in equation (1-8). The results are plotted in Figures 1-3, 1-4, 1-6 and 1-7. Figures 1-6 and 1-7 show the intensity of the column coupling vs. column index $|m|$ or distance $|m|d_x$. For separations $|m| > 1$, the coupling wave appears to decay exponentially as suggested by the Zenneck Surface wave theory. The fit between empirical data and the exponential decay is crude and is sensitive to small measurement errors. An exact knowledge of the coupling amplitudes is not vital to the determination of the array critical scan directions; the coupling phase is the important parameter and for that a good mathematical model was developed in Section I. The analysis of coupling accumulation at the critical scan angles was based on stationary phase concepts applied to the column coupling contributions. The relative phases of the column coupling coefficients are crucial.

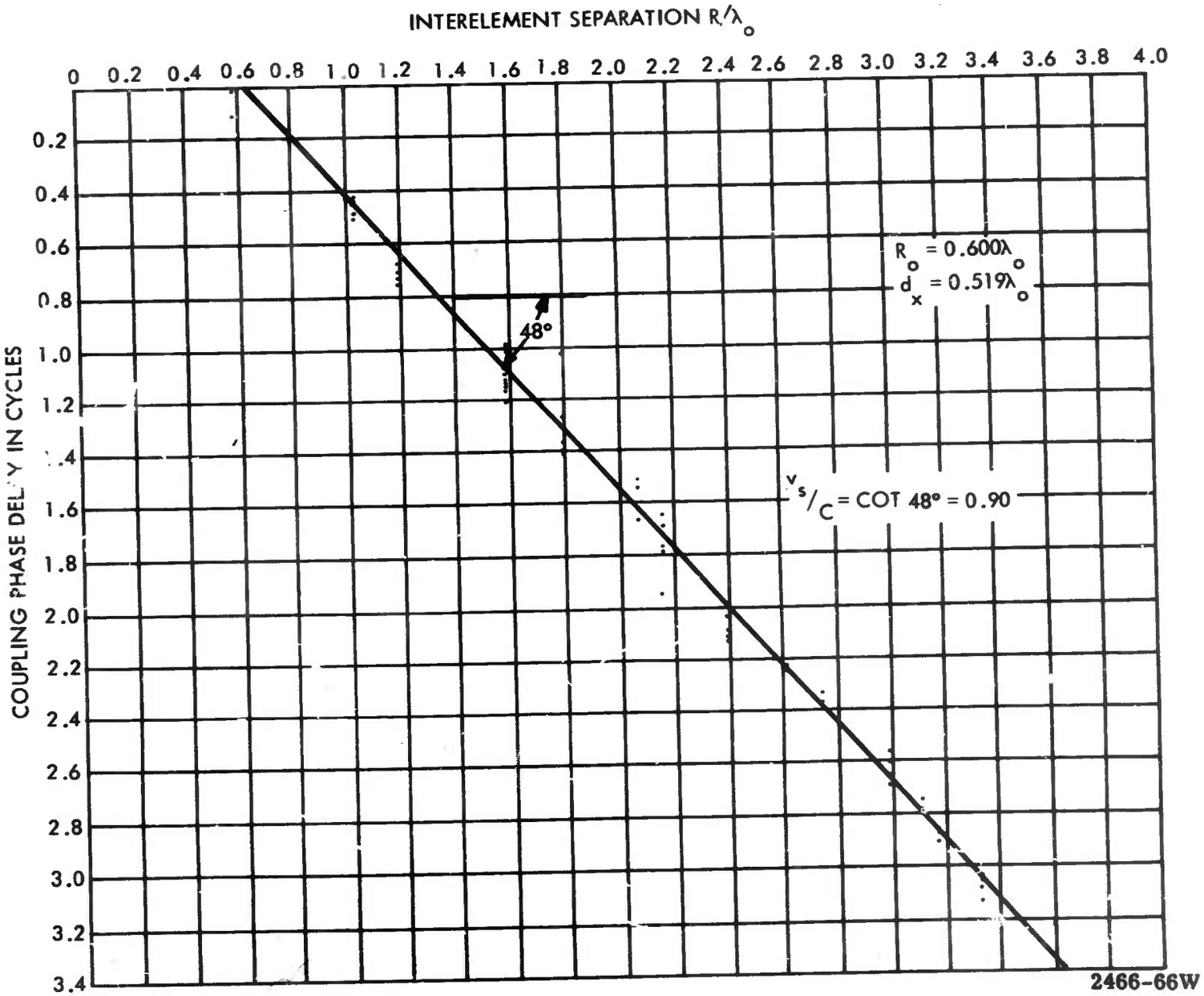

Figure 4-5. Phase of Coupling Between Linearly Polarized Coaxial Horns

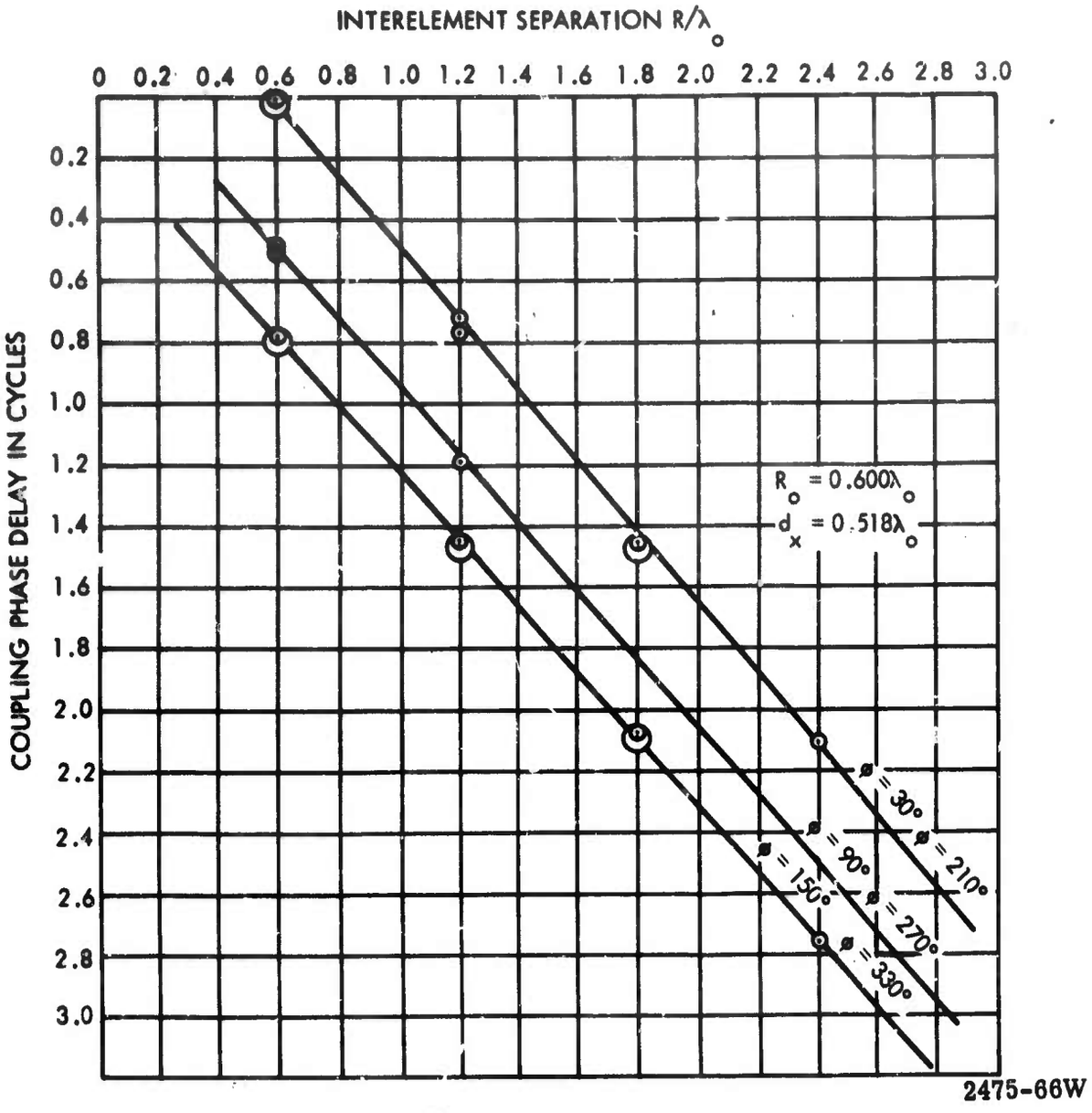

Figure 4-6. Phase of Coupling Between Circularly Polarized Coaxial Horns

Figures 1-3 and 1-4 show the phase of the column coupling coefficients vs. the distance between the coupled column and the reference element. Dots represent experimental data, and the straight line is a best fit to this data. Again, the phase linearity is excellent, suggesting a uniform velocity, slow wave, coupling mechanism similar to the Zenneck Surface Wave. Actual coupling velocity depends on array design. Empirical data in Figures 1-3 and 1-4 suggest coupling velocities of 90 to 92% in these arrays, with a probable accuracy of ±1%. The coupling velocity is nearly independent of antenna polarization and also seems to be nearly the same for element and column coupling. In the next section it will be seen that the coupling velocity depends strongly on frequency, inter-element spacing R_o, and on dielectrics. This nearly uniform coupling phase velocity and phase delay per column ($\bar{\psi}_1$) were used, in equations 1-10 thru 1-13, to identify the critical scan directions. Measured element radiation patterns show deep nulls in these same critical scan directions, as will be seen in the next section.

The straight line variation of phase delay vs. distance between columns has a direct impact on array scan performance, and on radar coverage, as a specific example. To steer a phased array in the azimuth plane, all antennas in a column are driven in-phase and consecutive columns have a uniform phase progression. Thus, a plot of array steering phase shifts vs. array column index would also be a straight line with a slope proportional to the cosine of the steering angle (equation 1-3). When the array is steered so that the steering phase advances match the column coupling delays, many coupling contributions add in-phase to produce a large electrical reflection inside the (radar) system, and relatively little transmission through the array face. This is the critical scan condition analyzed in the first part of this report.

4.3 ARRAY ACTIVE IMPEDANCE

Equation (1-4) showed that the active reflection coefficient (impedance mismatch) of any element in a phased array can be determined exactly from a knowledge of the array steering instructions (ψ_x, ψ_y) and mutual coupling coefficients (S_{mn}). For the uniform planar array being studied, the steering instructions are known from equation (1-3); the mutual coupling coefficients were measured and reported in Figures 4-1 and 4-2. The resultant array mismatch can be computed for any array scan angle. This was done in the case of the linearly polarized array scanned in the intercardinal ($\vec{E}$) plane, (ϕ_s=0).

The 77 complex coupling coefficients in Figure 4-1 were summed according to equation (1-7). The passive mismatch of the central element (S_{oo}) is quite small and independent of scan angle. It was omitted from this sum.

Figure 4-7 is a Smith plot of the array impedance change with scan angle. Best match occurs around 40°; this is confirmed by the element radiation pattern which has high corners near the same angle. Array mismatch is large and rapidly varying for scan angles between 55° and 65°. The corresponding radiation pattern had minima at scan angles slightly less than 65°. In Figure 4-7 the magnitude of the mismatch never exceeded 0.6, which appears to be a consequence of the finite array size. Larger arrays were considered, and their scanning impedances were estimated by linear extrapolation of the measured coupling data in Figures 1-3 and 1-6. Addition of four hypothetical columns on the left and four on the right of the previous array yields a 126 element array with the scanning mismatch shown in Figure 4-8. The active impedance of this array has been normalized for best impedance match near broadside. The added columns contribute very little to the active impedance of the array when scanned near broadside ($|\theta_s| < 40°$), since their coupling contributions have diverse phase angles here. The added columns significantly increase the array mismatch in the critical scan region ($55° \leq |\theta_s| \leq 65°$) where all elements added to one side of the array couple in-phase. Maximum mismatch is 0.8 at a scan angle of about 60°. Further increases in the hypothetical array size result in further increases in the estimated active mismatch near the critical scan angle.

The maximum value of the active mismatch and the depth of the corresponding radiation hole have not been determined. Measurements of the radiation patterns of a 361 element array of rectangular horns (Reference 11) and of an even larger array of coaxial horns (Appendix C) both indicate that the loss at critical scan can exceed 15 decibels (30 db in a two-way radar).

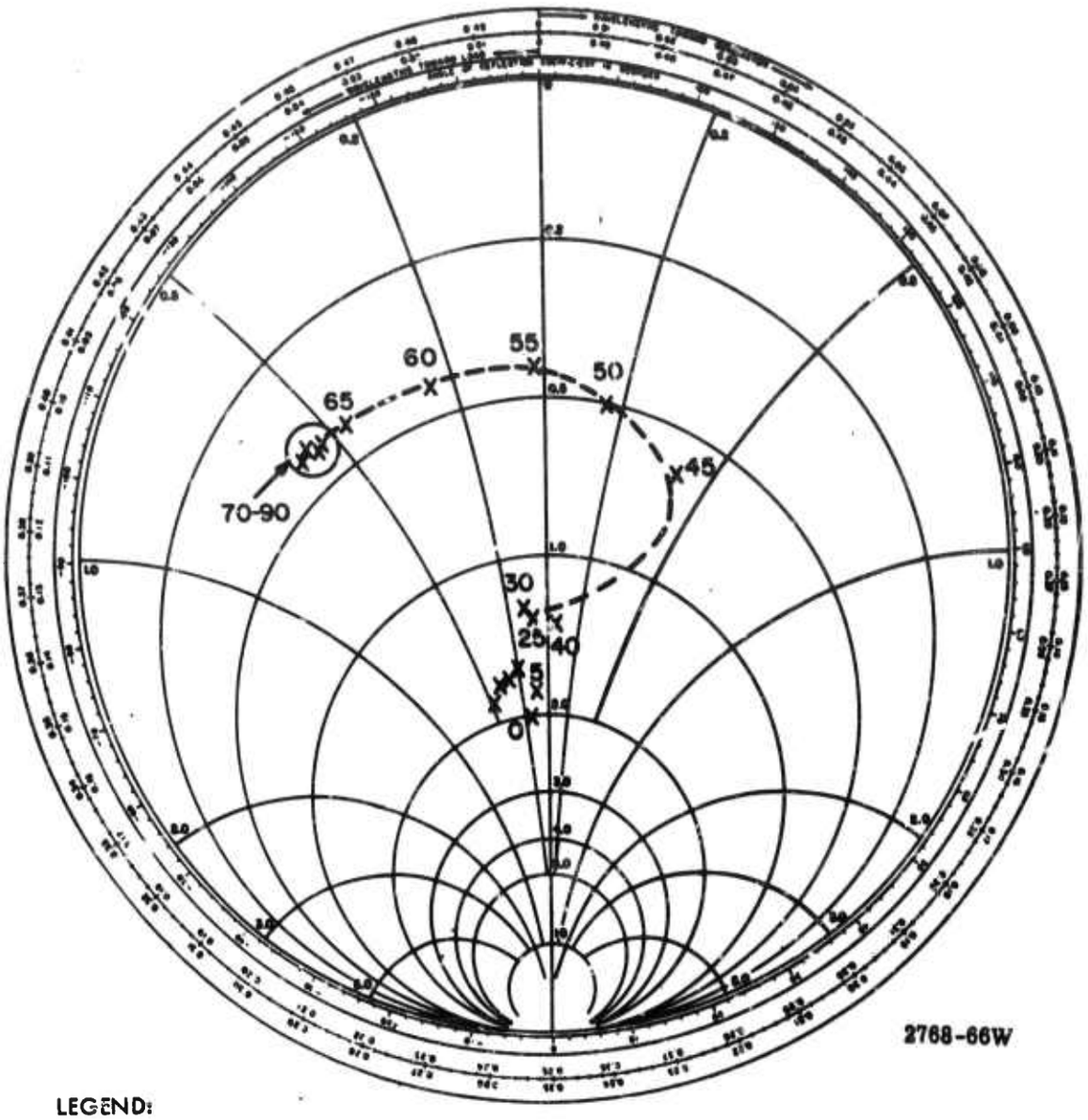

LEGEND:

X SCAN ANGLE IN DEGREES FROM BROADSIDE

Figure 4-7. Scan Impedance, 78 Effective Array Elements

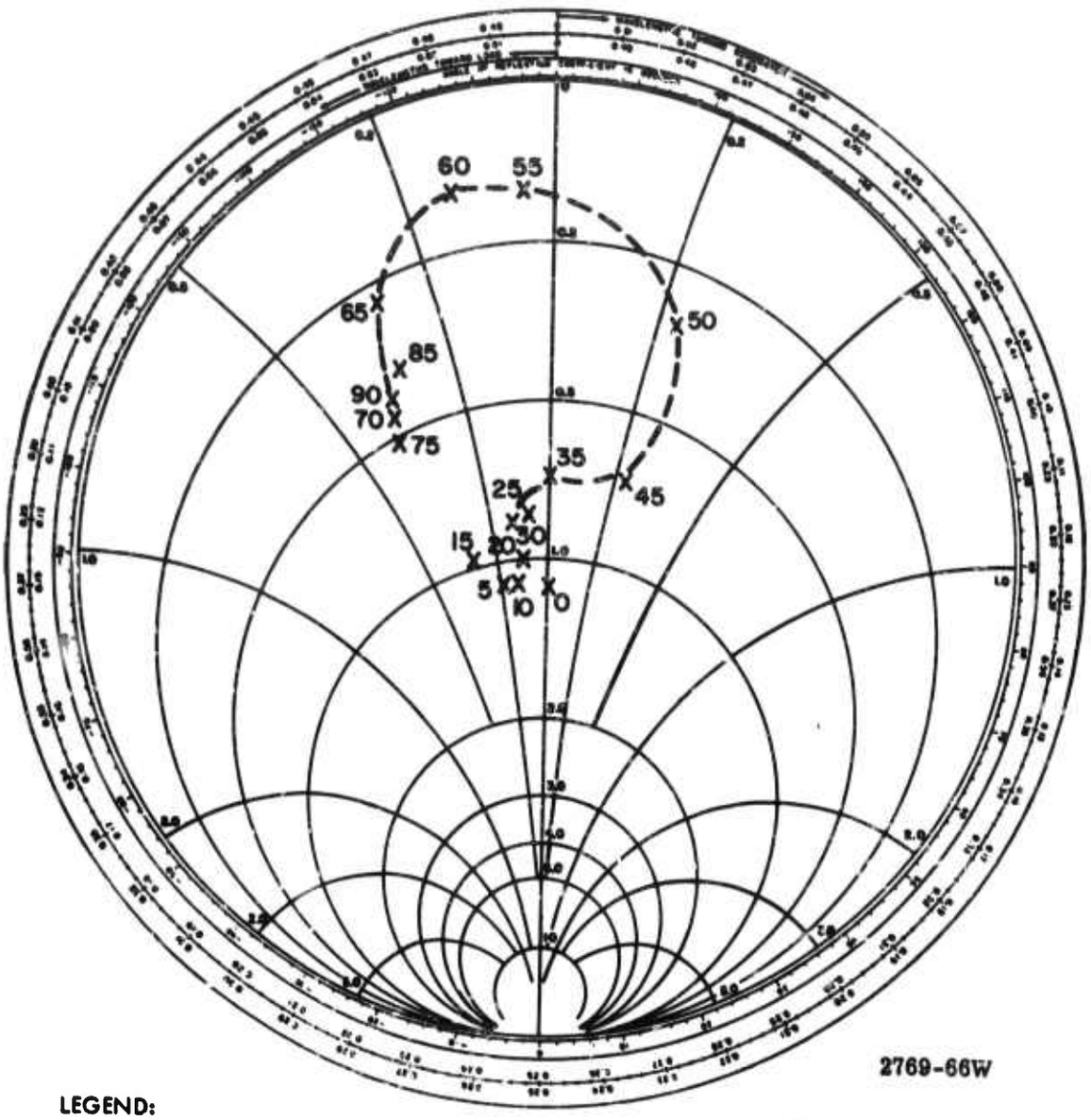

LEGEND:

X SCAN ANGLE IN DEGREES FROM BROADSIDE

Figure 4-8. Scan Impedance, 126 Effective Array Elements

SECTION V

MEASURED RADIATION PERFORMANCE

Many factors in the design of a phased array antenna influence its scan coverage. A planar array of uniformly spaced coaxial horn antennas (Figure 3-1) was the test vehicle used to evaluate the effects of some of these array design choices on scan coverage. The variables included interelement spacing, element polarization, plane of scan, presence of radomes, shape of the ground plane, generator impedance, and microwave frequency. Each of these changes was made uniformly on every element in the array. Each physical change was followed by measurement at several test frequencies of the radiation pattern of the central antenna element in the homogeneous array of passively terminated neighbors. Four representative radiation patterns are shown and explained. The scan coverage effects of the various array modifications are summarized simply by stating (or plotting) the presence and location of the critical scan angle in the intercardinal plane.

5.1 REPRESENTATIVE RADIATION PATTERNS

Figures 5-1 through 5-4 are radiation patterns of the coaxial horns under a single test condition. The antennas were circularly polarized, with hemispheric radomes and grooves in the ground plane between elements. Effective interelement spacing was $d_x = 0.506\lambda_o$. Pattern cuts were in the intercardinal plane of the array. The central element was connected to a receiver and automatic recorder. All remaining antennas were uniformly terminated in open circuits, short circuits, or 50 ohm resistors as indicated. Each pattern is a cartesian plot of radiation intensity in decibels vs. radiation angle in degrees from broadside. Three radiation patterns were measured in the intercardinal plane. The first radiation pattern shows the element response to an electric field in the plane of scan; the second shows the response to an electric field perpendicular to the plane of scan; and the third shows the array polarization ellipticity and net power density vs. radiation direction.

Figure 5-1 shows the element radiation pattern for the electric field component in the plane of scan (linear horizontal polarization). Radiation intensity is nearly uniform within an angle of ±55° from broadside. (The small ripple is attributed to array edge effects.) Deep radiation holes appear around ±65°. The antenna element had been previously tested as a single element on a large ground plane. The isolated antenna pattern showed good coverage with no radiation holes. When placed in an array of like

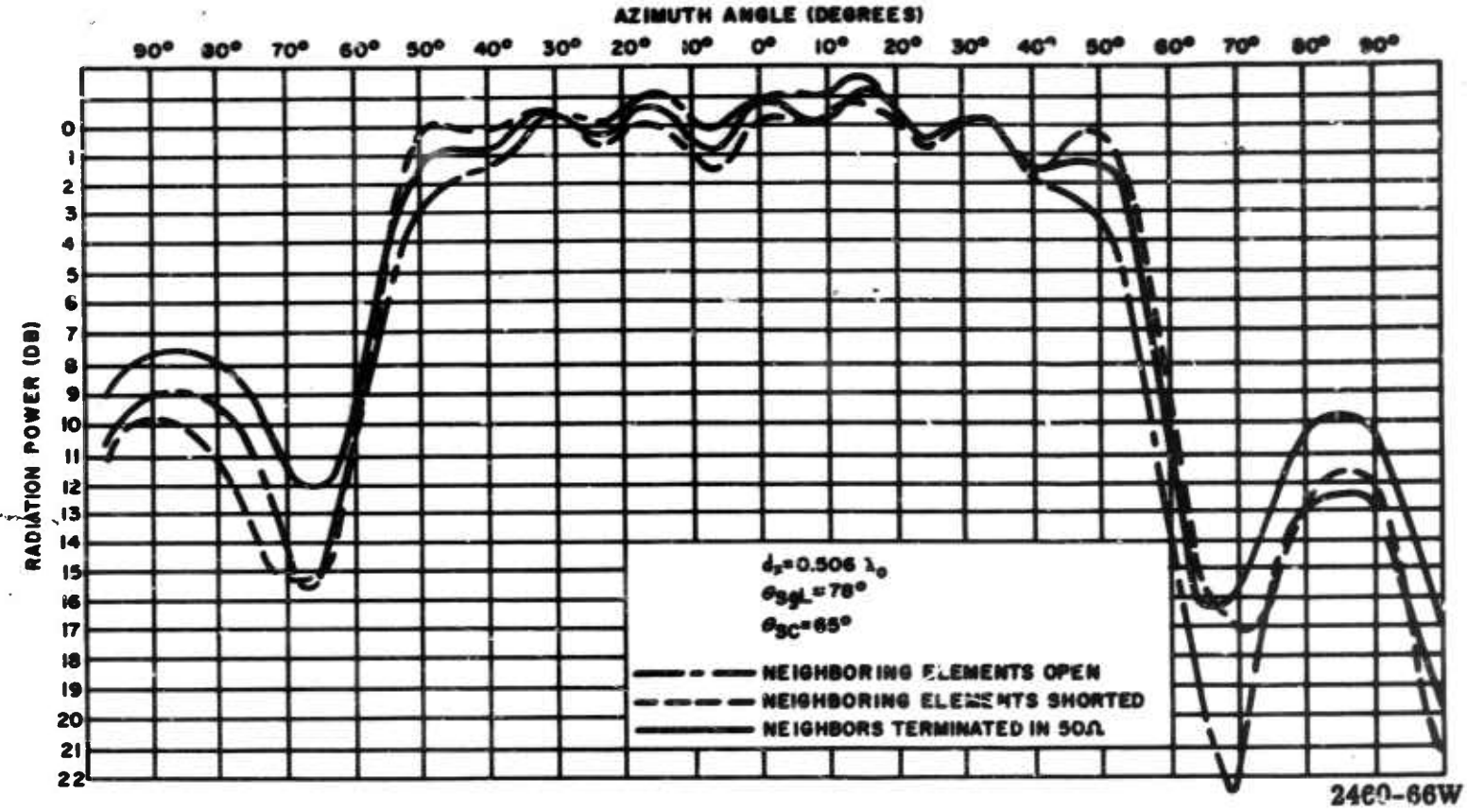

Figure 5-1. Element Radiation Pattern, $\vec{E}$ Component in Plane of Scan

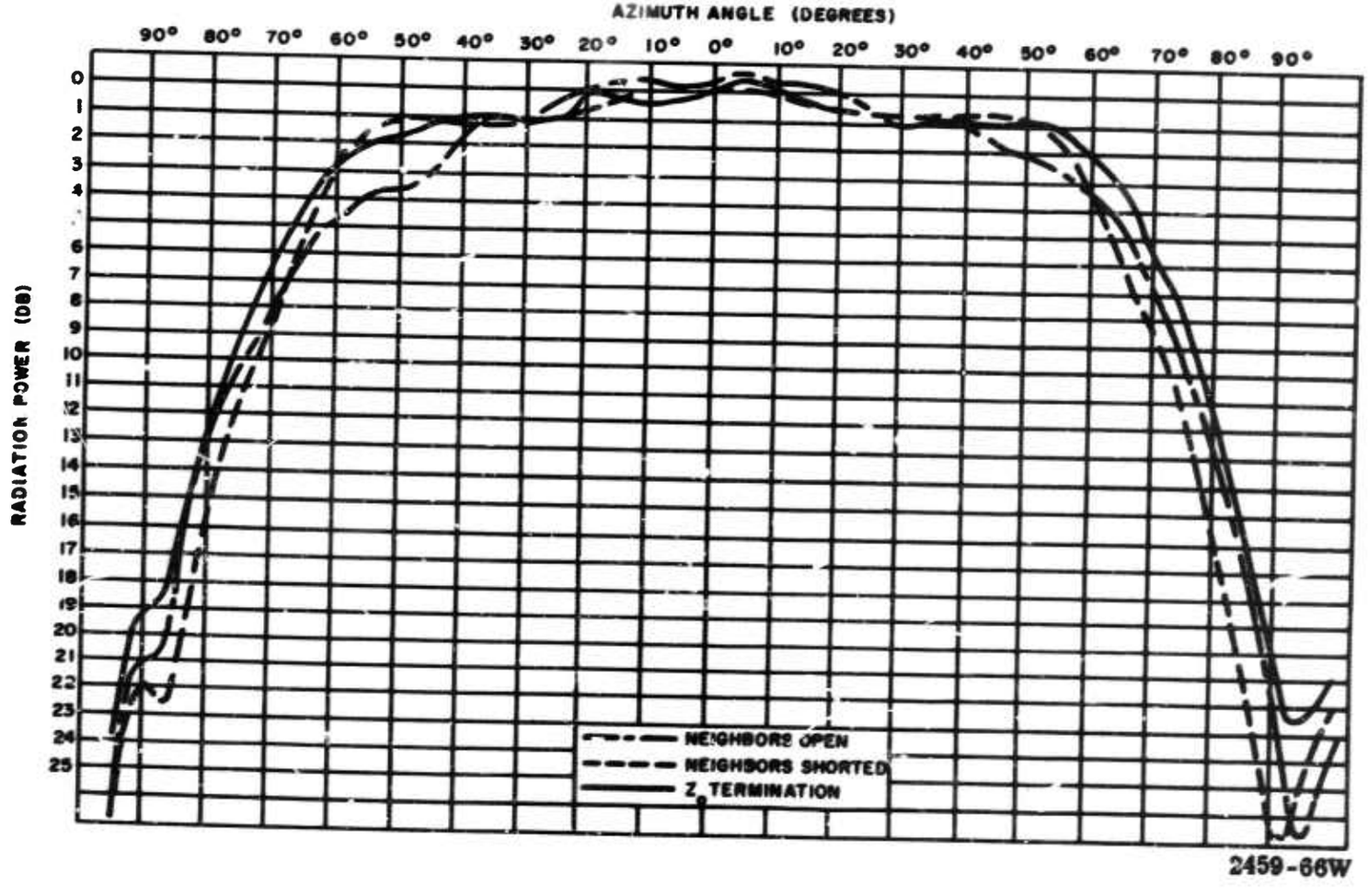

Figure 5-2. Element Radiation Pattern, $\vec{E}$ Component Perpendicular to Plane of Scan

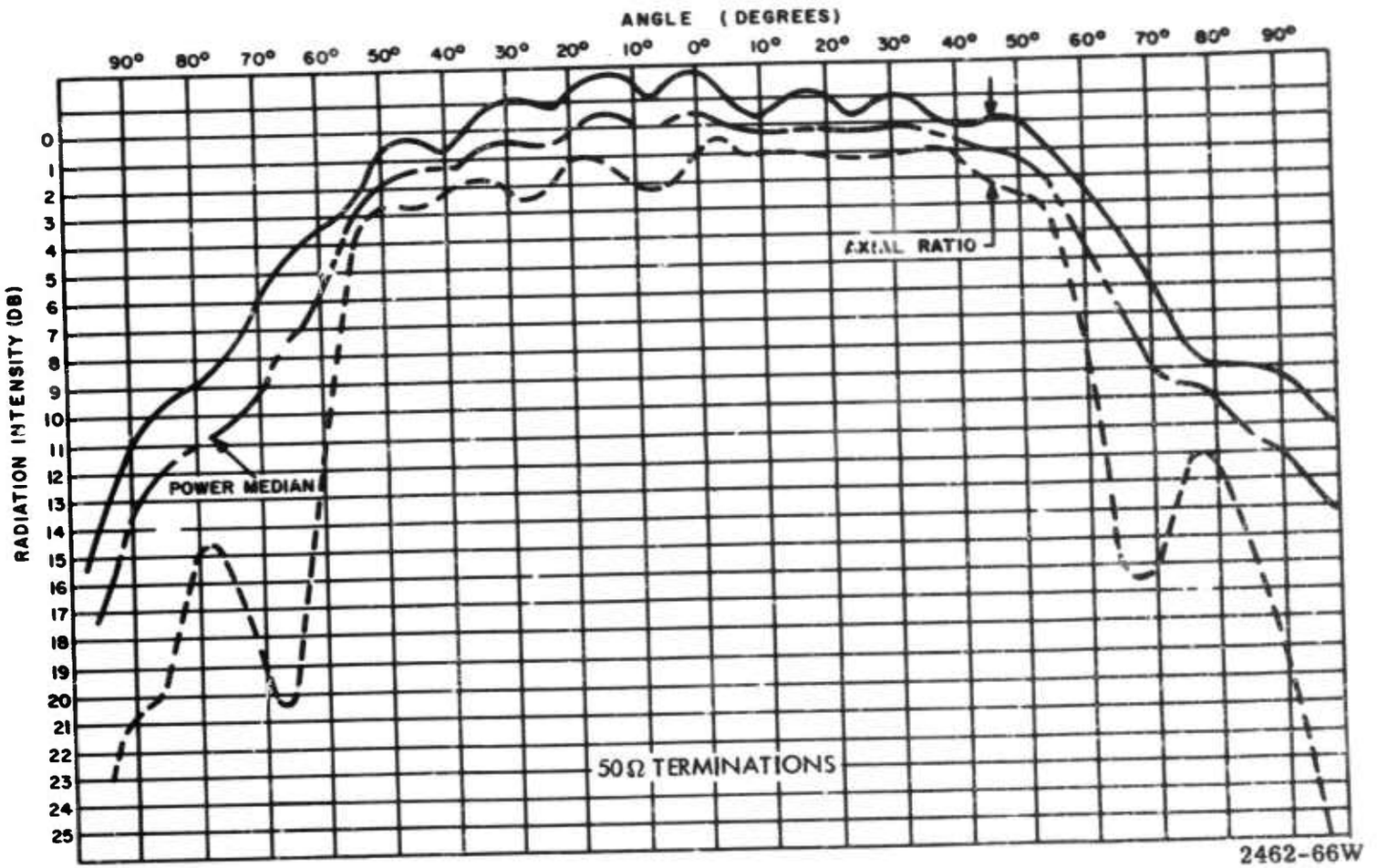

Figure 5-3. Element Radiation Pattern, Response to Rotating Linear Polarization

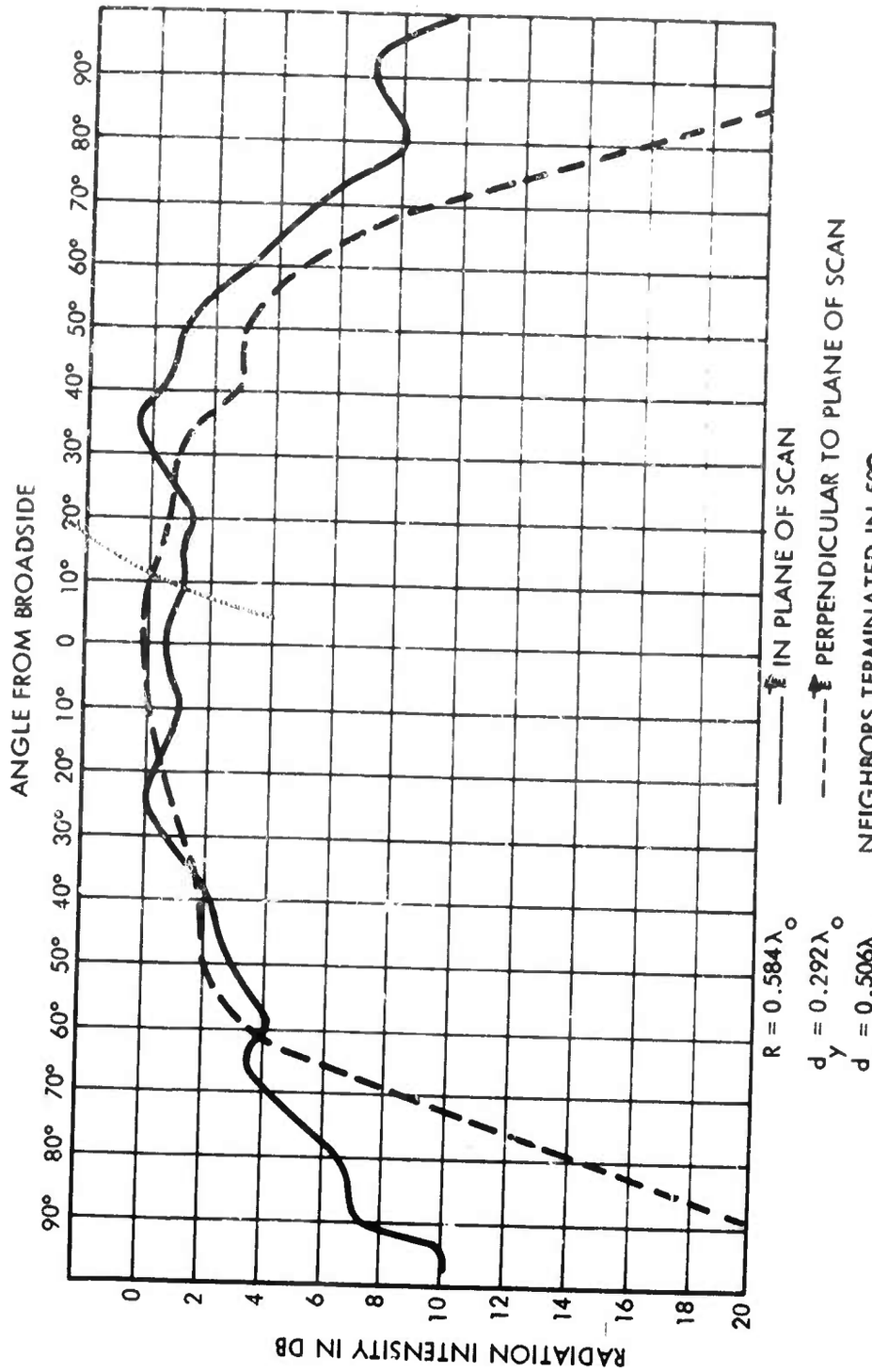

Figure 5-4. Element Radiation Pattern, Cardinal Plane

elements nulls appeared, as shown here. These nulls are a consequence of coupling to many neighboring elements and their re-radiation with a phase delay such as to nearly cancel the direct radiation from the central (active) element, at the critical scan angle. Equation (2-13) shows that a deep hole in the element pattern (of a single lobed array) implies a large impedance mismatch ($|\Gamma| \rightarrow 1$) in the active phased array steered to this same angle. Equation (1-13) gives the slow wave coupling velocity (v_s = 93%) corresponding to this critical scan angle ($\theta_{sc} = \pm 65°$) and electrical spacing ($d_x = 0.506\lambda_o$). The mutual coupling phase measurements (Figures 4-6 and 1-4) provide an independent check on the coupling velocity and also show $v_s \cong 0.93c_o$. Note that the radiation pattern (Figure 5-1) drops sharply at 55°, and has a radiation minimum at ±65°, whereas equation (1-14) shows that the grating lobe peak remains outside real space until the array is scanned to ±78°. Real array coverage is about 23° less than that predicted by the emergence of the grating lobe maximum into real space. Grating lobe suppression has been the criterion commonly used to determine interelement spacing and array scan coverage. That criterion is inadequate for arrays which support slow wave coupling and must be replaced by the formula for the critical scan angle of equation (1-13).

Figure 5-2 shows measured element radiation patterns with the electric field component perpendicular to the plane of scan (vertical polarization). The coverage is smooth and broad. No nulls occur within the forward half circle. The lack of nulls in Figure 5-2 can be explained in terms of the TM_o surface wave mode. This is the lowest order surface wave which can propagate over a metallic ground plane. This mode is believed to be the coupling mechanism causing the nulls in Figure 5-1. This ideal mode does not have an electric field component parallel to the ground plane (vertical polarization). Consequently, the parasitic elements cannot re-radiate this destructive component and the smooth "free-space" element pattern is preserved as seen in Figure 5-2.

Figure 5-3 is the radiation pattern of the same circularly polarized coaxial horn, using a facility with rotating linear polarization. The top and bottom curves are envelopes of the polarization ellipse; their vertical separation is the radiation ellipticity. The central curve is a plot of the net radiation power density vs. angle. It is also the median antenna response to a randomly oriented linear polarization. This antenna element had excellent internal circularity and good radiated circularity except near the critical scan region, where polarization became linear and perpendicular to the plane of scan. The depolarizing mechanism is a surface wave external to the array. Consequently, any

internal electronic techniques for polarization discrimination would be ineffective near the critical scan directions of a phased array.

The three previous figures showed element radiation patterns measured in the intercardinal plane of a hexagonal array of coaxial horns. Figure 5-4 shows the radiation pattern of the same element, in the same array, measured at the same frequency, but in a cardinal plane. In this plane, there are no radiation nulls for either linear polarization component. This is a consequence of the close effective antenna spacing in the cardinal planes ($d_y = d_x/\sqrt{3} = 0.557\, d_x$ as seen in Figure 4-1).

Figure 5-5 is an orthographic projection of the hemisphere in front of a planar phased array. It is a sketch showing the regions of large coupling accumulation and low radiation efficiency (shaded area), and the region of strong array coverage (white interior). The size and location of the region of poor radiation efficiency depend on the interelement spacing, and coupling velocity. The parameters $R_o = 0.585\lambda_o$, $d_x = 0.506\lambda_o$, and $v_s = 0.93c_o$ were used in Figure 5-5. These are the actual values from the previous array radiation measurements. Figures 5-1, 5-2 and 5-3 were antenna element radiation cuts in the intercardinal plane $\phi = \binom{0°}{180°}$. Figure 5-4 was a radiation cut in the cardinal plane $\phi = \binom{90°}{270°}$. These radiation patterns are array performance "cross-sections" in the principal planes of Figure 5-5.

5.2 MEASURED RADIATION NULLS

Next consider the influence of frequency "f" and electrical spacing between elements (R_o/λ_o) on measured array scan coverage. The physical character of the array (Figure 3-1) remained unchanged; only the microwave frequency was changed, in six steps across a 10% frequency band. After each frequency change, the element radiation pattern was measured (in the intercardinal plane). These element radiation patterns resembled the radiation plots given in the previous section (Figures 5-1, 5-2 and 5-3). The electric field radiation component in the plane of scan nearly vanished at a critical scan angle which depended on frequency and electrical spacing between elements in the array. In Figure 5-6 the angle of these radiation nulls θ_{sc} is plotted as a function of inter-element spacing (d_x/λ_o). The vertical dashed lines represent the six discrete frequencies (and electrical spacings) at which radiation patterns were measured. The points plotted as X locate the nulls in the measured antenna element pattern.

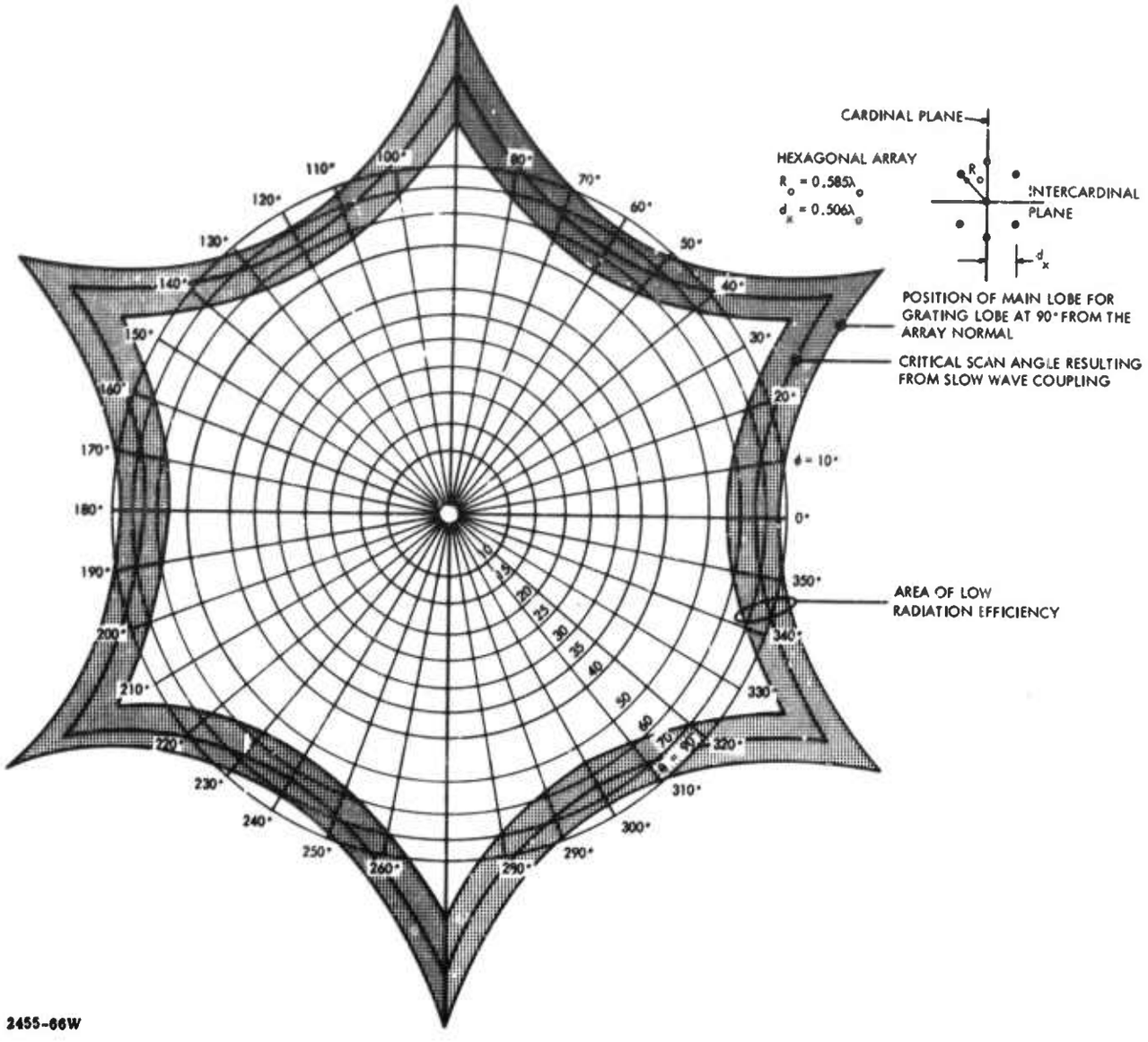

Figure 5-5. Critical Scan Areas

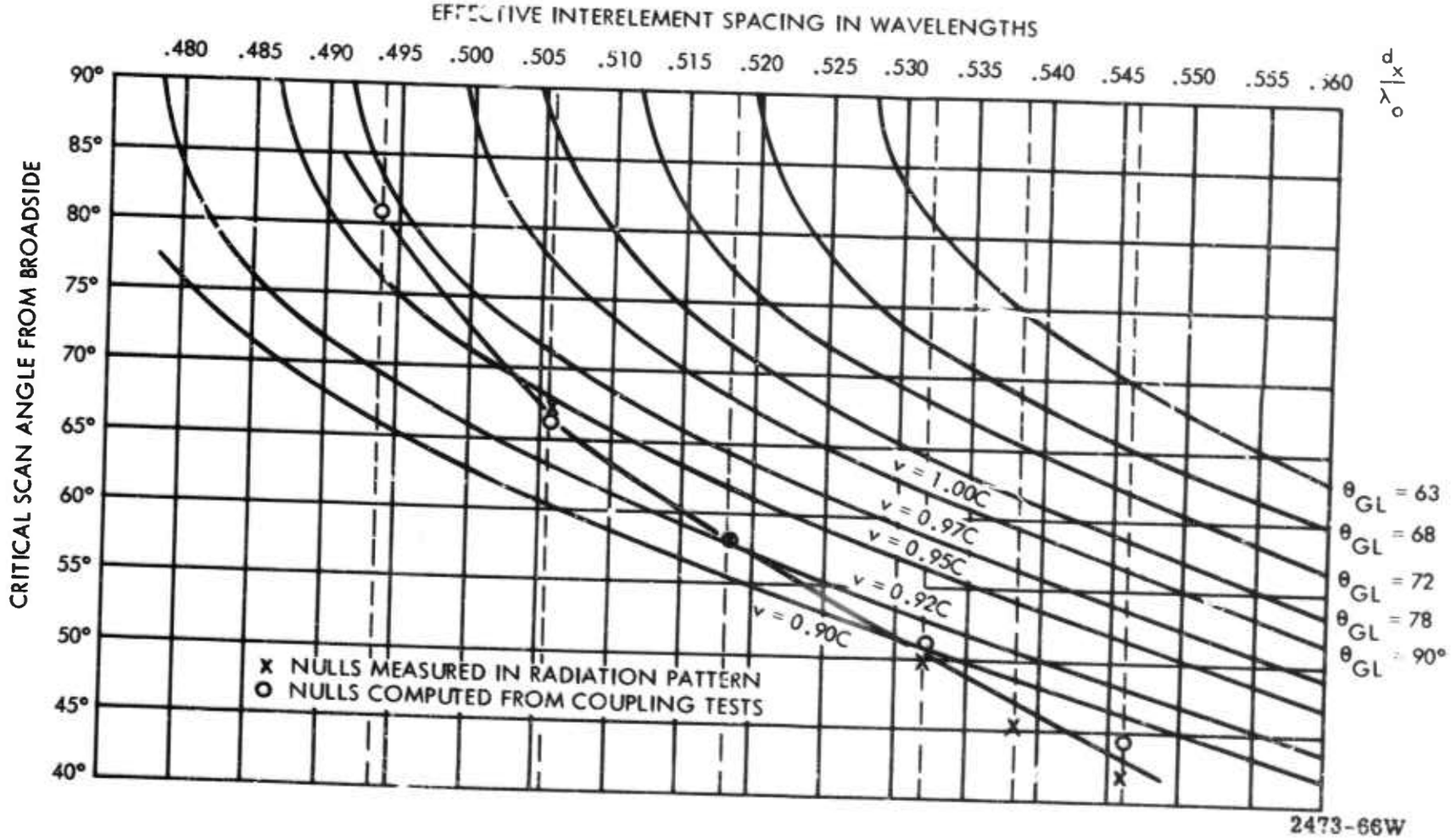

Figure 5-6. Critical Scan Angles, Circularly Polarized Elements with Radomes

Equation (1-13) gave a functional relationship between the critical scan angle θ_{sc}, the array electrical spacing (d_x/λ_o), and the coupling velocity v_s. This relationship yields the lower five curves in Figure 5-6. The upper curves show the location of the real grating lobe vs. scan angle and array spacing. The defining equations are

$$\left|\sin \theta_s\right| = \left(\frac{\lambda_o}{d_x}\right) - \left|\sin \theta_{GL}\right|$$

and

$$\left|\sin \theta_{sc}\right| = \left(\frac{\lambda_o}{d_x}\right) - \left(\frac{c_o}{v_s}\right).$$

Hence, the similarity between the contours for constant coupling velocity and for constant grating lobe angle.

Array mutual coupling coefficients were measured at several frequencies (the same ones used in the above radiation pattern measurements). At each frequency the coupling velocity and critical scan angle were computed using equations (1-10) and (1-13). These critical scan angles (based on mutual coupling coefficient measurements) are plotted as "0" in Figure 5-6. We can compare the minima in the measured radiation patterns "X" to the critical scan angles obtained from coupling measurements "0". In nearly every case, the critical scan angle based on coupling data matched the first minimum in the element radiation pattern. The scan coverage of this phased array is limited by slow wave coupling accumulation.

Next, the array of coaxial horns was converted from circular to linear polarization by removing the quarter-wave-plate from each antenna element (Figure 1-5). The plane of linear polarization was made to coincide with the intercardinal plane of the hexagonal array, and the element radiation patterns were measured in this same (horizontal) plane. These are the conditions conducive to launching and propagating a surface wave on the array face.

The linearly polarized array radiated practically no vertical (cross polarized) energy at any angle in the intercardinal plane. (This is to be expected of a well constructed, horizontally polarized antenna element in a homogeneous symmetric array). The linearly polarized array radiates (or receives) horizontally polarized signals. Its element radiation pattern closely resembles Figure 5-1 which showed the horizontal component of radiation from the circularly polarized array.

Linearly polarized element radiation patterns were measured at eight frequencies over a 17% band. Deep nulls were found only at the four highest frequencies (four largest values of d_x/λ_o). These measured nulls appear as "X" on Figure 5-7. No deep nulls were found at the four lowest frequencies (vertical dashed lines). The null positions were similar for linearly and circularly polarized arrays. The null depths varied considerably with frequency and polarization. Usually, the circularly polarized array had the sharper and deeper nulls. This could be a consequence of the looser, slowly decaying terminal coupling and consequent larger coupling area in the circularly polarized array.

In the previous arrays, each antenna element was covered with a hemispheric radome (Figure 1-5). These radomes had a dielectric constant e = 6.0, a thickness $T/\lambda_o = 0.018$, and a radius $r/\lambda_o = 0.3$. All radomes were removed to determine their effect on array performance. A large element mismatch resulted (VSWR = 3). The elements were rematched by identically reducing the diameter and length of the center conductor in each antenna of the array. A passive (S_{oo}) match of better than 2.0 VSWR was achieved over the 17% frequency band. Figure 5-8 is a photo of this array.

Element radiation patterns were measured in the intercardinal plane at eight microwave frequencies, first with all radomes in place and next with all radomes removed and the elements rematched. Figure 5-7 showed the critical scan angles measured in the array with radomes in place; Figure 5-9 shows the critical scan angles in the element radiation patterns measured at the same frequencies after removal of all radomes and rematching of the elements. At the four lowest frequencies no radiation nulls appeared either with or without radomes. At the fifth frequency (for which $d_x/\lambda_o = 0.519$), symmetric nulls appeared at ±64° from broadside with radomes in place. At this frequency the nulls dissappeared upon removal of the radomes. At the three highest frequencies deep radiation holes were observed both with and without radomes. Removal of these radomes caused the radiation nulls to move to wider angles, thus increasing the full angle of strong array coverage by an amount from 12° to 50° depending on the frequency. The angle of these radiation minima can be used to compute the coupling velocity in each array at the three highest test frequencies. Radome removal caused an increase of nearly 7% in this coupling velocity. The velocity increase was nearly the same for the three test frequencies. Furthermore, this velocity change was in good agreement with the 7.5% change in surface wave velocity estimated theoretically in Section I.

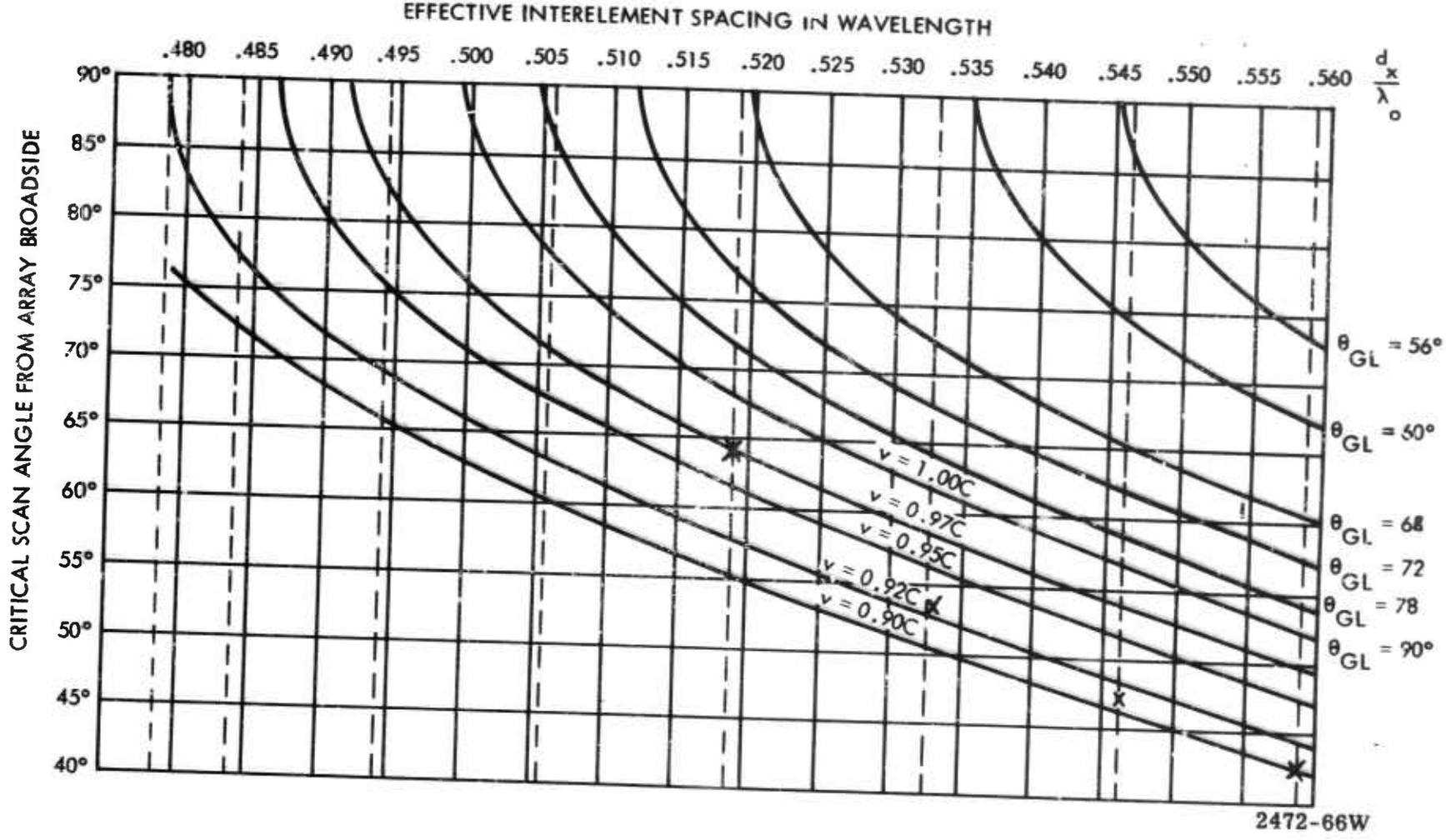

Figure 5-7. Critical Scan Angles, Linearly Polarized Elements with Radomes

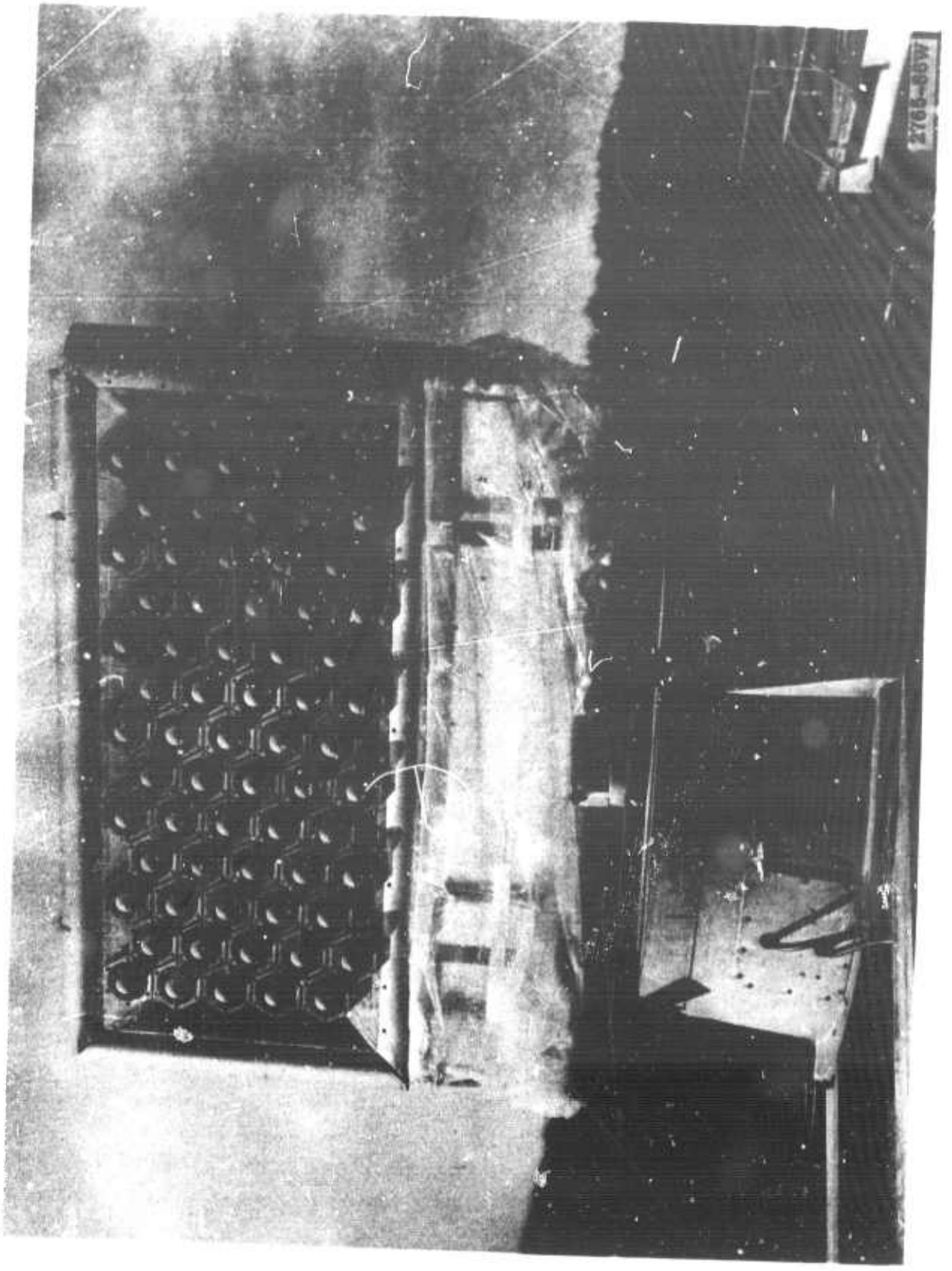

Figure 5-8. Antenna Array without Radomes

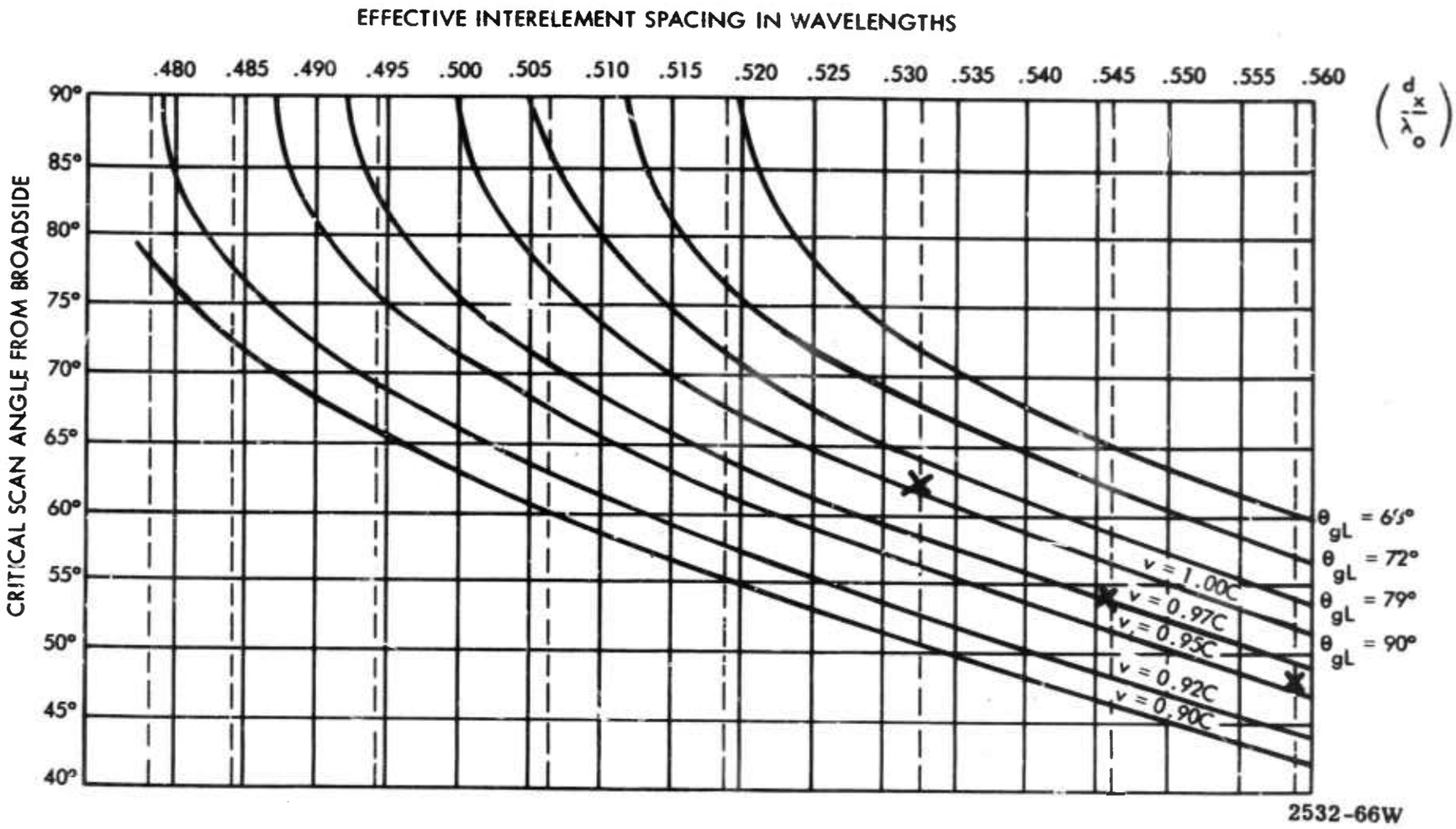

Figure 5-9. Critical Scan Angles, Linearly Polarized Elements without Radomes

In each of the previous arrays the antenna elements were mounted on a metallic ground plane which provided hexagonal grooves around each antenna element. These grooves were a consequence of the antenna physical design and assembly technique. The grooves were nearly uniform, with a depth $0.1\lambda_o$ and a width $0.017\lambda_o$. Their similarity to microwave chokes suggested that the grooves might influence the coupling velocity on the array and thus its critical scan angle. To check this, all the choke grooves were covered with metal foil, and radiation patterns were measured at several microwave frequencies before and after foil covering. The radiation holes did not significantly change in location or depth, suggesting that these chokes had little effect on coupling accumulation and array scan coverage. (Experiments at Lincoln Laboratory and at Raytheon have shown a strong influence of choke depth on the position of the radiation nulls measured in arrays of small rectangular horns. Presumably the grooves used in our tests were too narrow and too shallow to seriously impede the ground plane currents, and thus did not influence the coupling velocity or radiation nulls.)

Figures 5-1 and 5-2 showed that element radiation patterns and array scan coverage can depend on the array terminal impedance (generator impedance in a transmitting phased array). The antenna elements periodically couple and load any wave traveling across the array face. Changes in the impedance connected to the antenna terminals could affect this periodic loading and influence the array coupling coefficients and the critical scan angles. Four different types of reactive terminations were secured, plus 50Ω coaxial resistance. The central antenna element was connected to a detector and recorder. All neighboring elements were connected uniformly to the same type loads. The element radiation patterns were measured for these five distinct loads and at three different microwave frequencies. Three of the reactive terminations gave element radiation patterns very similar to those obtained with matched (50Ω) loads. The fourth reactive termination yielded broad element radiation patterns with considerable end-fire radiation. This broad coverage could be very desirable in some radar applications. It was observed at all three test frequencies using uniform terminations of two different physical designs and having similar electrical lengths. The broad element pattern, resulting from this specific set of reactive terminations, seems to be a true and accurate performance of the central element in this array. However, strong end-fire radiation is not theoretically possible in a very large array because of beam broadening with array scan toward end-fire (see equation 2-11). In going to larger arrays, the normalized element radiation pattern near end-fire must decrease to conserve available power. It is not known to what extent the generator impedance could be used to effectively control scan coverage in large, real, phased array systems.

SECTION VI

ARRAY COMPARISON

Several different antenna-array types have been critically analyzed or measured at Sylvania and at other organizations. Published data were examined and, where warranted, meetings were arranged with the principal investigators. These meetings are listed under VISITS and VISITORS.

Reported performance of these arrays will be reviewed here. The arrays critically evaluated include

1) Coaxial horns (Figure 1-5) measured under this and a related contract (Appendix C).

2) Flush coaxial horns developed by Sylvania Electronic Systems as a proprietary item.

3) Rectangular open end waveguide measured and analyzed at Bell Telephone Laboratories.[11, 12, 13, 14]

4) Infinitely long, narrow slits in a metal ground plane, analyzed in Appendix A.

5) Dipoles parallel to a conducting ground plane analyzed in Appendix B and References 15, 16, and 17.

Performance of these arrays can be classified according to whether or not they have a scanning blindness resulting from a large coupling accumulation and the emergence of a real grating lobe.

Analysis of arrays of dipoles parallel to a flat conducting sheet shows no radiation holes attributable to either slow wave coupling accumulation or end-fire grating lobe radiation. The element radiation patterns decreases smoothly and the magnitude of the mismatch grows smoothly with increasing scan angle, corresponding to the approach and entrance of a grating lobe into real space. This comparatively smooth scan performance of the dipole array is related to the radiation pattern of an isolated dipole over an infinite metal sheet. The dipole and its effective image do not radiate along the ground plane. A large dipole array does not radiate strongly near the ground plane and couplings do not accumulate to a maximum corresponding to a slow wave across the array face. These are the two potential causes of radiation minima in phased arrays. They are suppressed in an array of dipoles parallel to a conducting ground plane.

Measurement of Element radiation patterns in an array of 91 flush coaxial horns also revealed no nulls either at or preceding the emergence of a real grating lobe. More extensive data on this element is needed. All of the remaining arrays evidence holes in their scan coverage (similar to Figure 5-1) at or preceeding the emergence of a real grating lobe. Array size has some influence on the scan angle at which the radiation minima occur. Arrays of several dozen elements have radiation minima at scan angles a few degrees nearer broadside than those found in very large arrays of similar design. Antenna-array design details also influence the coupling velocity and thus the angle of radiation minima. Certain radome and choke geometries retard the coupling wave and reduce array scan coverage.

REFERENCES

1. J. Allen, "On Surface-Wave Coupling Between Elements of Large Arrays," IEEE, T.A.P., July 1965, pp. 638-9.

2. Barlow and Cullen, "Surface Waves," Proc of IEEE, Volume 100, part 3, Nov. 1953, pp. 329-347.

3. F. Zucker, "Surface and Leaky Wave Antennas," Chapter 16 of Antenna Engineering Handbook, by H. Jasik, McGraw Hill, 1961.

4. C. Walter, "Traveling Wave Antennas," McGraw Hill, 1965, pp. 235-280.

5. L. Lechtreck, "Green's Function in Space Tapered Arrays," IEEE, T.A.P., May 1964, pp. 366-367.

6. L. Parad, "Some Mutual Impedance Effects in Phased Arrays," The Microwave Journal, June 1962, pp. 87-89.

7. J. Allen, "Mutual Coupling - Why Worry About It," 1965 International Antenna and Propagation Symposium Program and Digest, pp. 133-137.

8. L. Lechtreck, "Cumulative Coupling in Antenna Arrays," 1965 International Antenna and Propagation Symposium Program and Digest, pp. 144-149.

9. N. Hamlin, "Double-Probe Phase Meter is Simple and Accurate," Microwaves, Jan. 1966, pp. 42-45.

10. L. Parad and R. Kreutel, "Mutual Effects Between Circularly Polarized Elements," 12th Annual Symposium, USAF Antenna R&D, University of Illinois, Oct. 1962.

11. Amitay, Cook, Pecina, and Wu, "On Mutual Coupling and Matching Conditions in Large Planar Phased Arrays," 1964 PTGAP International Symposium Program and Digest, p. 154.

12. C. P. Wu and V. Galindo, "Properties of a Phased Array of Rectangular Waveguides with Thin Walls," IEEE, T.A.P., March 1966, pp. 163-173.

13. V. Galindo and C. P. Wu, "Asymptotic Behavior of the Coupling Coefficients for an Infinite Array of Thin-Walled Rectangular Waveguides," IEEE, T.A.P., March 1966, pp. 248-9.

14. V. Galindo and C. Wu, "Numerical Solutions for an Infinite Phased Array of Rectangular Waveguides with Thick Walls," IEEE, T.A.P., March 1966, pp. 149-158.

15. L. Stark, "Radiation Impedance of a Dipole in an Infinite Array," Radio Science, March 1966, Vol. 1, pp. 361-367.

16. P. Carter, "Mutual Impedance Effects in Large Beam Scanning Arrays," IRE, PTGAP, May 1960, pp. 276-285.

17. J. Allen et. al., "Phased Array Radar Studies," Lincoln Laboratory Tech., Report No. 381, March 31, 1965.

18. J. Zenneck, "Uber die Fortpflanzumg ebener elektromagnetischer Wellen längs einer ebener Leiterfläche und ihre Beziehung zur drahtlosen Telegraphie," Annalen der Physik, 1907, 23, p 846.

19. W. VonAulock, "Properties of Phased Arrays," Proc IRE, October 1960, pp 1715-27.

20. P. Hannan, "The Element-Gain Paradox For a Phased-Array Antenna," IEEE, T.A.P., July 1964, pp 423-433.

21. R. Elliott, "Beamwidth and Directivity of Large Scanning Arrays," Microwave Journal, Jan. 1964, pp. 74-82.

APPENDIX A

THE INPUT ADMITTANCE TO A SLOTTED ARRAY WITH OR WITHOUT A DIELECTRIC SHEET

L. I. Parad

The performance of a phased array is dependent upon the active driving point admittance of the array element as a function of scan. In fact, the scan limits of the array are set by the element mismatch rather than the grating lobe formation (in some cases, the large element mismatch is coincident with the appearance of the grating lobe). A number of papers have been written on the subject of the element match. One method [(1), (2)], gives a physical insight to the problem but gives qualitative rather than quantitative results. Another approach[(3)] which yields quantitative results, does not give physical insight to the problem and is very complicated. The interpretation given in reference (4) of Stark's[(5)] derivation is useful because it gives one an understanding as to why the input admittance is expressed as a series. However, the interpretation is not valid when a dielectric sheet covers the array. In this paper, a transmission line approach will be used to solve the problem. Because of the simplicity of this approach, it can be applied to more complicated problems, such as an array covered by several layers of dielectric sheets. In order to emphasize the approach rather than the solution to a particular problem, a two dimensional problem will be solved.

The geometry of the problem is shown in Figure A-1. The array, which consists of a large number of slots, lies in the XY plane. Each slot is infinite in the "Y" direction and has a uniform electric field "E", independent of "Y" in the "X" direction. The entire array is covered by a dielectric sheet of thickness "t" and relative permitivity "ϵ_r". The array of slots is fed with a progressive phase shift $v_o d$ so that the main beam is steered in the direction

$$\sin \theta_o = \frac{\lambda v_o}{2\pi} = \frac{v_o}{k} \tag{1}$$

where

$$v_o = \frac{2\pi}{\lambda} \sin \theta_o$$

and v_o is the propagation constant in the "X" direction

k is the free space propagation constant

θ_o is the direction of the peak of the main beam.

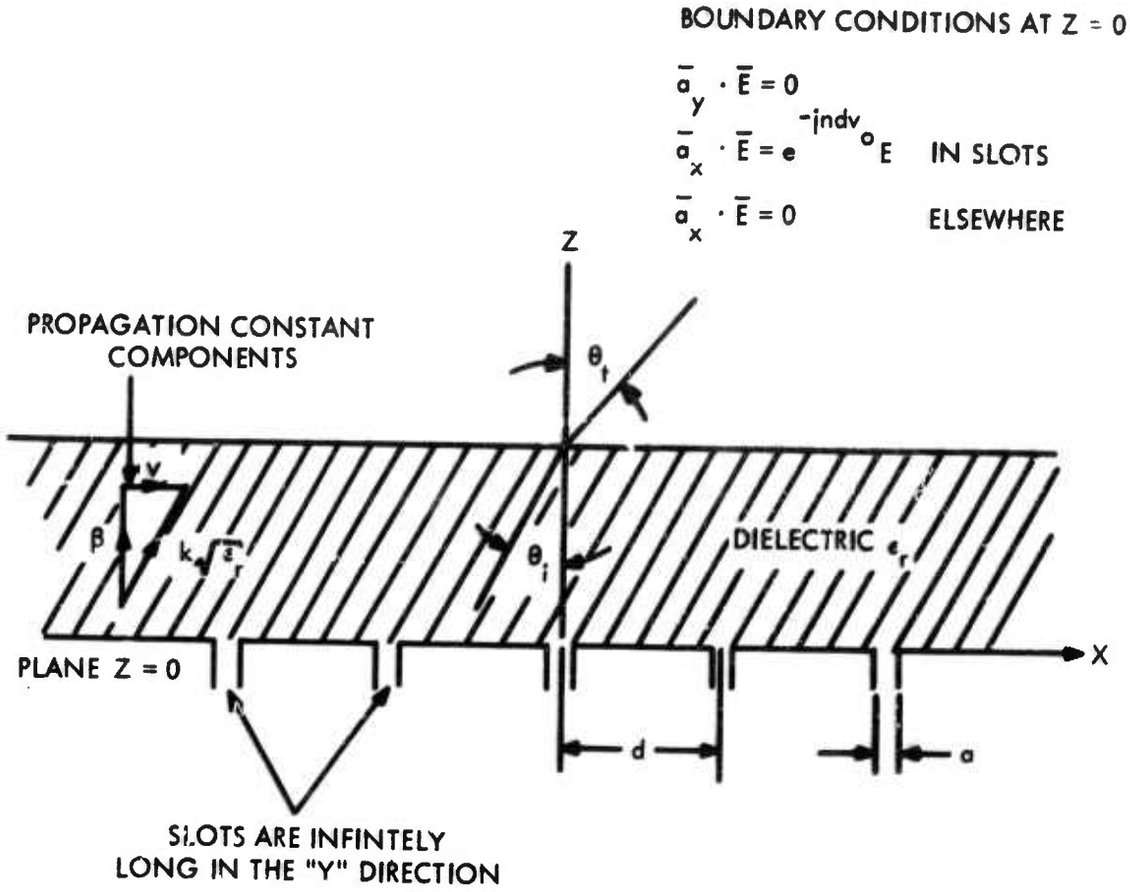

Figure A-1. Planar Slotted Array Covered by a Dielectric Sheet

The input admittance of one slot as a function of steering angle will be solved by the following method.

(a) Express the field at Z = 0 as the sum of an infinite number of plane waves.

(b) Determine the input admittance at Z = 0 for a plane wave.

(c) Compute the total input power at Z = 0 for an aperture having a length "ℓ" in the "Y" direction and a width "d" in the "X" direction.

(d) Express the input admittance in terms of the input power and voltage.

To express the aperture field as a sum of plane waves, we take the Fourier transform of the aperture distribution:

$$\mathcal{E}_x(v) = \int_{-\infty}^{\infty} E_x(x,0)e^{jvx}dx = \frac{aE \sin av/2}{av/2} \cdot \frac{\sin (2N+1)(v - v_o)\, d/2}{\sin (v - v_o)d/2} \qquad (2)$$

where $N \to \infty$ and "v" is the propagation constant in the "X" direction. Taking the inverse transform to obtain $E_x(x, o)$ results in

$$E_x(x,0) = \frac{1}{2\pi} \int_{-\infty}^{\infty} \frac{aE \sin av/2}{av/2} \cdot \frac{\sin (2N+1)(v - v_o)d/2}{\sin (v - v_o)d/2} e^{-jvx}dv \qquad (3)$$

In evaluating equation (3), it is important to observe that the integrand is zero except in the vicinity of $v = v_o + 2n\pi/d$ where $\sin \frac{d}{2}(v - v_o) \approx \frac{d}{2}(v - v_o)$. Thus equation (3) may be rewritten as

$$E_x(x,0) = \frac{aE}{2\pi} \sum_{n=-\infty}^{\infty} \left\{ \frac{\sin \frac{a}{2}(v_o + 2n\pi/d)}{\frac{a}{2}(v_o + 2n\pi/d)} e^{-j(v_o + 2n\pi/d)x} \right.$$

$$\left. \int_{v-(v_o + 2n\pi/d-)}^{v-(v_o + 2n\pi/d+)} \frac{\sin (2N+1)(v - v_o)d/2}{(v - v_o)d/2}\, dv \right\} \qquad (4)$$

$$E_x(x,0) = \frac{aE}{d} \sum_{n=-\infty}^{\infty} \frac{\sin \frac{a}{2}(v_o + 2n\pi/d)}{\frac{a}{2}(v_o + 2n\pi/d)} e^{-j(v_o + 2n\pi/d)x} \qquad (5)$$

Since none of the derivation thus far is dependent upon the dielectric slab being present, let us momentarily assume the dielectric slab is not there. Then the input admittance to a plane wave is

$$Y_i = \frac{H_y}{E_x} = \frac{1}{\eta \cos\theta}$$

$$\cos\theta = \sqrt{1 - \frac{v^2}{k^2}} \qquad (6)$$

where $\eta = \sqrt{\mu/\epsilon} = 377$ for free space and θ is the angle the incident wave makes with the YZ plane. The input power to the structure for a length "ℓ" in the "Y" direction and width "d" in the "X" direction is

$$P = \frac{1}{2} \int_0^{\ell} \int_{d/2}^{d/2} E_x H_y^* \, dx \, dy \qquad (7)$$

Equations (5) and (6) can be inserted into equation (7)

$$P = \frac{a^2 \ell \, |E|^2}{2d^2} \int_{-d/2}^{d/2} \left[\sum_{n=-\infty}^{\infty} \frac{\sin \frac{a}{2}(v_o + 2n\pi/d)}{\frac{a}{2}(v_o + 2n\pi/d)} e^{-j(v_o + 2n\pi/d)x} \right]$$

$$\left[\sum_{m=-\infty}^{\infty} Y_{im}^* \frac{\sin \frac{a}{2}(v_o + 2m\pi/d)}{\frac{a}{2}(v_o + 2m\pi/d)} e^{-j(v_o + 2m\pi/d)x} \right] dx \qquad (8)$$

Note that for $m \neq n$, the integral is zero. Hence, the power supplied by a length "ℓ" of one slot is

$$P = \frac{a^2 \ell \, |E|^2}{2d} \sum_{n=-\infty}^{\infty} Y_{in}^* \left[\frac{\sin \frac{a}{2}(v_o + 2n\pi/d)}{\frac{a}{2}(v_o + 2n\pi/d)} \right]^2 \qquad (9)$$

where Y_{in}^* is determined from equation (6) using

$$Y_{in} = \frac{1}{\eta \sqrt{1 - (v_o + 2n\pi/d)^2/k^2}} = \text{input wave admittance at } z = 0 \text{ (without dielectric)} \qquad (10)$$

The power into the slot in terms of the slot admittance is

$$P = \frac{1}{2} VI^* = \frac{1}{2} (Ea)(Ea)^* Y^* \tag{11}$$

Combining equations (9) and (11), the slot input admittance is

$$Y = \frac{2P^* \ell}{a^2 |E|^2} = \frac{\ell}{d} \sum_{n=-\infty}^{\infty} Y_{in} \left[\frac{\sin \frac{a}{2} (v_o + 2n\pi/d)}{\frac{a}{2} (v_o + 2n\pi/d)} \right]^2 \tag{12}$$

where Y_{in} is given by equation (10) and is the ratio of H_y/E_x in the plane Z = 0 for the nth plane wave as given by equation (5).

Consider the situation where the array of slots is covered by a dielectric layer. In this case, the input admittance to the slot is still given by equation (12) except that Y_{in} must be computed from the formula[6]

$$Y_{in} = Y_{on} \frac{Y_{an} + j\, Y_{on} \tan \beta_n t}{Y_{on} + j\, Y_{an} \tan \beta_n t} = \left. \frac{H_y}{E_x} \right|_{Z=0} = \text{input admittance, seen thru dielectric} \tag{13}$$

where

$$Y_{on} = \frac{H_{yi}}{E_{xi}} = \sqrt{\frac{\epsilon_r \epsilon_o}{\mu}} \frac{1}{\cos \theta_{in}} = \text{characteristic wave admittance, in dielectric, referred to Z direction.}$$

$$Y_{an} = \frac{H_{yt}}{E_{xt}} = \sqrt{\frac{\epsilon_o}{\mu}} \frac{1}{\cos \theta_{tn}} = \text{characteristic wave admittance, in air, referred to Z direction}$$

$$\beta_n = k \sqrt{\epsilon_r} \cos \theta_{in} = \sqrt{\epsilon_r k^2 - \left(v_o + \frac{2n\pi}{d}\right)^2} = \text{wave number, in Z direction, in dielectric.}$$

$$\cos \theta_{in} = \sqrt{1 - \frac{1}{\epsilon_r k^2} \left(v_o + \frac{2n\pi}{d}\right)^2}$$

$$\cos \theta_{tn} = \sqrt{1 - \frac{1}{k^2} \left(v_o + \frac{2n\pi}{d}\right)^2}$$

θ_{in} is the angle which the incident wave makes with the YZ plane

θ_{tn} is the angle which the transmitted wave makes with the YZ plane

H_{yi} and E_{xi} are the incident wave fields in the dielectric

H_{yt} and E_{xt} are the transmitted wave fields in space

Some consequences of equation (12) will now be discussed. The input admittance has a pole when Y_{in} has a pole. From equation (13), these poles can occur only when θ_t is an imaginary angle (no radiation). It has been shown [7] that these poles correspond to the excitation of surface wave modes. An estimate of the propagation constant "v" which gives rise to the admittance pole can easily be obtained from equation (7) for a thin dielectric layer by assuming that

$$\tan \beta t = \beta t \tag{14}$$

the condition for the admittance pole is obtained from equation (13) as

$$\sqrt{1 - \frac{v^2}{k^2}} = - jkt\left(1 - \frac{v^2}{\epsilon_r k^2}\right) \tag{15}$$

$$\frac{v^2}{k^2} = \epsilon_r + \frac{\epsilon_r^2}{2k^2t^2}\left[1 - \sqrt{1 + 4k^2t^2\,\frac{\epsilon_r - 1}{\epsilon_r}}\right] \approx 1 + k^2t^2\left(\frac{\epsilon_r - 1}{\epsilon_r}\right)^2 \tag{16}$$

Note that for $kt < 0.1$, the propagation constant which caused the admittance pole is essentially equal to the free space propagation constant independent of the dielectric constant. The thickness of the dielectric, not the dielectric constant, is the important factor in determining the surface wave velocity.

A few comments on the validity of this approach are appropriate. There were two assumptions made to derive equation (9). One assumption was that the array was infinite and the other that the electric field across the slot is uniform. The infinite array assumption is reasonable for many of the large phased arrays being built or planned. The assumption of a uniform field across the slots, although accurate only for narrow slots, does not affect the position of the input admittance pole as can be seen from equation (9). The aperture field distribution can affect the admittance pole by eliminating it, which occurs when the transform of the aperture field has a zero at the angle for which Y_{in} has a pole.

In summary the input admittance as a function of scan angle has been determined for a planar array scanned in the "E" plane. It is shown that an admittance pole occurs at a scan angle which corresponds to surface wave propagation along the structure. Since the surface wave propagation constant is greater than that of free space, the admittance pole occurs at scan angles prior to the emergence of the grating lobe. Thus, the scan limits of a phased array are specified by the admittance poles which occur in the same planes of scan as the grating lobes, but at smaller scan angles. The total input admittance is obtained from the summation of an infinite number of terms. However, for slots about a quarter wavelength wide, equation (12) shows that the summation converges rapidly and several terms are adequate for most engineering applications.

References

1. Allen, J. L., "On Surface-Wave Coupling Between Elements of Large Arrays", IEEE Trans. on Antennas and Propagation, Vol. AP-13, July 1965, pp. 638-639.

2. Lechtreck, L.W., "Cumulative Coupling in Antenna Arrays", 1965 International Symposium of the IEEE Group on Antennas and Propagation, Aug. 30-Sept. 1, pp. 144-147.

3. Galindo, V. etal, "Numerical Solutions for an Infinite Phased Array of Rectangular Waveguides with Thick Walls:, 1965 International Symposium of the IEEE Group on Antennas and Propagation, Aug. 30-Sept. 1, 138-143.

4. Parad, L.I., "The Real and Reactive Power of a Planar Array" IEEE Trans. on Antennas and Propagation, Vol. AP-13, Nov. 1965

5. Stark, L., "Radiation Impedance of a Dipole in an Infinite Array". Formal Technical Document, Hughes Aircraft Co., Fullerton, Calif. (May 1, 1960).

6. Ramo, S. and Whinner, J.R., "Fields and Waves in Modern Radio, John Wiley & Sons, Inc., New York, Second Edition 1953, pp. 296-298.

7. Walter, C.H. "Traveling Wave Antennas," McGrawHill Book Co., Inc., New York, 1965, pp. 253-258.

APPENDIX B

DIPOLES IN PHASED ARRAYS

L. Parad

B.1 INTRODUCTION

Since the dipole is the best known antenna element, a great deal of work has been done to evaluate its performance in a phased array. As is usual, new work in the field has supplanted the older work in most instances. For this reason, only the work of Stark[1] and that of the Lincoln Laboratory group[2][3] need be considered. Using the recent work in the field, this section will evaluate the electrical performance of a dipole above a ground plane. The array of dipoles in free space will not be considered since it is the equivalent of a slotted array.

The most important electrical characteristics of a phased array antenna element are its pattern in the array and its active driving point impedance. These characteristics will be studied for both infinite and finite sized arrays.

B.2 INFINITE DIPOLE ARRAY

B.2.1 Input Impedance as a Function of Scan Angle

The driving point impedance of one dipole in an infinite dipole array has been investigated by Stark.[1] The array geometry without a ground plane is shown in Figure B-1. The following assumptions are made in the analysis:

1) The dipoles are thin metal strips "L" long and "δ" wide.

2) The current distribution on the individual dipole is sinusoidal (with peak current at the dipole center).

3) The dipoles are driven with equal amplitudes and phased to produce a planar wave front.

The method of solution is to express the current distribution in the XY plane as a double Fourier Series of plane waves. For example, if the current distribution were independent of Y and consisted of an infinite number of pulses along the X axis, the series of pulses may be represented by a single Fourier Series, with each component having a specific amplitude and wavelength along the X axis. Each Fourier Series component is a plane wave having no Y variation and whose wavelength in the X direction determines the

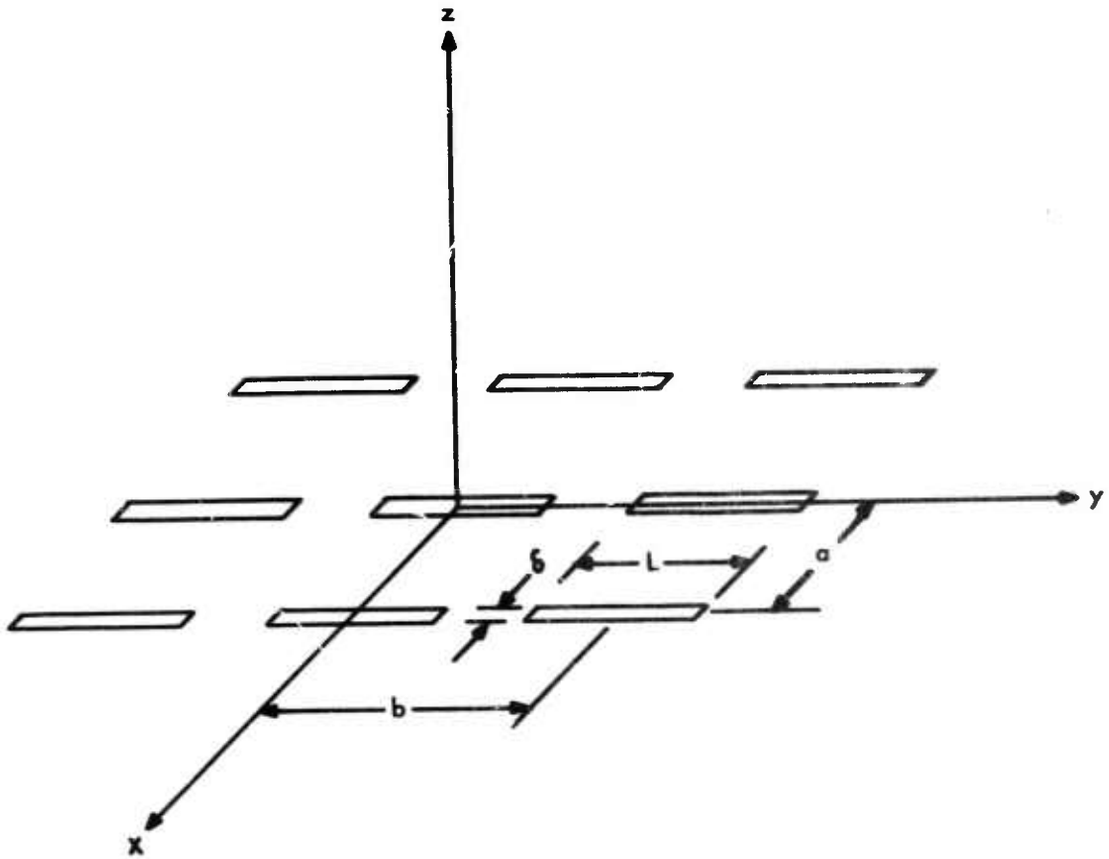

Figure B-1. Infinite Dipole Array (Ground Plane Not Shown)

angle between its direction of propagation and the X axis. Similarly, a current distribution having variations in both the X and Y directions can be represented by a double Fourier Series. In this instance, each term of the series will have a specified wavelength along both the X and Y axis which specifies the propagation direction of the plane wave. Once the set of plane waves which, when summed, represents the current distribution is found, the electric and magnetic fields at a single dipole surface is known. The complex power radiated from the dipole is

$$P_{complex} = \frac{1}{2} \int\int_{dipole} E \times H^* \cdot ds. \tag{1}$$

Equating the power radiated by a dipole to the input power, the dipole input impedance is obtained as

$$Z = \frac{1}{|I_o^2|} \int\int E \times H^* \cdot ds \tag{2}$$

where I_o is the current at the point at which the impedance is being measured. Instead of using only the fields produced by the dipoles shown in Figure B-1, the effect of the ground plane is accounted for by subtracting another identical set of fields displaced by twice the ground plane spacing. The resulting expression for the input impedance appears very complicated, but can be interpreted. The driving point impedance for a dipole in an array of dipoles a distance S above a ground plane is

$$Z_{in} = \frac{1}{2}\left(\frac{2}{\pi}\right)^2 \frac{L^2}{ab}\sqrt{\frac{\mu}{\epsilon}}\left\{\frac{\sin\left(\frac{\pi\delta}{\lambda}\cos\theta_{xs}\right)}{\frac{\pi\delta}{\lambda}\cos\theta_{xs}} \times \frac{\cos\left(\frac{\pi L}{\lambda}\cos\theta_{ys}\right)}{1-\left(\frac{2L}{\lambda}\cos\theta_{ys}\right)^2}\right\}^2$$

$$\times \frac{\sin^2\theta_{ys}}{\cos\theta_{zs}}\left[1 - e^{-j2kS\cos\theta_{zs}}\right] + \frac{1}{2}\left(\frac{2}{\pi}\right)^2 \frac{L^2}{ab}\sqrt{\frac{\mu}{\epsilon}} \sum_{m=-\infty}^{\infty}\sum_{n=-\infty}^{\infty}$$

$$\left\{\frac{\sin\left[\frac{\pi\delta}{a}\left(\frac{a}{\lambda}\cos\theta_{xs}+m\right)\right]}{\frac{\pi\delta}{a}\left(\frac{a}{\lambda}\cos\theta_{xs}+m\right)} \times \frac{\cos\left[\frac{\pi L}{b}\left(\frac{b}{\lambda}\cos\theta_{ys}+n\right)\right]}{1-\left[\frac{2L}{b}\left(\frac{b}{\lambda}\cos\theta_{ys}+n\right)\right]^2}\right\}^2$$

$$\times \frac{\left[1-(\cos\theta_{ys}+n\frac{\lambda}{b})\right]\left[1-e^{-j2\gamma_{mn}S}\right]}{\gamma_{mn}/k} \tag{3}$$

where the term m = 0, n = 0 is excluded from the double summation

L, a, b, and δ are defined in Figure B-1

$\sqrt{\frac{\mu}{\epsilon}}$ = 377 ohms

λ is the free space wavelength

θ_{xs}, θ_{ys}, and θ_{zs} are the angles measured between the main beam direction and the X, Y, and Z axis respectively

$k = \frac{2\pi}{\lambda}$

S is the distance between the plane of the dipole array and the ground plane

$$\gamma_{mn} = k\sqrt{1 - [(\cos\theta_{xs} + \frac{m\lambda}{a})^2 + (\cos\theta_{ys} + \frac{n\lambda}{b})^2]}$$

and is the propagation constant of the m, n^{th} plane wave in the Z direction. It is positive real or negative imaginary.

To better understand equation (3), consider an array of N dipoles driven by current sources and phased to produce a beam in the direction $\theta_z = 0$. The power radiated by the array of dipoles is

$$P_{radiated} = \frac{N}{2} V I^* = \frac{N}{2} |I^2| Z_{input}. \qquad (4)$$

Using equation (3), the power in the main beam (all terms under $\sum\sum$ correspond to grating lobes) is

$$P = N I^2 \frac{L^2}{ab\pi^2} \sqrt{\frac{\mu}{\epsilon}} .$$

If the array is steered to the direction θ_x, θ_y, the main beam is broadened by

$$1/\cos\theta_z = 1/\sqrt{1 - \cos^2\theta_x - \cos^2\theta_y}$$

and its peak power density varies with the element power pattern. Examining the first term of equation (3), the beam broadening factor is present so that the rest of the factors must be the element power pattern which happens to be complex. The real part of the

element power pattern is easily shown to be proportional to the power pattern of a dipole with the assumed current distribution above an infinite ground plane.

Using the concept of a complex power pattern yields an understanding of equation (3). The first term is the element power pattern evaluated at the main beam peak (i. e., $\cos \theta_{xs}$ and $\cos \theta_{ys}$ have replaced the general values $\cos \theta_x$ and $\cos \theta_y$) times the main lobe width. Similarly, each term under the double summation represents the power in a grating lobe. The power in the grating lobe is obtained as the element power pattern evaluated at the grating lobe peak times the beam broadening factor. Since the elements are located on a rectangular grid, grating lobes are formed as the angles

$$\cos \theta_x = \cos \theta_{xs} + \frac{\lambda}{a} m$$

$$\cos \theta_y = \cos \theta_{ys} + \frac{\lambda}{b} n \qquad (6)$$

Note that equation (3) converges fairly rapidly if a reasonable dipole ($L = 0.5\lambda$, $\delta = 0.1\lambda$) is assumed. For these dimensions terms for $|n| > 3$ or $|m| > 15$ are negligible and a useful formula for the dipole driving point impedance in a large array is available.

B. 2. 2 The Relationship Between Element Pattern, Array Patterns, and Element Driving Point Impedance

This section will first discuss concepts necessary to understand the operation of a phased array element. It will then discuss the specific case of a dipole above a ground plane phased array element. The following two definitions are needed:

1) Source pattern: $S(\theta, \phi)$: The pattern measured in the array with one element driven and all others match terminated.

2) Element pattern: $E(\theta, \phi)$: The pattern of the isolated element and ground plane.

The array pattern may be expressed in many ways. One common method is with the source pattern as shown below:

$$A(\theta,\phi) = S(\theta,\phi) \sum \sum V_{mn} e^{j(2\pi/\lambda)(md_x \sin\theta\cos\phi + nd_y \sin\theta\sin\phi)} \qquad (7)$$

where $S(\theta,\phi)$ is the source pattern, V_{mn} is the source excitation voltage, d_x and d_y are element spacings in the X and Y directions, and θ and ϕ are the usual spherical coordinates. The double sum term is periodic.

If a grating lobe resulting from this periodicity is allowed in real space, it will be suppressed only by the source function $S(\theta, \phi)$. $S(\theta, \phi)$ is the result of the direct radiation of the excited element and the fields radiated by the parasitically excited elements. Assuming that the scattered radiation pattern is identical to the element pattern, the source pattern is

$$S(\theta, \phi) = E(\theta, \phi) \sum \sum C_{mn} e^{j(2\pi/\lambda)(md_x \sin\theta \cos\phi + nd_y \sin\theta \sin\phi)} \tag{8}$$

where $E(\theta, \phi)$ is the element pattern and C_{mn} describes the field coupled to the mn^{th} element. Note that the $\sum \sum$ of equation (8) is periodic with the same period as the array factor. Hence, if $E(\theta, \phi)$ is broad, $S(\theta, \phi)$ is approximately periodic also.

Aperture type elements have broad element patterns which fall to zero along the ground plane in the "H" plane, but not in the "E" plane. Thus $S(\theta, \phi)$, which is approximately periodic in the "E" plane with the same periodicity as the array factor, will have the same gain in the grating lobe direction as in the main beam direction. If the element spacing is large enough to allow the grating lobe into real space, a sidelobe comparable to the main beam peak will occur. Hence, if array patterns with low sidelobes are to be achieved, the elements must be spaced to keep the entire grating lobe out of real space.

A dipole element has a relatively narrow pattern which goes to zero along the ground plane. Hence, $S(\theta, \phi)$ cannot be considered periodic. However, it is desirable to determine $S(\theta, \phi)$ because it describes the array gain variation with scan angle as shown by equation (8). To determine the source pattern of a dipole, the array pattern is written in terms of the dipole current and element pattern.

$$A(\theta, \phi) = E(\theta, \phi) \sum \sum I_{mn} e^{j(2\pi/\lambda)(md_x \sin\theta \cos\phi + nd_y \sin\theta \sin\phi)} \tag{9}$$

where I_{mn} is the current on the mn^{th} element and $E(\theta, \phi)$ is the pattern of a dipole above a ground plane. The ratio of currents I_{mn}/I_{pq} is also the ratio of the driving voltages. However, the magnitude of I_{mn} is dependent upon the steering angle as shown by

$$I_{mn} = \frac{V_{mn}}{Z_G + Z_D(\theta, \phi)} \tag{10}$$

where Z_G is the generator impedance and $Z_D(\theta, \phi)$ is the driving point impedance when the beam is steered to θ, ϕ. Thus, when a linearly polarized array of dipoles is steered, the

peak of the radiated field does not vary with the steering angle as the factor of the isolated element, $E(\theta, \phi)$. Instead, it varies with the element factor times the variable ratio of the current at the angle θ, ϕ to the current at the angle $\theta = 0 = \phi$. Thus, from equations (8), (9), and (10) the source pattern of a dipole in an array is

$$S(\theta, \phi) = E)\theta, \phi) \frac{I(\theta, \phi)}{I(0, 0)} = E(\theta, \phi) \frac{Z_G + Z_D(0, 0)}{Z_G + Z_D(\theta, \phi)} = E(\theta, \phi) \frac{1 - \Gamma(\theta, \phi)}{1 - \Gamma(0, 0)} \tag{11}$$

when the generator is matched to the transmission line. Thus, the source pattern, which describes the variation in the peak gain of a phased array as a function of scan angle, has been determined as a function of the element factor and the driving point impedance. Since the element factor of a dipole is well known, the major effort in the dipole investigation has been to determine the driving point impedance.

B. 3 FINITE SIZED DIPOLE ARRAYS

Most of the large phased arrays being constructed are large enough to allow most of the central elements to be considered as an element in an infinite array. In the design of the array element and its initial testing, a reasonably sized array must be chosen to simulate the infinite array environment. For dipole arrays, the input impedance vs. scan angle for different sized arrays can be computed for thin dipoles. From these computations the array size needed for developing the dipole can be determined. However, before relying upon an approximate theory, it is necessary that experimental tests confirm the theory.

B. 3. 1 Experiment and Theory

To close the gap between theory and experiment, a small phased array of dipoles was tested by Lincoln Laboratory.[3] Two different arrays were tested, an 8×8 array and a 7×7 array, each with a perimeter of dummy elements. The dipoles were $3/8\lambda$ long, had a length to diameter ratio of 13. 6, and were fed by a split-tube balun. Thus, the dipoles used in the experiment were a poor approximation of the thin dipoles usually assumed in the theoretical computation of mutual impedance between dipoles. Each array was steered in the E plane, H plane, and 45° plane, and the input impedance of a central element measured. Next, the input impedance was computed assuming thin $3/8\lambda$ long elements and neglecting the presence of baluns. Good correlation between computed and

measured data was obtained for all scan angles. In all cases, the deviation in the magnitude of the reflection coefficient was within 26%, while the phase deviation was less than 24 degrees. For most scan angles the correlation was much better. Because of the correlation between experimental and theoretical data, theory will be used to estimate the performance of dipoles in large phased arrays.

B. 3. 2 Linearly Polarized Dipoles on a Square Grid

Linearly polarized dipoles have been investigated in detail.[2] The active input impedance to half-wave and short dipoles has been determined as a function of element spacing (spacings considered are 0.5λ, 0.6λ, 0.7λ, and 0.8λ) and element height above the ground plane (data with heights of 0.25λ, 0.125λ, and data with no ground plane are available in referenced work). A typical set of data is shown in Figures B-2 and B-3. This data is similar to that of the Lincoln Laboratory except that the generator output impedance is the complex conjugate of the input impedance to a single dipole above a ground plane (the previous data has the generator output impedance equal to the complex conjugate of the active driving point impedance at broadside). Note that matching the isolated element produces better than a 2.3:1 match for the array element for all scan angles within an 83° included angle cone. Hence, if it is desired to minimize the worst VSWR, the isolated element may be matched as a first cut. A better match would be obtained if the real part of the generator impedance were 100 ohms instead of 85.66 ohms. The E and H plane source patterns are shown in Figure B-3. They are obtained using equation (11) and Figure B-2. Note that the source pattern is dependent upon the generator impedance and that the E and H plane beamwidths would be more nearly equal if the real part of the generator impedance were made 100 ohms.

B. 3. 3 Crossed Dipoles on a Triangular Grid

Dipoles on square grid arrays have been discussed. However, the scan requirements of many arrays can be met with fewer elements spaced on a triangular grid.[4] Since there is no published data on this subject,* the problem was investigated. Two configurations were studied. The first is shown in Figure B-4. It consists of 0.4λ crossed

*Bliss Diamond of Lincoln Laboratory has indicated that he has data on infinite arrays of crossed dipoles on a triangular grid. This work is not presently available for dissemination.

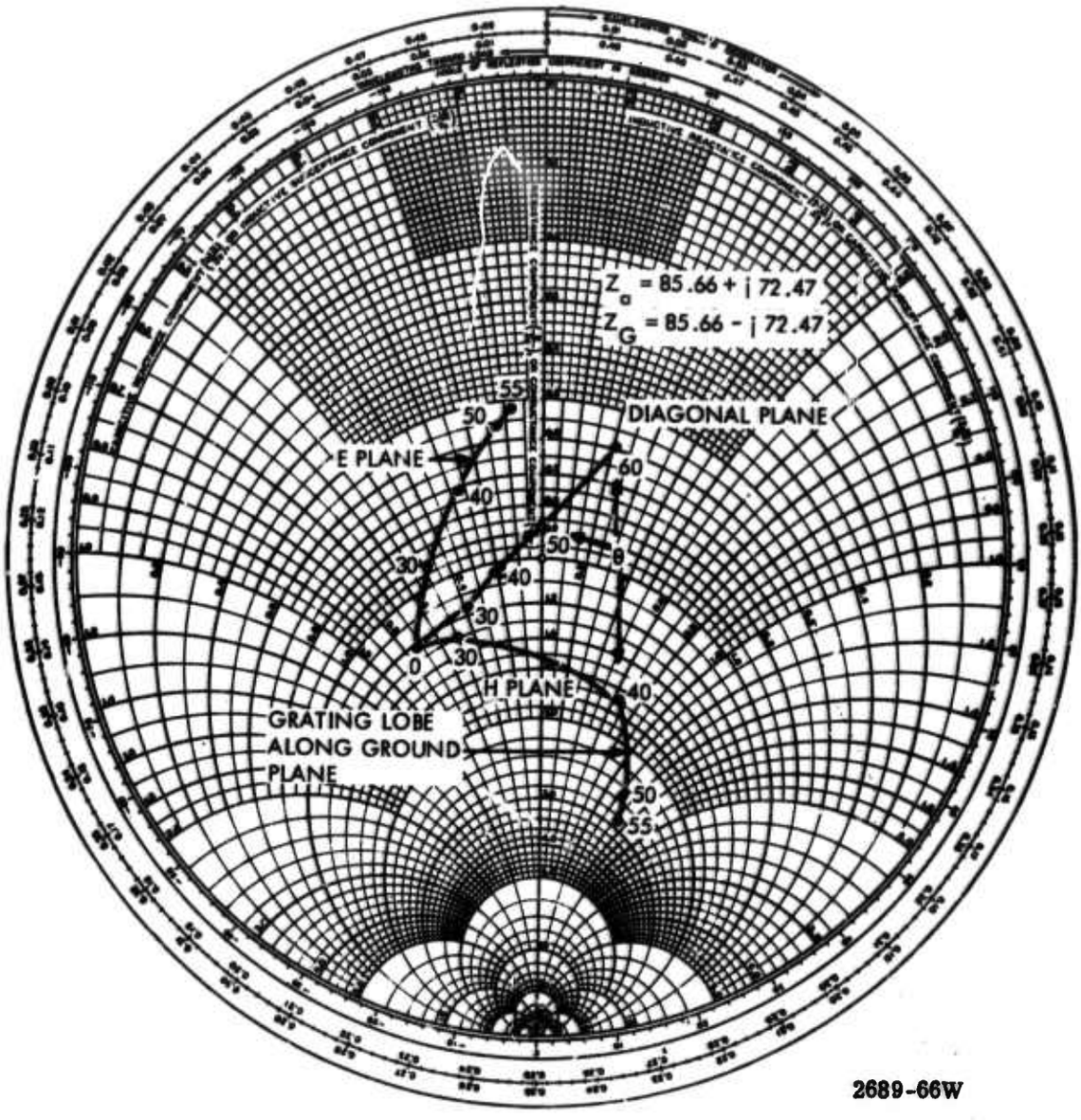

Figure B-2. Driving Point Impedance with Scan Angle for Center Element of 9 × 7 Array of λ/2 Dipoles λ/4 Above a Ground Plane with Element Spacing 0.6λ Square. Generator Impedance is Conjugate of Isolated Element Impedance (Z_a)

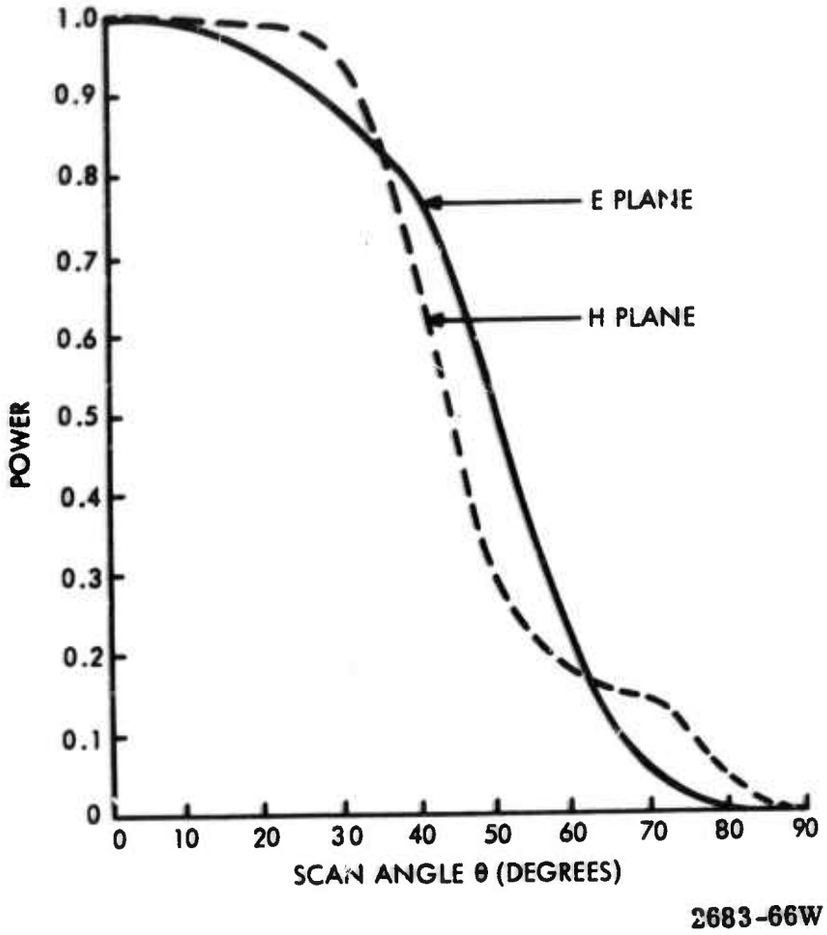

Figure B-3. E and H Plane Source Pattern of Center Element of 9 × 7 Array of λ/2 Dipoles λ/4 Above a Ground Plane with Element Spacing 0.6 λ square. Generator Impedance is conjugate of Isolated Element Impedance.

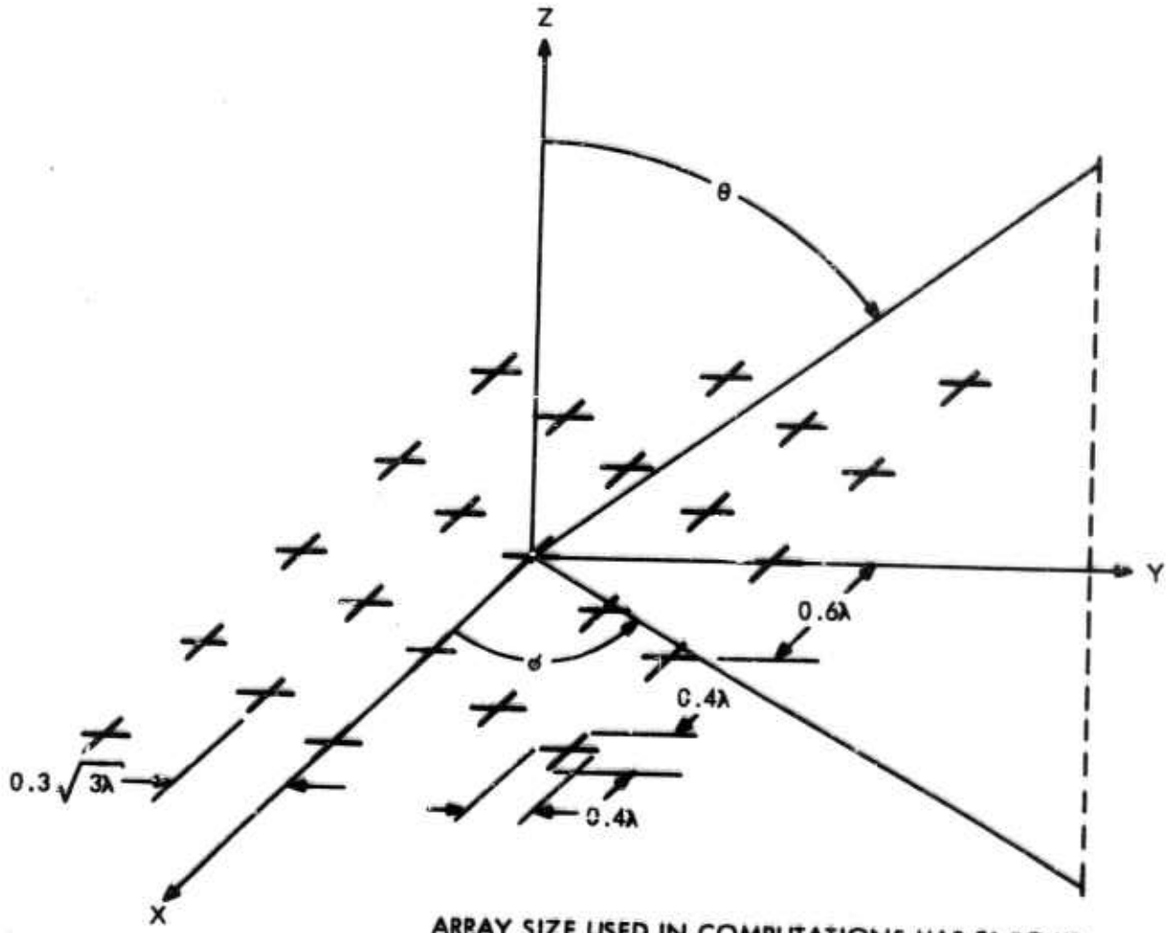

ARRAY SIZE USED IN COMPUTATIONS HAS 21 ROWS IN X DIRECTION, 13 ROWS IN Y DIRECTION AND 137 ELEMENTS.

2685-66 W

Figure B-4. Crossed Dipoles on a Triangular Grid (Ground Plane which is λ/4 below dipole is not shown)

dipoles spaced 0.6λ apart on an equilateral triangular grid 0.25λ above a ground plane. The 0.4λ dipole length was chosen as a realistic dipole length. The second consists of 0.2λ crossed dipoles spaced 0.3λ apart on an equilateral triangular grid 0.25λ above a ground plane. This configuration was chosen to determine the coupling effects for close spacings. The results are presented at the end of this section. A number of assumptions were made in the analysis. They consist of the following:

1) The dipoles are thin.

2) All Y oriented dipoles (hereby called Y dipoles) have the same input impedance.

3) All X dipoles have the same input impedance.

4) All dipoles are excited with equal amplitude incident waves.

5) The phases of the incident waves are chosen to form a ramp phase front at the aperture.

6) The elements are excited by realistic (not current) sources.

The active driving point impedance of the dipole is required. To determine this impedance it is first necessary to compute the mutual impedance between dipoles. Since crossed dipoles above a ground plane are to be examined, the mutual impedance between elements which are parallel or perpendicular and which do or do not lie in the same plane must be obtained. Because of the general nature of this problem, the integral method of Baker and LaGrone[5] is used. With this data, the input impedance to the central Y dipole can be computed as

$$Z_{in} = Z_{11} - Z_{11}\text{image} + \sum_{y\ \text{dipoles}} \sum \left({}_yZ_{mn} - {}_yZ_{mn}\text{image}\right) \frac{I_{mn}}{I_{11}}$$

$$+ \sum_{x\ \text{dipoles}} \sum \left({}_xZ_{mn} - {}_xZ_{mn}\text{image}\right) \frac{I_{mn}}{I_{11}} \qquad (12)$$

where $\sum\sum$ excludes the m = 1 = n term, ${}_yZ_{mn}$ is the mutual impedance between the mn^{th} Y dipole and the central Y dipole, ${}_xZ_{mn}$ is the mutual impedance between the mn^{th} X dipole and the central Y dipole, Z_{11} is the self impedance of the dipole, I_{11} is the current on the

central Y dipole, and ${}_xI_{mn}$ and ${}_yI_{mn}$ are the currents on the X and Y mn^{th} dipoles. A similar expression may be written for the central X dipole. By using assumptions 2 through 5, equation (12) may be rewritten as

$$ {}_yZ_{in} = Z_y + \frac{I_x}{I_y} Z_c = Z_o \frac{1 + \Gamma_y}{1 - \Gamma_y} \tag{13} $$

$$ {}_xZ_{in} = \frac{I_y}{I_x} Z_c + Z_x = Z_o \frac{1 + \Gamma_x}{1 - \Gamma_x} \tag{14} $$

where Z_o is the characteristic impedance of the feed cable, Γ_x and Γ_y are the reflection coefficients of the X and Y dipoles and

$$ Z_y = Z_{11} - Z_{11}\text{image} + \sum_{y\ \text{dipoles}} \sum ({}_yZ_{mn} - {}_yZ_{mn}\text{image}) e^{j\frac{2\pi}{\lambda} \sin\theta(d_x \cos\phi + d_y \sin\phi)} \tag{15} $$

$$ Z_c = \sum_{x\ \text{dipoles}} \sum ({}_xZ_{mn} - {}_xZ_{mn}\text{image}) e^{j\frac{2\pi}{\lambda} \sin\theta(d_x \cos\phi + d_y \sin\phi)} . \tag{16} $$

Z_y and Z_c and Z_x as obtained from the computer are given in Tables B-1 and B-2.

In the principal planes, ${}_xZ_{in}$ and ${}_yZ_{in}$ are given directly by the values of Z_x and Z_y in Tables B-1 and B-2. In the planes $\phi = 30°$ and $\phi = 60°$, the ratio of I_x/I_y must be known before the total input impedances to the X and Y dipoles are obtained. Thus, the relative phase and amplitude of the waves incident upon the X and Y dipoles must first be decided upon. Next, equations (13) and (14) are solved for I_x/I_y and the same equations are then used to determine ${}_xZ_{in}$ and ${}_yZ_{in}$. To solve for the driving point impedances, let the crossed dipoles be fed by a quadrature hybrid with the wave incident upon the X dipole leading that in the Y dipole by 90°. The results of these computations are shown in Figures B-5, B-6, B-7, and B-8. In all cases, the Smith Charts have been plotted by adding + j115 to the computed impedance and dividing by 45.3 (the self impedance of the dipole is 42-j113). From these figures, it can be seen that matching the isolated dipoles would provide an excellent first cut try to matching the array element.

TABLE B-1

CONTRIBUTIONS TO IMPEDANCE $_yZ_{in}$ at F_o

θ_s	$Z_y;\phi_s = 0°$	$Z_y;\phi_s = 30°$	$Z_y;\phi_s = 60°$	$Z_y;\phi_s = 90°$	$Z_c;\phi_s = 0$ or $\phi_s = 90$	$Z_c;\phi_s = 30$	$Z_c;\phi_s = 60$
0	56.8-j152	56.8-j152	56.8-j152	56.8-j152	0	0	0
10	60.5-j151	60.4-j151	58.1-j150	55.7-j150	0	0.6-j.2	0.9-j.3
20	59.9-j146	58.0-j144	55.2-j142	52.3-j144	0	3.2-j.3	3.0-j.6
30	66.3-j137	60.4-j135	49.9-j134	44.8-j134	0	6.7-j.2	6.7-j1.6
40	64.6-j124	57.8-j120	40.9-j120	33.8-j121	0	11.4+j3.5	11.5+j.2
50	67.4-j108	53.0-j105	32.7-j109	22.7-j115	0	14.7+j7.6	15.2+j1.0
60	58.5-j84.8	46.8-j72.4	23.6-j103	11.6-j111	0	17.8+j21.4	17.5+j7.0
70	38.0-j72.0	43.9-j51.4	11.4-j99	6.6-j109	0	20.5+j31.6	12.6+j13.4

TABLE B-2

CONTRIBUTIONS TO IMPEDANCE $_xZ_{in}$ at F_o

θ_s	$Z_x;\phi_s = 0°$	$Z_x;\phi_s = 30°$	$Z_x;\phi_s = 60°$	$Z_x;\phi_s = 90°$
0	58.8-j149	58.8-j149	58.8-j149	58.8-j149
10	56.7-j147	57.8-j149	58.6-j151	58.8-j151
20	5.13-j142	55.7-j144	58.8-j141	62.3-j142
30	44.6-j135	48.9-j135	60.7-j136	64.4-j133
40	35.5-j125	42.4-j125	55.9-j120	66.6-j113
50	22.2-j114	32.3-j116	53.6-j107	63.5-j95.1
60	11.7-j109	21.3-j105	48.5-j89.6	61.0-j50.0
70	5.4-j108	17.4-j96.7	29.8-j79.5	60.5-j24.0

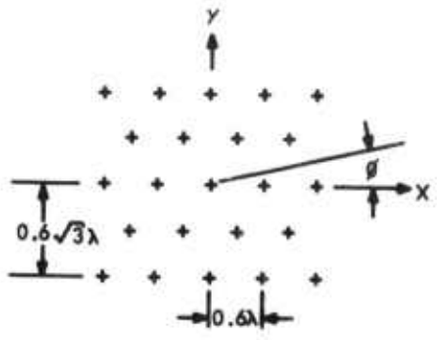

ARRAY CONSISTS OF 21 COLUMNS
13 ROWS, 137 ELEMENTS

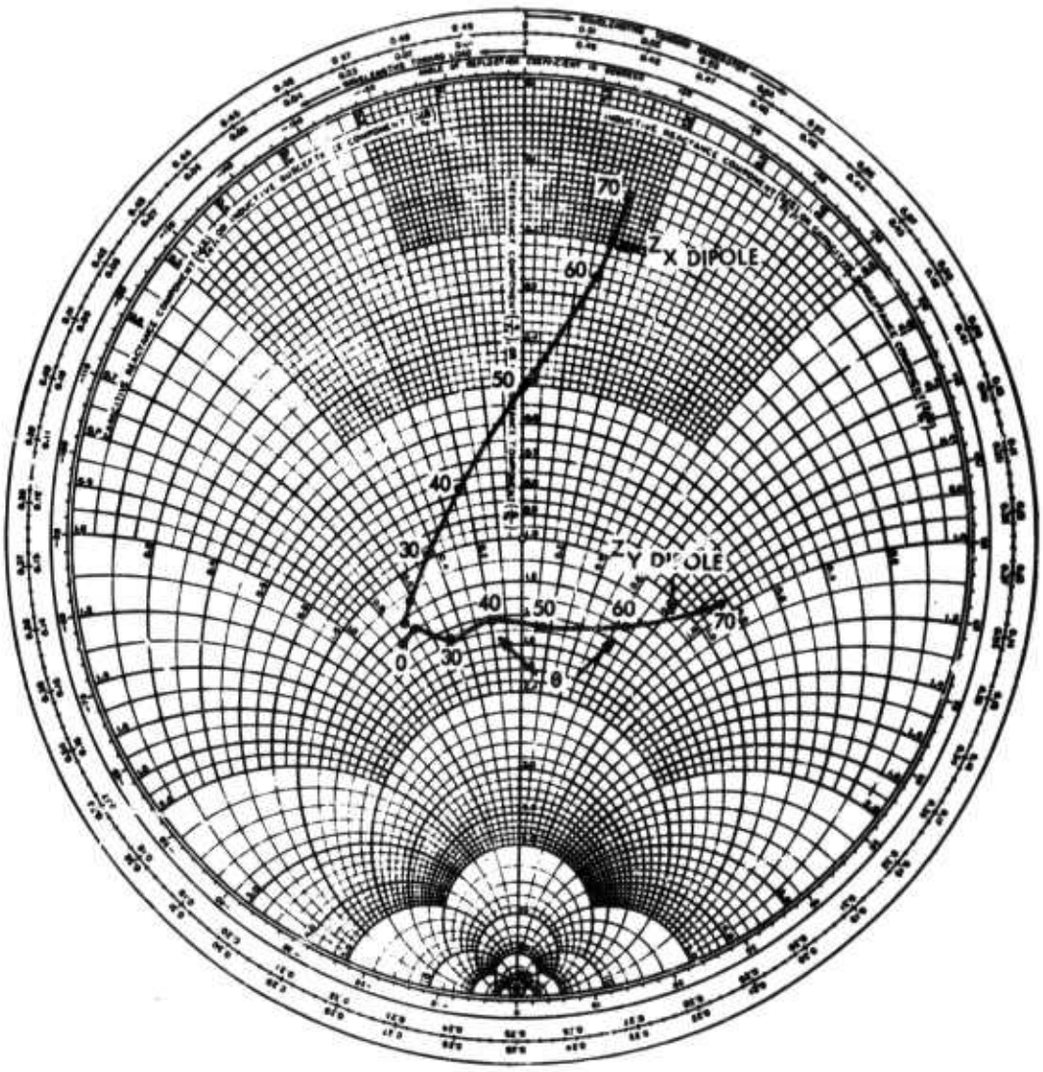

2677-66W

Figure B-5. Input Impedance of X and Y Dipoles in $\phi = 0°$ Plane (Circular Polarization).

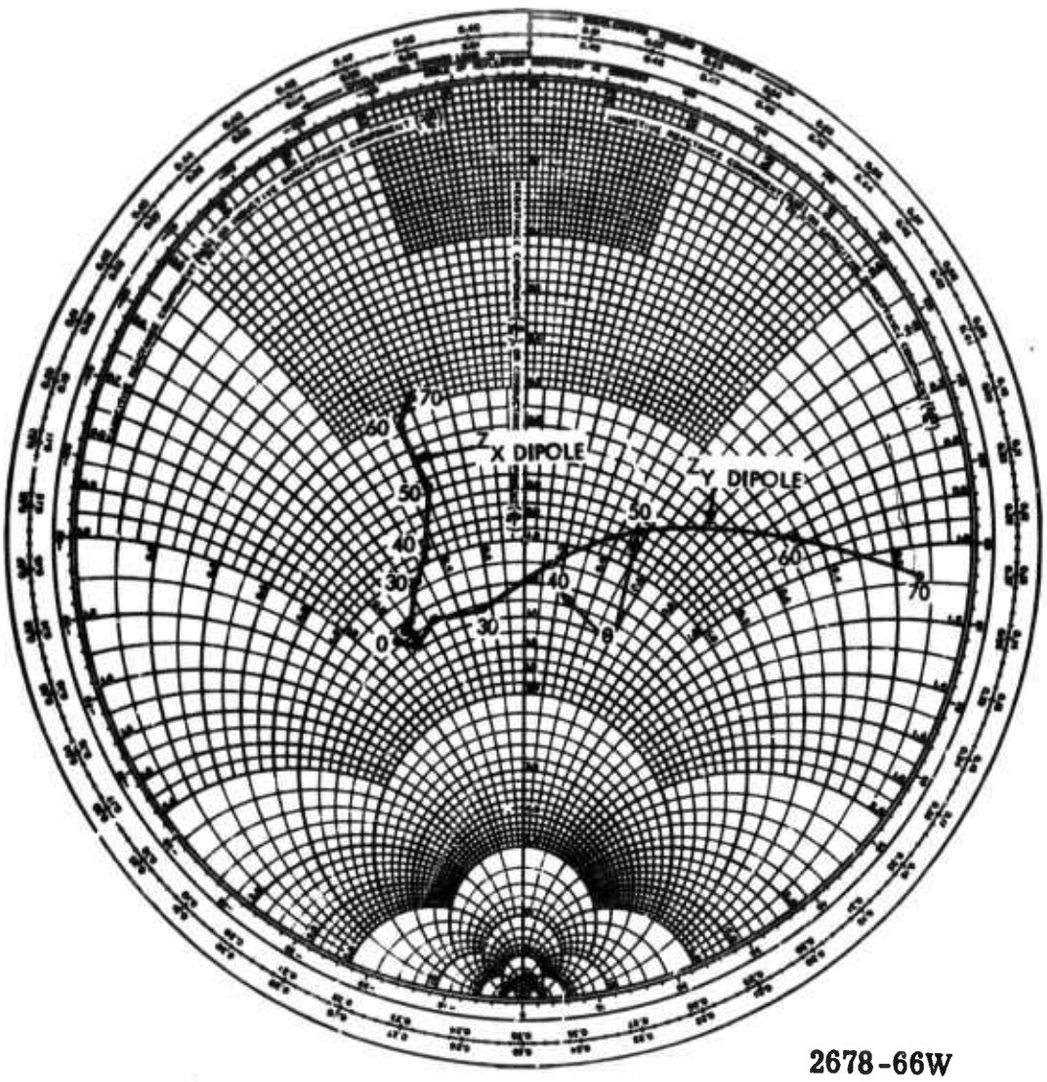

2678-66W

Figure B-6. Input Impedance of X and Y Dipoles in $\phi = 30°$ Plane (Circular Polarization)

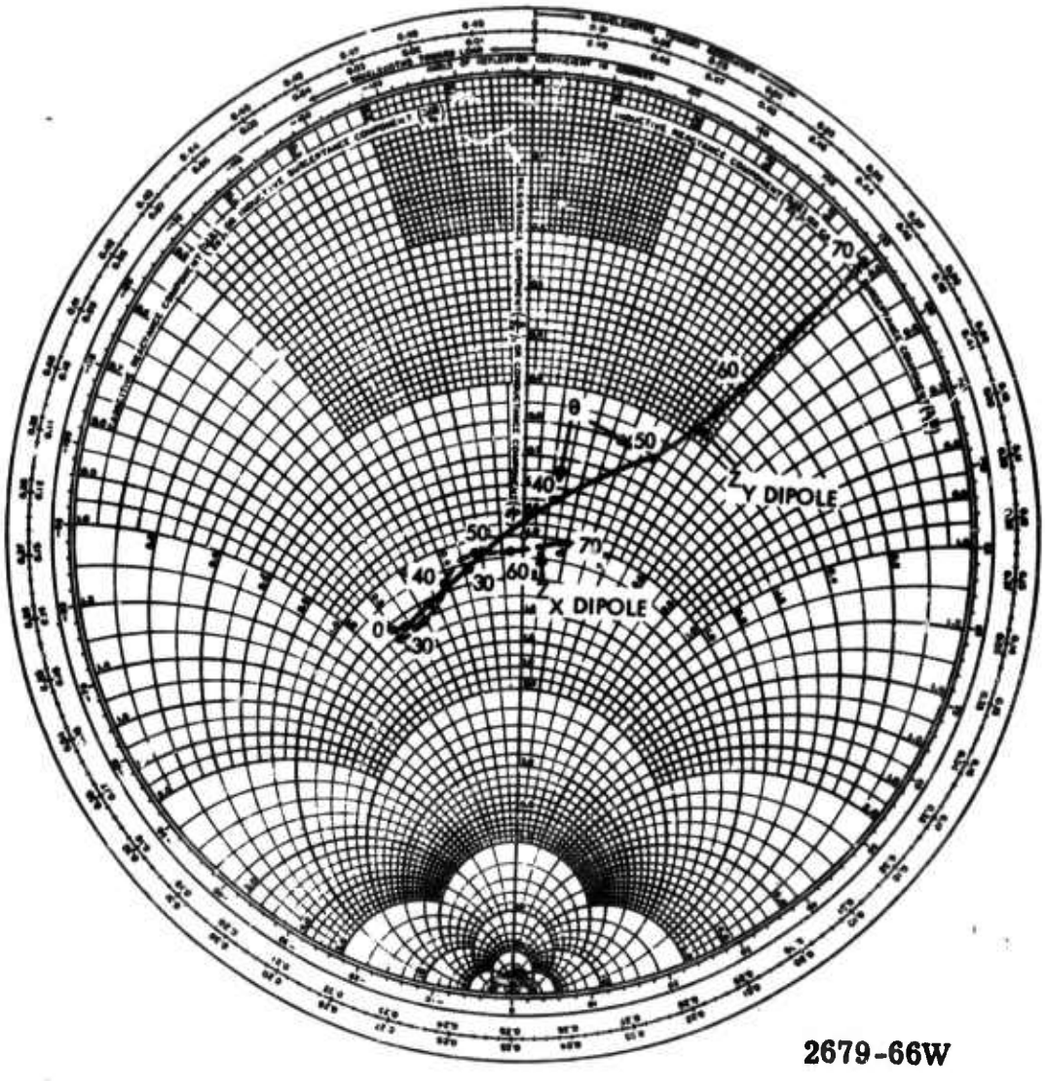

2679-66W

Figure B-7. Input Impedance of X and Y Dipoles in $\phi = 60°$ Plane (Circular Polarization)

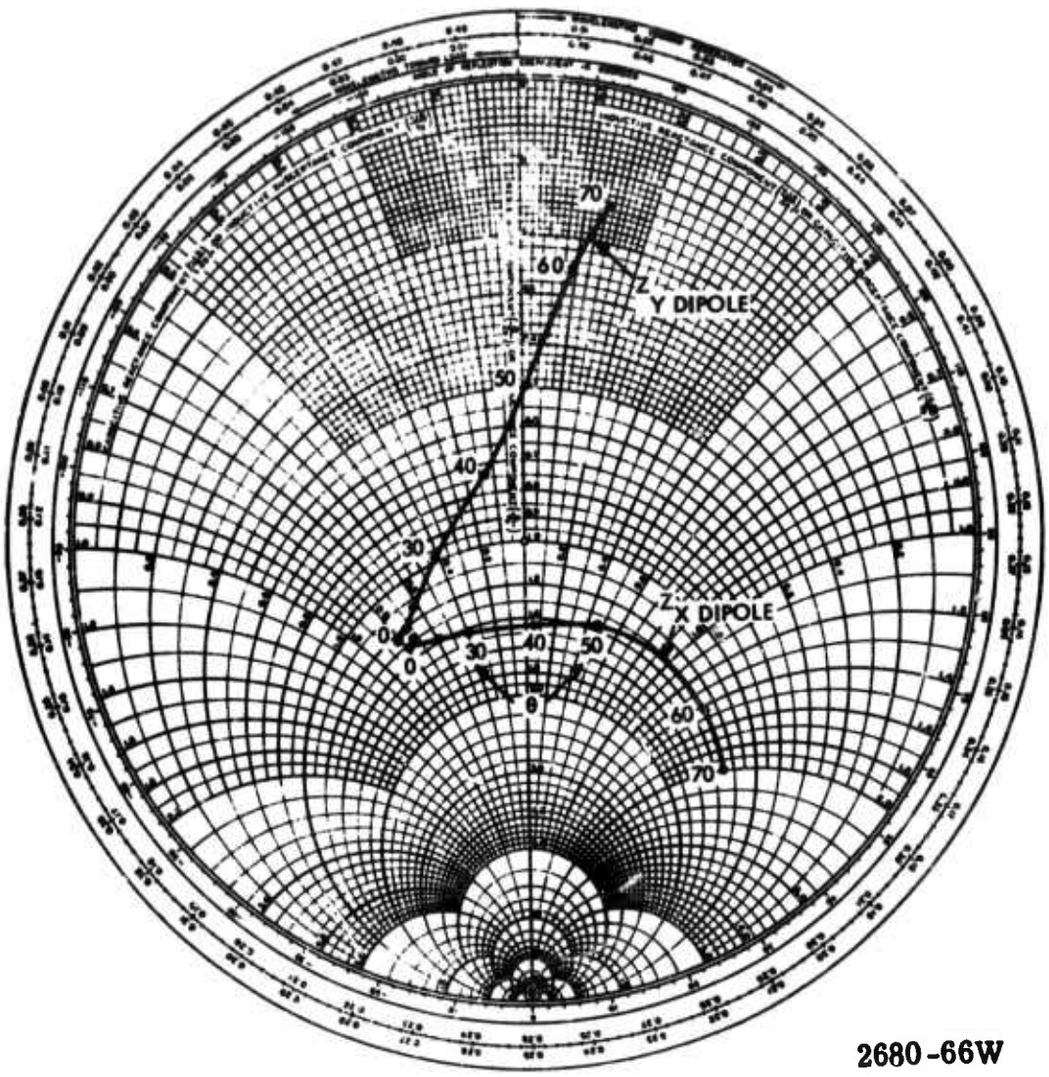

2680-66W

Figure B-8. Input Impedance of X and Y Dipoles in $\phi = 90°$ Plane (Circular Polarization)

Principal plane patterns for both the X and Y dipoles are obtained using Figures B-5 and B-8 with equation (11). The results are shown in Figure B-9. Note that array effects broaden the E plane pattern considerably for both planes, but only affect the H plane pattern in the plane of scan which allows the grating lobe to enter real space. The grating lobe effect is gradual, first taking place at a scan angle of about 55°.

The reflected power in both the driven and orthogonal ports of the quadrature hybrid can be directly determined from Figures B-5, B-6, B-7, and B-8. The reflected powers are (assuming unity incident power to the driven port)

$$P_{driven} = |\Gamma_D|^2 = \frac{1}{4}(\Gamma_x - \Gamma_y)^2$$

$$P_{orthogonal} = |\Gamma_o|^2 = \frac{1}{4}(\Gamma_x + \Gamma_y)^2. \qquad (17)$$

The terms Γ_D and Γ_o can be obtained directly from a vector addition of Γ_x and Γ_y in Figures B-5 thru B-8. The results are shown in Figures B-10 and B-11.

Figure B-10 shows Γ_D as a function of θ and ϕ. For small values of θ, $|\Gamma_D|$ is independent of ϕ and the phase of Γ_D is dependent upon 2ϕ. At wide steering angles, where grating lobe effects begin to occur, $|\Gamma_D|$ repeats for 60° changes in ϕ and the phase of Γ_D varies as 2ϕ. Because of the variation of the phase of Γ_D with ϕ, it is seen that there is no simple matching network which reduces Γ_D independent of ϕ.

Figure B-11 plots Γ_o as a function of ϕ and θ. Note that, to a good approximation, Γ_o is independent of ϕ. Hence, a matching network may be used which reduces the peak value of Γ_o at wide angles at the expense of the match at $\theta = 0°$. It is because of the ϕ independence of Γ_o that the dipoles were not matched at broadside. Instead, Γ_o at $\theta = 45°$ was minimized.

The observed variation in Γ_o and Γ_D with ϕ is expected for circularly symmetric, circularly polarized elements because the coupling coefficients between driven ports or between orthogonal ports vary as 2ϕ, while the coupling between a driven port and an orthogonal port is independent of ϕ.[6]

The ellipticity ratio of the crossed dipoles was computed in the principal planes. From Figure B-9 it can be seen that the E and H plane beamwidths are approximately equal.

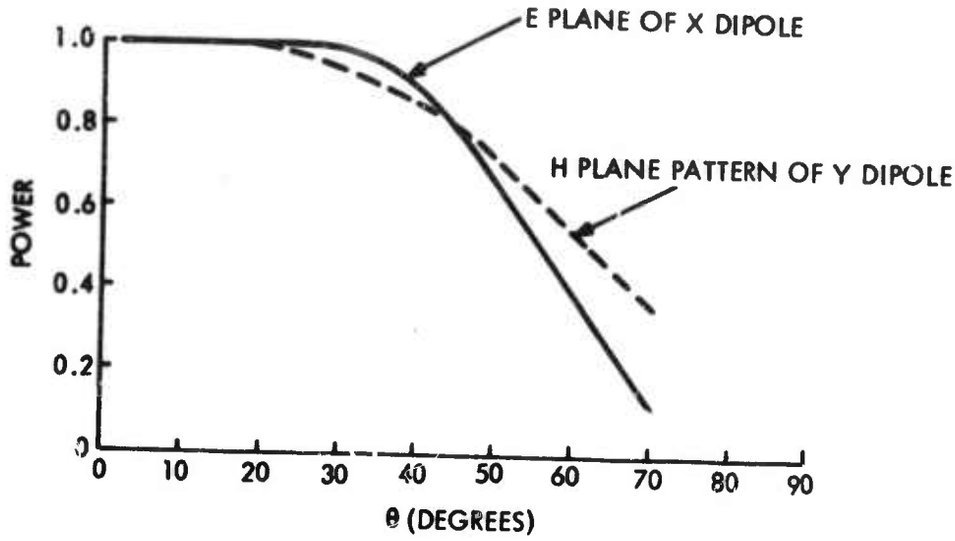

SOURCE PATTERNS OF X AND Y DIPOLES IN $\phi = 0°$ PLANE
(CLOSE ELEMENT SPACING ELIMINATES GRATING LOBE PROBLEMS)

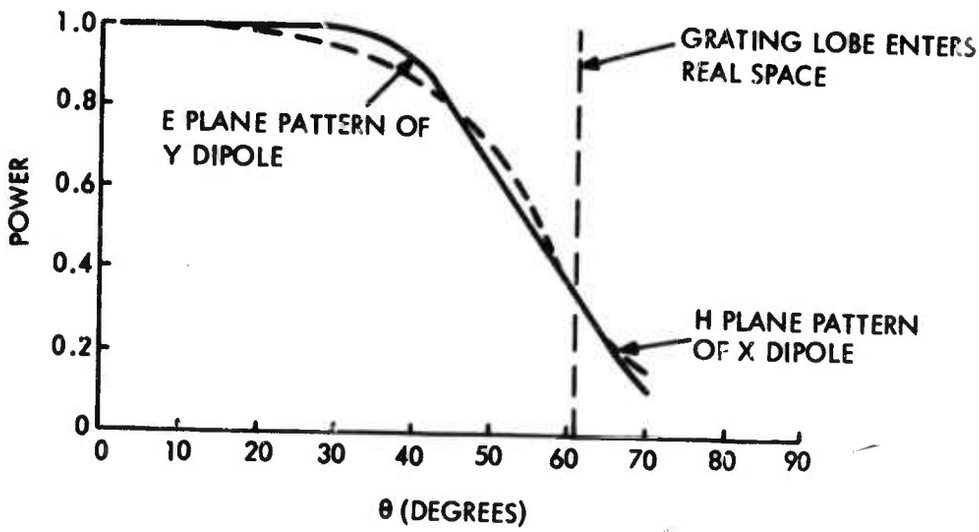

SOURCE PATTERNS OF X AND Y DIPOLES IN $\phi = 90°$ PLANE

2684-66W

Figure B-9. Principal Plane Patterns of X and Y Dipoles in a Triangular Grid Array.

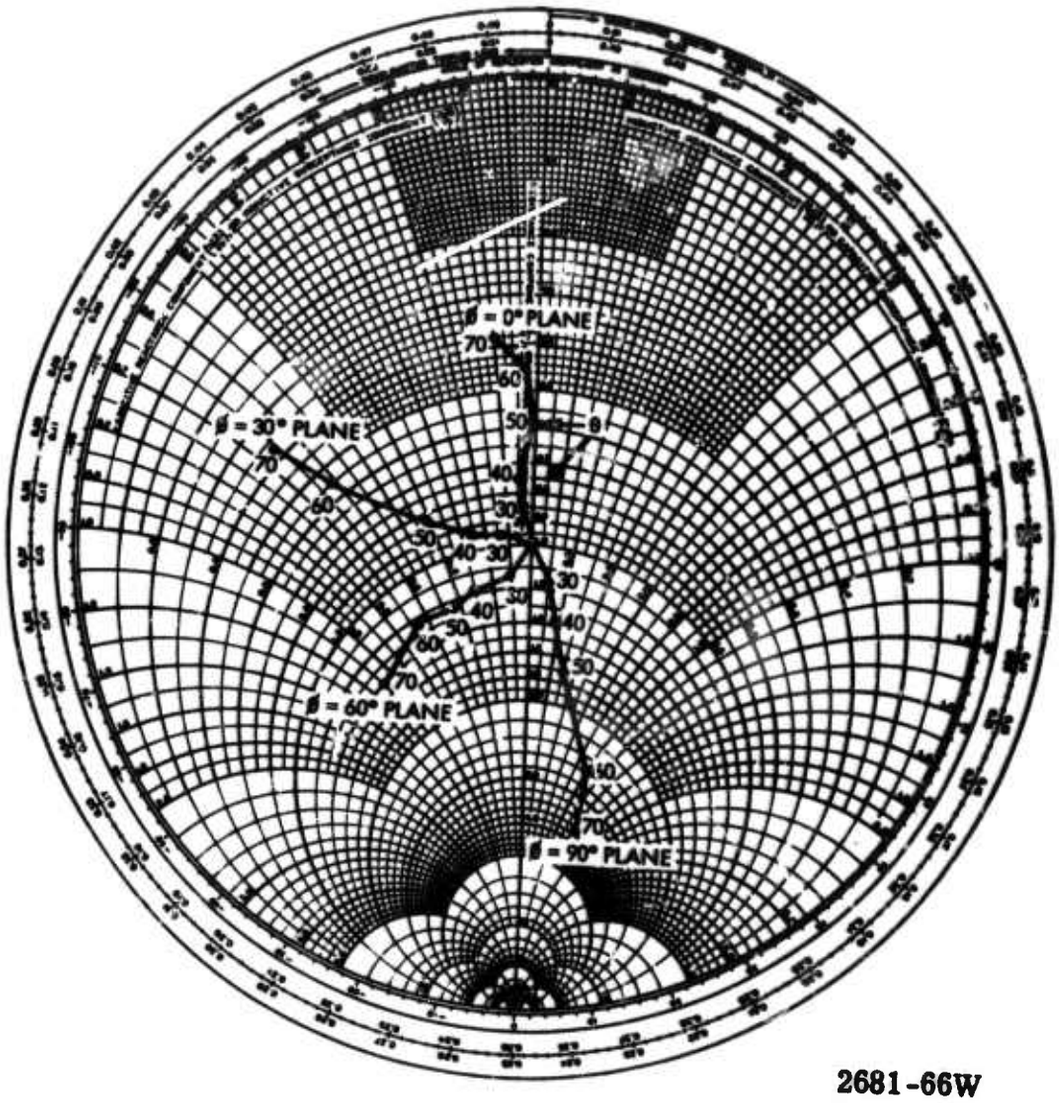

2681-66W

Figure B-10. Reflection Coefficient of Driven Port of Circularly Polarized Crossed Dipoles Vs. ϕ and θ

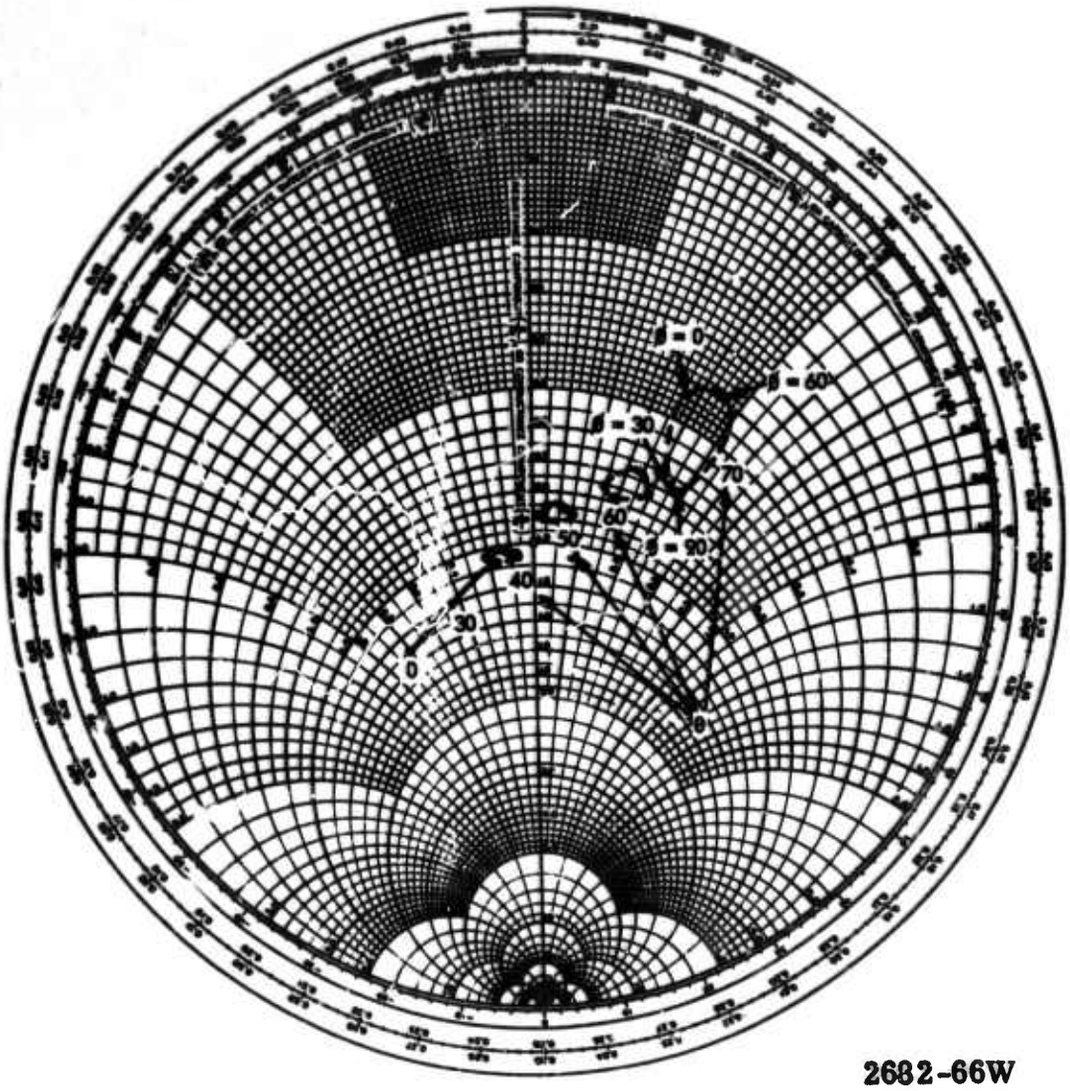

2682-66W

Figure B-11. Reflected Wave in Orthogonal Port of Circularly Polarized Crossed Dipoles Vs. ϕ and θ

However, the relative phase of the two patterns is dependent upon θ, which causes the ellipticity ratio to degrade. Computations show that the ellipticity ratio is better than 2 db out to 60° in the $\phi = 0°$ plane and out to 50° in the $\phi = 90°$ plane.

All the results thus far indicate that the dipole is a good phased array element for scan angles out to about 50 degrees from broadside. Two other results are required before this conclusion can be reached: the bandwidth capability, and a verification that the chosen array size is adequate to simulate the infinite array. It is known that an isolated dipole above a ground plane can be well matched over a reasonable bandwidth (a match better than 1.2:1 can easily be obtained for a 7 per cent bandwidth). Hence, it is the bandwidth of the mutual coupling that had to be investigated. To determine the mutual coupling bandwidth, the element length in wavelengths was kept constant, but the interelement spacing and height above a ground plane was reduced by 7 per cent. The results of these computations are shown in the first part of Table B-3.

TABLE B-3

DRIVING POINT IMPEDANCE

(FOR SCAN IN TWO PRINCIPAL PLANES, AT FREQUENCY F_o)

	Array Size = 137 Elements				Array Size = 447 Elements	
θ_s	$_xZ_{in};\phi_s = 0°$	$_xZ_{in};\phi_s = 90°$	$_yZ_{in};\phi_s = 0°$	$_yZ_{in};\phi_s = 90°$	$_yZ_{in};\phi_s = 0°$	$_yZ_{in};\phi_s = 90°$
0	64.5-j144	64.5-j144	65.3-j149	65.3-j149	66.9-j147	66.9-j147
10	62.1-j143	68.6-j144	67.3-j144	63.8-j146	67.0-j146	64.9-j144
20	57.6-j139	66.6-j136	67.6-j142	59.2-j139	67.6-j140	58.4-j137
30	49.5-j132	72.7-j126	71.2-j130	50.5-j130	69.3-j131	47.8-j130
40	37.0-j123	66.5-j110	68.5-j120	35.0-j123	71.4-j119	37.5-j122
50	23.1-j118	71.1-j92.0	69.1-j104	21.7-j118	65.4-j103	23.9-j118
60	11.1-j117	57.8-j66.2	58.2-j81.9	10.4-j117	61.2-j85.6	12.2-j118
70	4.2-j116	33.5-j44.2	37.2-j72.3	2.4-j119	40.1-j68.2	3.9-j120

Comparing these results to the principal plane impedances in Tables B-1 and B-2, it can be seen that the VSWR remains approximately the same. To check the array sample size used, the input impedance to the Y dipole in a 447-element array with the same reduced

spacing was also computed. These results are given in the last part of Table B-3. The two different array sizes give essentially the same central element input impedance.

Computations were also made on elements with a 3 per cent larger interelement spacing and height above the ground plane. In general, the VSWR was slightly worse everywhere but in the $\phi = 90°$ plane. In this plane, which is the H plane of the X dipole, the X dipole VSWR increased significantly at the angles $\theta = 60°$ and 70°, indicating that significant grating lobe effects were occurring However, if steering were limited to a 100 degree included angle cone, the worst VSWR in the principal planes would be about 2: 1.

The configuration consisting of 0.2λ dipoles spaced 0.3λ apart on an equilateral triangular grid 0.25λ above a ground plane will now be discussed. The close spacing was chosen to eliminate any possibility of grating lobe effects. The array size chosen to study this problem was about 7λ square, slightly larger than that used to study the 0.4λ long dipoles. The array consisted of 45 columns and 29 rows for a total of 653 elements. The driving point impedance was computed as a function of scan angle in the two principal planes. The data is presented in Figure B-12. The matching network used with the short dipoles is adjusted so that the broadside impedance lies in the same part of the Smith Chart as it does in Figure B-5 to allow easy comparison. Note that the equivalent generator impedance is not the complex conjugate of the isolated element impedance, since this matching technique is only valid for elements reasonably far apart (as far apart as possible without allowing the grating lobe into real space for any of the desired scan angles). Comparing Figures B-5 and B-12, it is seen that scanning in the H plane is independent of the element spacings as long as the grating lobe is kept well out of real space. For E plane scanning, the real part of the impedance variation is independent of the element spacing, but the reactive part is dependent upon element spacing. However, no significant change in scan performance out to 70° is observed. Hence, the scan performance of dipoles 0.6λ apart is almost as good as it is at closer spacings.

B.4 CURRENT SHEET ANTENNA

Discrete elements have been analyzed in both finite and infinite arrays. In general, the formulas for the element input impedance are quite complicated and must be solved using computer techniques. To obtain a simple expression for impedance variation with scan angle, an infinite current sheet above a ground plane will be analyzed. Since a

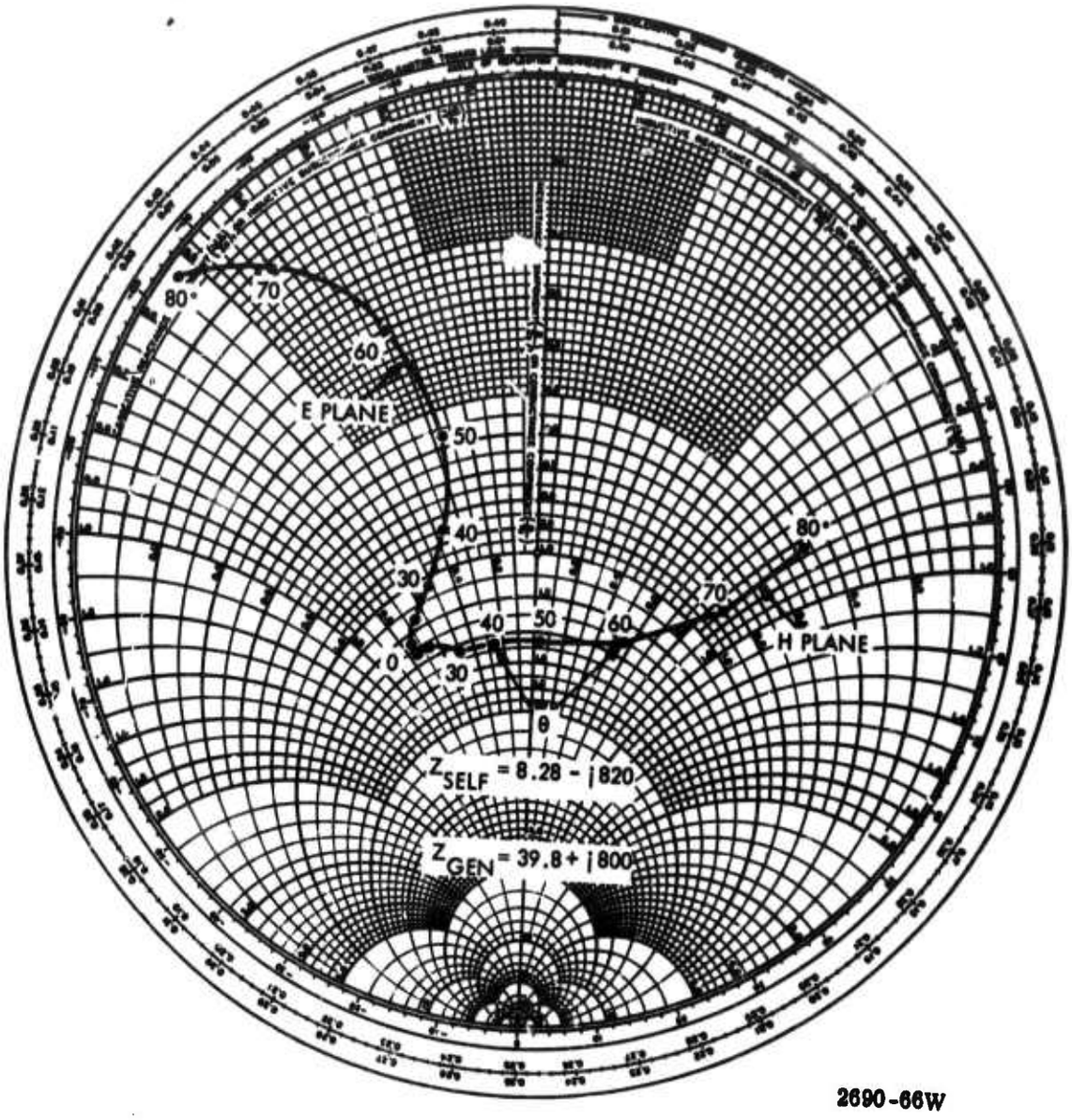

2690-66W

Figure B-12. Input Impedance of Array of 0.2λ Dipoles in Triangular Grid with a 0.3λ Interelement Spacing 653 Elements in Array

current sheet may be thought to be an infinite number of very closely spaced small dipoles, the impedance variation with scan angle will be similar to that obtained in Figure B-12.

The geometry to be analyzed consists of an infinite current sheet of Y directed current in the XY plane with a perfectly conducting sheet at Z = -d as shown in Figure B-13. The problem is to find the ratio of electric to magnetic field parallel to the sheet as a function of steering angle. To steer the beam, the current sheet is excited with uniform amplitude and a phase shift linear with distance. Assuming the plane wave direction is $\theta = \theta_o$, $\phi = 90°$, the ratios of magnetic to electric fields near the current sheet are

$$\frac{H_x}{E_y} = \frac{1}{\cos\theta_o}\sqrt{\frac{\epsilon}{\mu}} \qquad \text{for } Z = 0+ \tag{18}$$

$$\frac{H_x}{E_y} = \frac{-j}{\cos\theta_o}\sqrt{\frac{\epsilon}{\mu}}\cot\left(\frac{2\pi d}{\lambda_o}\cos\theta_o\right) \qquad \text{for } Z = 0- \tag{19}$$

where equation (19) is the admittance looking into a short circuit from a transmission line having the characteristic admittance $\sqrt{\frac{\epsilon}{\mu}}/\cos\theta_o$ and propagation constant $2\pi\cos\theta_o/\lambda_o$.[7] The total impedance seen by the current sheet is

$$Z = \frac{1}{\left.\frac{H_x}{E_y}\right|_{0+} + \left.\frac{H_x}{E_y}\right|_{0-}} = \frac{\sqrt{\frac{\mu}{\epsilon}}\cos\theta_o}{1 - j\cot\left(\frac{2\pi d}{\lambda_o}\cos\theta_o\right)} . \tag{20}$$

Equation (20) is valid for scanning in the $\phi = 90°$ plane (E plane).

Note that in equation (20), the numerator is simply the ratio E_y/H_x of the excited plane wave. It can be shown that for a plane wave steered in the general direction θ_o, ϕ_o, the input impedance is

$$Z = \frac{\sqrt{\frac{\mu(\cos^2\theta_o + \sin^2\theta_o\cos^2\phi_o)}{\epsilon(\cos^2\theta_o + \sin^2\theta_o\sin^2\phi_o)}}}{1 - j\cot\left(\frac{2\pi d}{\lambda_o}\cos\theta_o\right)} . \tag{21}$$

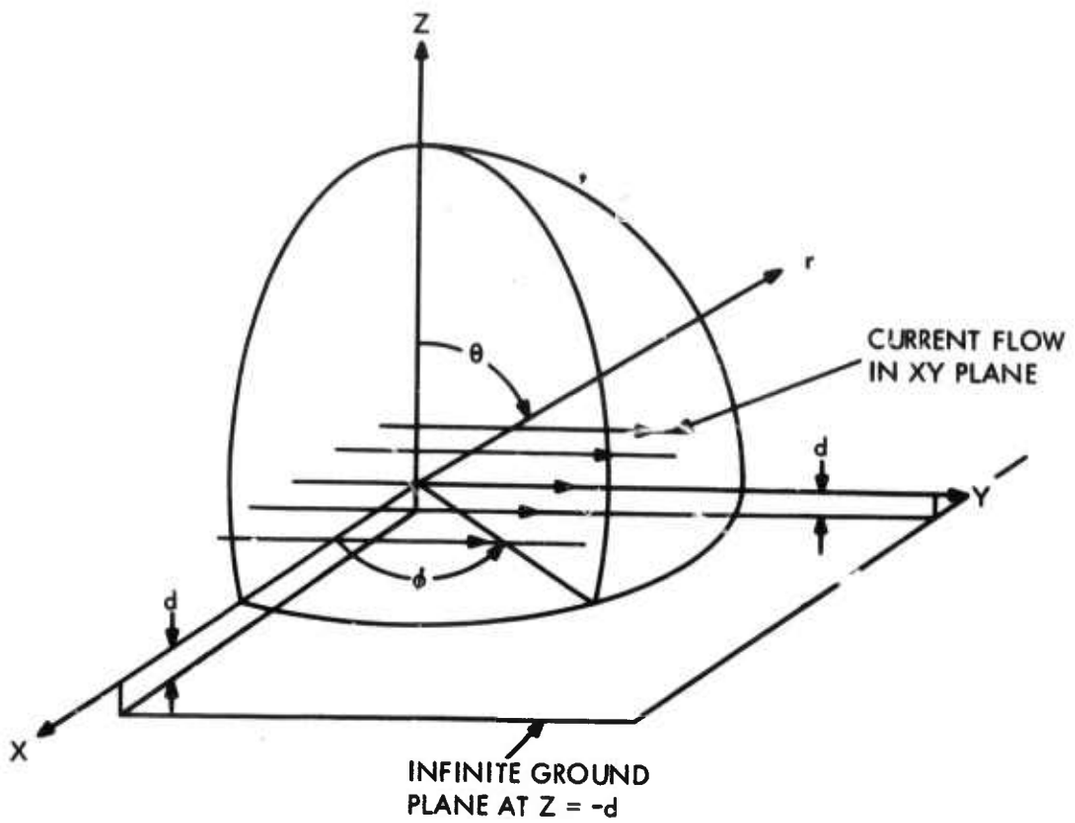

Figure B-13. Current Sheet Antenna

Letting $d = \lambda_o/4$ and plotting

$$Z_{\text{normalized}} = 1.3\sqrt{\frac{\epsilon}{\mu}}\, Z - j.75 \qquad (22)$$

the Smith Chart plots for E and H plane scan in Figure B-14 are obtained. The peculiar normalization of equation (22) was used to allow a direct comparison of Figure B-14 with Figures B-12 and B-5. Comparing these figures, it is seen that Figure B-12 is very similar to Figure B-14 and that the impedance plots of Figure B-12 are between the impedance plots of Figures B-5 and B-13 as expected.

Thus, the current sheet approach first suggested by Wheeler[8] for analysis of dipole arrays without a ground plane has been shown to be a useful approach for dipoles above a ground plane also. With this approach, the scan angle limits of a dipole element above a ground plane has been established.

References

1. Stark, L., "Radiation Impedance of a Dipole in an Infinite Array", Radio Science, Vol. 1, March 1966, pp. 361-367.

2. Allen, J. L.; et. al., "Phased Array Radar Studies", Lincoln Laboratory Technical Report #381, March 31, 1965.

3. Diamond, B. L., and Lewis, T. B., "Correlation of Experimental and Theoretical Active Impedance of a Dipole in an Array", IEEE Transactions on Antennas and Propagation, September 1965, pp. 806-807.

4. Sharp, E. D., "A Triangular Arrangement of Planar-Array Elements That Reduces the Number Needed", IRE Transactions on Antennas and Propagation, March 1961, pp. 126-129.

5. Baker, H. C., and LaGrone, A. H., "Digital Computation of the Mutual Impedance Between Thin Dipoles", IRE Transactions on Antennas and Propagation, March 1962, pp. 172-178.

6. Parad, L. I., and Kreutel, R. W., "Mutual Effects Between Circularly Polarized Elements", 12th Annual Symposium, USAF Antenna Research and Development Program, University of Illinois, October 1962.

7. Ramo, S., and Whinnery, J. R., "Fields and Waves in Modern Radio", John Wiley & Sons, Inc., New York, Second Edition 1953, pp. 296-298.

8. Wheeler, H. A., "Simple Relations Derived from a Phased-Array Antenna Made of a Infinite Current Sheet", IEEE Transactions on Antennas and Propagation, July 1965, pp. 506-514.

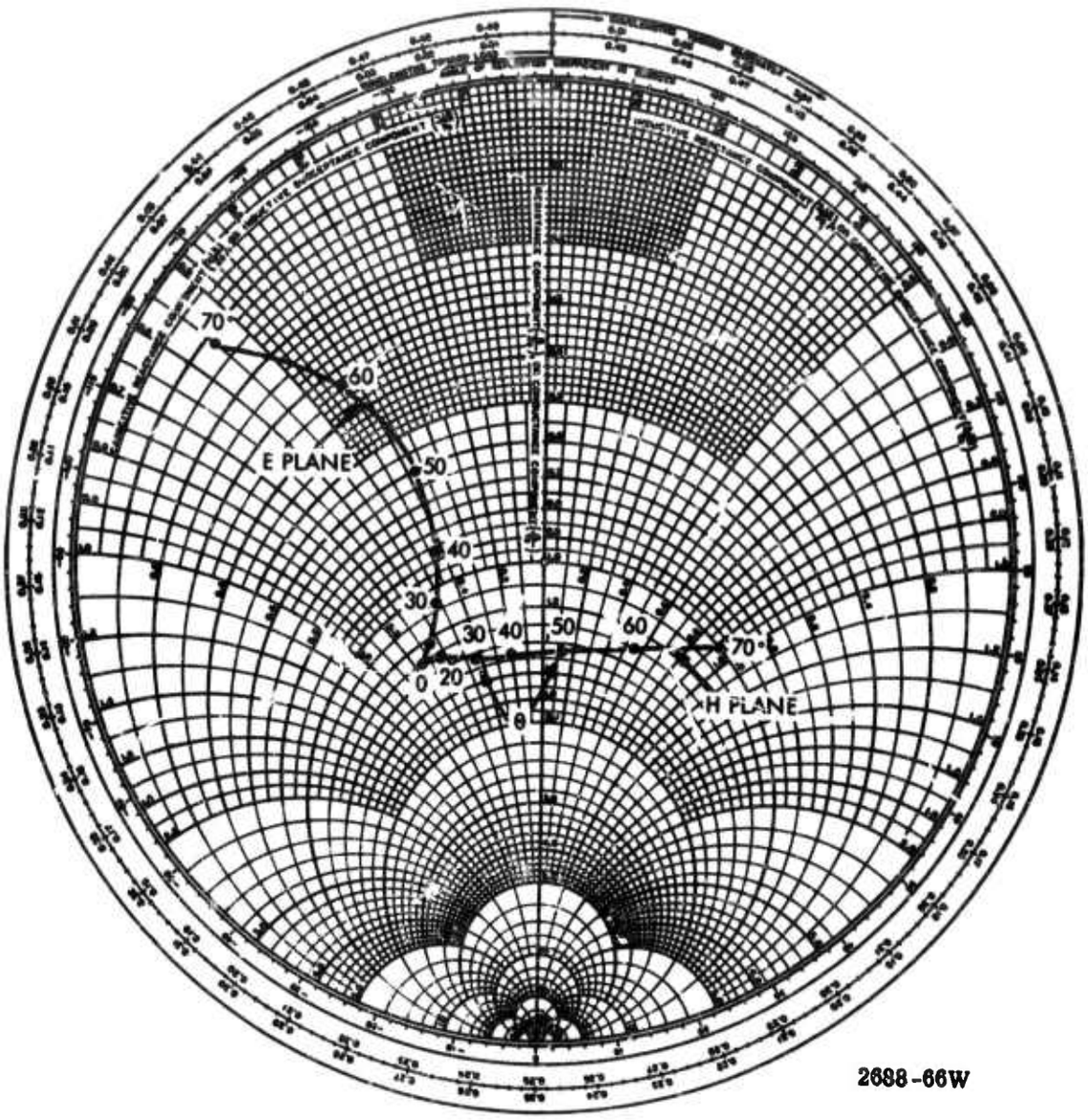

Figure B-14. Input Impedance of an Infinite Current Sheet $\lambda_0/4$ Above a Ground Plane

APPENDIX C

FLIGHT TEST PERFORMANCE DATA ON THE MAR RADAR SYSTEM

The MAR phased array radar system was developed by Sylvania under contract to Bell Telephone Laboratories (DA-30-069-ORD-1955). The radar uses circularly polarized coaxial horn antenna elements in a planar, hexagonal array similar to, but much larger than, the array used in this study. Extensive flight tests over the MAR radar confirm the surface wave analysis in this study.

A radar target was simulated by an airborne transmitter of known location, RF power, and polarization. The airborne transmitter (with controllable polarization) was tracked by the circularly polarized, phased array, radar receiver on the ground. The power output from the receiver sum channel was recorded as a function of array scan. The envelope of this sum beam maximum versus scan is the antenna element radiation pattern. Consequently we can compare this radar flight test data* with analytical and experimental element radiation characteristics obtained in this study contract.

When the MAR radar was scanned in the directions predicted in this study, radiation minima were observed. Received power dropped sharply by 3 db, and ellipticity exceeded 15 decibels. This occurred over a narrow angular band of the shape shown in Figure 5-5. These flight measurements showed that in the critical scan directions (near the edge of the radar design coverage) the radar array received only one linear polarization component and rejected the orthogonal component of the "radar echo". This could be explained by surface wave propagation across the array face in only the lowest T. M. mode. The measured holes in the coverage occurred at slightly larger scan angles (implying a slightly faster surface wave) than had been measured in the sample array under this study contract. This could be due to any of several small differences in the antenna elements or it could be a direct consequence of the different array sizes. (The MAR array was several times larger than the one used in this study.)

The radiation patterns of certain edge elements in the MAR receiver array were measured. These edge elements showed radiation nulls at the same scan angles as the nulls in the sum pattern of the full array. However, the edge elements radiated non-symmetrically; the deep null appeared only on that side away from the array center. This

*Courtesy of John Van Dolman, Bell Telephone Labs, White Sands, New Mexico

asymmetric performance of the edge element was predicted analytically. Mutual coupling and re-radiation are possible only from antenna elements on one side of an edge element. The phase delays through mutual coupling plus radiation retardation add in multiples of 2π for radiation or reception at the critical scan angle on the side of the array normal opposite the parasite. This accounts for the asymmetric radiation null.

The antenna element coupling coefficients in the MAR receiver array were also measured. The coupling data resembled Figures 4-2, 4-4, and 4-6 of this report except that

1) the coupling intensities in the MAR array were reported to be a few decibels weaker and,

2) the MAR coupling velocity was reported to be a few percent faster than found in our study.

Measurement of the MAR radar scan coverage, element radiation pattern, and mutual coupling coefficients confirm the findings in this study.

LIST OF SYMBOLS

$A_o, A_m, A_{m'}$	= column coupling amplitudes
c_o	= velocity of light in free space, 2.99790×10^8 m/s
d_x, d_y	= spacing between elements in X and Y directions
ϵ	= dielectric constant of medium
E	= total radiated field intensity (volts/meter)
$E_m(\theta, \phi)$	= electric field radiated by the m^{th} element per unit incident voltage
E_Σ	= radiated field intensity (volts/meter) from the whole array
h	= radome height above ground plane
K_o	= free space wave number
K_s	= wave number along array surface
m, n	= array indices locating the antenna element
N_o	= characteristic impedance of free space (377 ohms)
0, 0	= reference element indices
$P(\theta_s, \phi_s)$	= total power (watts) radiated by the array
R_v	= inverse square of the surface wave velocity
r, θ, ϕ	= spherical coordinates
S_{mn}	= mutual coupling coefficient between the central (0, 0) antenna and the (m, n) antenna
s	= subscript identifying the array steering commands
T	= radome thickness
TE_{10}	= transverse electric, wave mode in rectangular waveguide
TE_{11}	= transverse electric, wave mode in coaxial waveguide
TM_0	= transverse magnetic surface wave mode
u	= propagation constant normal to interface

LIST OF SYMBOLS (Continued)

V_d = volume of hemispheric radome dielectric

V_{mn} = drive applied to the (m, n) antenna, amplitude and phase

V_{oo} = drive applied to the reference element

v_s = phase velocity along array surface

V_m = incident voltage driving the m^{th} antenna element

x, y, z = cartesian coordinates

x = distance in the direction of surface wave propagation

z = distance normal to the surface

Z_o = characteristic impedance of the transmission lines

Z_s = tangential surface impedance

α = attenuation constant

γ = tangential propagation constant

$\Gamma_m(\theta_s\phi_s)$ = active reflection coefficient at the m^{th} element

$\eta_a(\theta_s\phi_s)$ = array efficiency = $\frac{\text{power radiated}}{\text{power consumed}}$

θ_{sc} = critical scan angles

θ_{sgL} = scan angle causing an end-fire grating lobe

$\theta_s\phi_s$ = array steering coordinates

λ_s = wavelength along array surface

Ψ_x, Ψ_y = phase increments between consecutive columns or rows

Ψ_m = phase of the mth column coupling coefficient

$\bar{\Psi}$ = mean coupling phase delay per column

$\bar{\Omega}_1$ = effective solid angle surrounding each major radiation lobe in real space

ω = angular frequency

PRESENTATIONS AND PUBLICATIONS

"Cumulative Coupling in Antenna Arrays" by L. W. Lechtreck, presented at the International Antenna & Propagation Symposium on August 31, 1965. Program & Digest, pp. 144-9.

VISITS & VISITORS

July 13, 1965 at Sylvania
Sylvania Participants: K. Rau, L. Lechtreck, L. Parad
Bell Telephone Participants: R. Pecina, R. Lowell, R. Rice, R. Heidt, P. Butzine
Subject: Phased Arrary Tests

October 21, 1965 at Sylvania
Sylvania Participants: L. Lechtreck, L. Parad
R.A.D.C. Participant: C. Pankiewicz
Lincoln Lab. Participant: D. Bernella
Subject: Progress Review

January 17, 1966 at White Sands, New Mexico
Sylvania Participant: L. Lechtreck
Bell Telephone Labs Participant: John Van Dolman
Subject: MAR Radar Performance

January 18, 1966 at Hughes Aircraft (Fullerton, California)
Sylvania Participant: L. Lechtreck
Hughes Participants: R. Tang, L. Stark, E. Dufort, DuHamel
Subject: Array Technical Studies under AF19-628-4984 and AF30 (602)-3886.

April 19, 1966 at Sylvania
Sylvania Participants: L. Lechtreck, L. Parad
Customer Representatives: Lt. Col. John Toomay, C. Pankiewicz, Dr. R. Mack
Subject: Contract Review

July 14, 1966 at Sylvania
Sylvania Participants: L. Lechtreck, L. Parad
R.A.D.C. Participant: C. Pankiewicz
Subject: Progress Report

July 18, 1966 at Lincoln Labs.
Sylvania Participants: L. Lechtreck, L. Parad
Lincoln Lab. Participants: B. Diamond, D. Bernella
Subject: Dipole Array Theory and Tests.

CONCLUSIONS

Analysis and experimental evidence show that array performance can vary greatly with scan angle. In-phase coupling accumulation can cause deep holes in the scan coverage of a phased array. Coupling accumulation seems to be largest (deepest radiation nulls) in those antenna arrays which provide a mechanism for launching and propagating an electromagnetic wave along the array face. In some arrays, this coupling wave travels at a velocity substantially less than the velocity of light in free space. Slow wave coupling accumulation leads to radiation minima at scan angles less than those for which a grating lobe peak enters real space. In this case, scan performance is limited, not by the classical grating lobe considerations, but rather by cumulative coupling. Radiation nulls can occur within the design coverage if the array spacing is chosen to merely keep the grating lobe maxima outside real space for all required array scan directions.

In a phased array, mutual coupling between any pair of antenna elements is usually quite small. Their individual effect on array performance is usually negligible. Large degradations of array performance occur when many coupling contributions add in-phase in the critical scan regions. For this reason, cumulative coupling minima may not be recognizable in the analysis or test of small array samples frequently used in the development and test of antenna elements for use in large phased arrays.

Multifunction radars frequently use phased arrays to form and steer high resolution radar beams. The effectiveness of such an antenna array is measured in terms of its angular radiation coverage, polarization ratio, active impedance, and efficiency. All these aspects of the antenna array are related so that serious degradation in one aspect is usually reflected in the others.

Consequences to system performance at the critical scan angles depend upon the array design. Measurements here suggest that one linear polarization (electric field in the plane of scan) could be almost totally reflected at the array face with virtually no radiation of this polarization at these scan angles. A linearly polarized array would be blind in these directions; a circularly polarized array could radiate only one linearly polarized component; a two port polarization diversity receiver would accept the same linear polarization ($\vec{E}$ perpendicular to the plane of scan) at both antenna terminals, thus losing polarization discrimination capability. In three-dimensional space, the critical scan regions are bounded by corrugated cones, parallel to, and inside, the scan surface defined by the emergence of a grating lobe maximum into real space.

The existence of deep radiation holes and related deterioration in array performance are not inherently bad, provided these degradations are kept outside the scan coverage required of the phased array. Array performance which deteriorates abruptly outside the required coverage region may be preferable to lesser degradations spread across all scan space including the scan area for which strong array coverage is desired.

RECOMMENDATIONS FOR FUTHER STUDY

Effective use of phased arrays requires an accurate knowledge of the potentialities and limitations of this type of radiating system. Phased array understanding remains incomplete in certain important engineering areas. We will try to identify those critical areas closely related to this study.

This study has shown the relation between the angular position of radiation minima and array coupling velocity. Null depths in measured element radiation patterns were found to vary greatly with the microwave frequency and array polarization. Sometimes a secondary minimum was observed at a wider scan angle than the first minimum. Array coverage is limited by the first minimum; its angular location has been explained. The depth of the first minimum and the occasional observance of a second minimum have not been fully explained.

Antenna elements for large arrays are usually developed and tested in small array samples. Antenna element performance is known to change significantly in passing from a small to a large array. A general theory (or new test procedure) is urgently needed to extrapolate element performance measured in a small array to performance of that same element in a large array.

An array of flush coaxial horns has been tested and reported to have no radiation nulls in the forward hemisphere of the array ($|\theta_s| < 90°$), even under conditions where a grating lobe approaches and enters real space. A more critical examination of this high potential array element is needed.

Finally, a variety of classical slow wave structures have been analyzed by others. Some of these physical shapes resemble phased arrays. Application of these classical solutions to phased array problems could lead to techniques for estimating coupling velocity and assuring that future array designs have cumulative coupling nulls outside their required scan coverage.

ACKNOWLEDGMENTS

This work was supported by Rome Air Development Center under Contract AF 30 (602) 3886 and order No. 723 from the Advanced Research Projects Agency. Encouragement from the contract monitors C. Pankiewicz and Lt. Col. John Toomay is appreciated. Appendices A and B were written by L. Parad, and numerous helpful criticisms were made by Dr. B. Nelson (both of Sylvania Electronic Systems).

BLANK PAGE

Unclassified
Security Classification

DOCUMENT CONTROL DATA - R&D

(Security classification of title, body of abstract and indexing annotation must be entered when the overall report is classified)

1. ORIGINATING ACTIVITY (Corporate author)

Sylvania Electronic Systems
Waltham, Mass. 02154

2a. REPORT SECURITY CLASSIFICATION

Unclassified

2b. GROUP

3. REPORT TITLE

SURFACE WAVE BEHAVIOR IN PHASED ARRAYS

4. DESCRIPTIVE NOTES (Type of report and inclusive dates)

Final Technical Report

5. AUTHOR(S) (Last name, first name, initial)

Lechtreck, Dr. Lawrence W.

6. REPORT DATE	7a. TOTAL NO. OF PAGES	7b. NO. OF REFS
October 21, 1966	118	37

8a. CONTRACT OR GRANT NO.

AF30(602)3886

b. PROJECT NO.

4506

c. Task No. 450604

d. ARPA Order No. 7_

9a. ORIGINATOR'S REPORT NUMBER(S)

S66-12

9b. OTHER REPORT NO(S) (Any other numbers that may be assigned this report)

RADC-TR-66-663

10. AVAILABILITY/LIMITATION NOTICES

This document is subject to special export controls and each transmittal to foreign governments or foreign nationals may be made only with prior approval of RADC (EMLI), GAFB, NY, 13440.

11. SUPPLEMENTARY NOTES

RADC Project Engineer:
Charles L. Pankiewicz/EMATA/330-2443
ARPA Project Engineer: Lt. Col. John Toomay

12. SPONSORING MILITARY ACTIVITY

Rome Air Development Center
Techniques Branch (EMAT)
Griffiss AFB, NY, 13440

13. ABSTRACT

Mutual coupling in a phased array can cause its radiation performance to vary with electrical phasing used to steer the array. Large performance degradations can accrue when many coupling contributions add in-phase. This happens when the steering phase advance equals the mutual coupling phase delay between consecutive elements. For these critical scan directions reflections can be very large, and the antenna array will transmit or receive very little power, as evidenced by deep holes in the element radiation pattern.

A large, flat, uniformly spaced array of identical antenna elements is analyzed. A relationship is found between critical scan angle and mutual coupling coefficients. Element radiation pattern, active array mismatch, and radiation efficiency are shown to be equivalent representations of phased array scan performance.

Extensive radiation pattern and mutual coupling measurements were made in a planar, equiangular array of coaxial horn antennas. These measured mutual coupling coefficients were summed over columns of the test array. The phases of these column sums were found to vary linearly with distance. At the critical scan angle, all columns on one side of the array couple in-phase and re-radiate destructively, causing deep holes in array coverage and in element radiation pattern. Empirical coupling velocities were less than the free space velocity of light. Radiation holes appeared at scan angles which were smaller than those for which the grating lobe maximum enters real space.

Many physical perturbations of the array geometry were investigated experimentally to determine their influence on array scan performance. Several diverse array types are reported to have radiation minima attributable to in-phase coupling accumulation.

DD FORM 1 JAN 64 1473

Unclassified
Security Classification

14 KEY WORDS	LINK A		LINK B		LINK C	
	ROLE	WT	ROLE	WT	ROLE	WT
Radar Antennas Coupled Antennas Antenna Radiation Patterns Phased Arrays Radar Scanning						

INSTRUCTIONS

1. ORIGINATING ACTIVITY: Enter the name and address of the contractor, subcontractor, grantee, Department of Defense activity or other organization *(corporate author)* issuing the report.

2a. REPORT SECURITY CLASSIFICATION: Enter the overall security classification of the report. Indicate whether "Restricted Data" is included. Marking is to be in accordance with appropriate security regulations.

2b. GROUP: Automatic downgrading is specified in DoD Directive 5200.10 and Armed Forces Industrial Manual. Enter the group number. Also, when applicable, show that optional markings have been used for Group 3 and Group 4 as authorized.

3. REPORT TITLE: Enter the complete report title in all capital letters. Titles in all cases should be unclassified. If a meaningful title cannot be selected without classification, show title classification in all capitals in parenthesis immediately following the title.

4. DESCRIPTIVE NOTES: If appropriate, enter the type of report, e.g., interim, progress, summary, annual, or final. Give the inclusive dates when a specific reporting period is covered.

5. AUTHOR(S): Enter the name(s) of author(s) as shown on or in the report. Enter last name, first name, middle initial. If military, show rank and branch of service. The name of the principal author is an absolute minimum requirement.

6. REPORT DATE: Enter the date of the report as day, month, year; or month, year. If more than one date appears on the report, use date of publication.

7a. TOTAL NUMBER OF PAGES: The total page count should follow normal pagination procedures, i.e., enter the number of pages containing information.

7b. NUMBER OF REFERENCES: Enter the total number of references cited in the report.

8a. CONTRACT OR GRANT NUMBER: If appropriate, enter the applicable number of the contract or grant under which the report was written.

8b, 8c, & 8d. PROJECT NUMBER: Enter the appropriate military department identification, such as project number, subproject number, system numbers, task number, etc.

9a. ORIGINATOR'S REPORT NUMBER(S): Enter the official report number by which the document will be identified and controlled by the originating activity. This number must be unique to this report.

9b. OTHER REPORT NUMBER(S): If the report has been assigned any other report numbers *(either by the originator or by the sponsor)*, also enter this number(s).

10. AVAILABILITY/LIMITATION NOTICES: Enter any limitations on further dissemination of the report, other than those imposed by security classification, using standard statements such as:

(1) "Qualified requesters may obtain copies of this report from DDC."

(2) "Foreign announcement and dissemination of this report by DDC is not authorized."

(3) "U. S. Government agencies may obtain copies of this report directly from DDC. Other qualified DDC users shall request through _____."

(4) "U. S. military agencies may obtain copies of this report directly from DDC. Other qualified users shall request through _____."

(5) "All distribution of this report is controlled. Qualified DDC users shall request through _____."

If the report has been furnished to the Office of Technical Services, Department of Commerce, for sale to the public, indicate this fact and enter the price, if known.

11. SUPPLEMENTARY NOTES: Use for additional explanatory notes.

12. SPONSORING MILITARY ACTIVITY: Enter the name of the departmental project office or laboratory sponsoring *(paying for)* the research and development. Include address.

13. ABSTRACT: Enter an abstract giving a brief and factual summary of the document indicative of the report, even though it may also appear elsewhere in the body of the technical report. If additional space is required, a continuation sheet shall be attached.

It is highly desirable that the abstract of classified reports be unclassified. Each paragraph of the abstract shall end with an indication of the military security classification of the information in the paragraph, represented as *(TS), (S), (C), or (U)*.

There is no limitation on the length of the abstract. However, the suggested length is from 150 to 225 words.

14. KEY WORDS: Key words are technically meaningful terms or short phrases that characterize a report and may be used as index entries for cataloging the report. Key words must be selected so that no security classification is required. Identifiers, such as equipment model designation, trade name, military project code name, geographic location, may be used as key words but will be followed by an indication of technical context. The assignment of links, roles, and weights is optional.